



**HAL**  
open science

# Physical nanoscale analysis of heat transfer in defective nanowires

Shiyun Xiong

► **To cite this version:**

Shiyun Xiong. Physical nanoscale analysis of heat transfer in defective nanowires. Engineering Sciences [physics]. Ecole Centrale Paris, 2014. English. NNT : 2014ECAP0054 . tel-01127355

**HAL Id: tel-01127355**

**<https://theses.hal.science/tel-01127355>**

Submitted on 7 Mar 2015

**HAL** is a multi-disciplinary open access archive for the deposit and dissemination of scientific research documents, whether they are published or not. The documents may come from teaching and research institutions in France or abroad, or from public or private research centers.

L'archive ouverte pluridisciplinaire **HAL**, est destinée au dépôt et à la diffusion de documents scientifiques de niveau recherche, publiés ou non, émanant des établissements d'enseignement et de recherche français ou étrangers, des laboratoires publics ou privés.

## THÈSE

présentée par

**Shiyun Xiong**

pour l'obtention du

GRADE de DOCTEUR

Formation doctorale : Physique et Sciences pour l'Ingénieur

Laboratoire d'accueil : Laboratoire d'Énergétique Moléculaire  
et Macroscopique, Combustion (EM2C)  
du CNRS et de l'École Centrale Paris

### Physical Nanoscale Analysis of Heat Transfer in Defective Nanowires

Soutenue le 07 Novembre 2014

<b>Jury :</b>	MM	KOSEVICH	Yuriy	Rapporteur
		DONADIO	Davide	Rapporteur
		PERRIN	Bernard	
		JOULAIN	Karl	
		CORTONA	Pietro	
		CHALOPIN	Yann	
		VOLZ	Sebastian	Directeur de thèse



# Acknowledgement

First and foremost, I am deeply grateful to my supervisor Prof. Sebastian Volz for his professional tutoring, fruitful discussions and continuous encouragement during the past three years. I appreciate a lot the weekly one-to-one discussions, through which I can always get new ideas and also get more closed to the spirit of nano-scale heat transfer. I am full of gratitude to Sebastian Volz for sending me to numerous conferences during my Ph.D, from which I learnt a lot.

Millions of thanks should be sent to Prof. Pietro Cortona and Prof. Yurii Chumakov for teaching me the density functional theory. They are always very patient to answer my questions. Great thanks also go to Kaike Yang and Prof. Roberto D'Agosta at Universidad del País Vasco (UPV), from whom I acquired the Green's function techniques. Prof. Yuriy Kosevich at Russian academy of sciences, Prof. Traian Dumitrică at the university of Minnesota and Dr. Yuxiang Ni are greatly acknowledged for the collaborations and their useful discussions, suggestions and contributions to the thesis.

I am greatly indebted to all my thesis committee members: Yuriy Kosevich, Davide Donadio, Bernard Perrin, Karl Joulain, Pietro Cotona, Yann Chalopin, for their useful comments and suggestions on the thesis. Many thanks for the help from my friends and colleagues: Yuxiang Ni, Kimmo Sääskilahti, Wassim Kassem, Haoxue Han, Benoit Latour, Jose-Ediberto Ordonez Miranda, Laurent Tranchant, Jordane Soussi, Yann Chalopin, Thomas Antoni, Konstantinos Termentzidis and Alexis Pokropivny ... There are lots of happy memories with you and I will always treasure our friendship.

The China Scholarship Council (CSC) is acknowledged for the financial support.

Last but not least, I would like to express my deep thanks to my wife, Yajuan Cheng, for her selfless and endless supporting and help. She is always with me whenever I have difficulties. This thesis would not come to be possible without her love and encouragement. I also acknowledge the continuous support from my parents and brother. Their love and encouragement make me progress continuously.



# Abstract

This thesis is focused on the investigation of the impact of various lattice defects, i.e., screw dislocations, anti-phase boundaries, twinning boundaries, and vacuum gaps, on the thermal conductivity of nanowires by molecular dynamic simulations and Green's function calculations.

We firstly calculated the thermal conductivity of  $\langle 110 \rangle$  Si nanowires with a screw dislocation in the center through non-equilibrium molecular dynamics. We find that with the inclusion of a dislocation, the phonon-phonon scattering rate is enhanced dramatically due to the dislocation-induced strain field. This anharmonic scattering process increases with the Burger's vector. As a result, the thermal conductivity of dislocated nanowires is largely reduced and the reduction percentage is proportional to the magnitude of Burger's vector.

Secondly, the concept of anti-phase superlattice nanowire is proposed and its thermal conductivity is investigated with equilibrium molecular dynamics. It is found that the anti-phase boundary can strongly scatter phonons and reduce the phonon group velocity. The interplay between phonon coherent transport and boundary scattering results in a minimum thermal conductivity at a specific period length. The combination of anti-phase boundary scattering and nanowire surface scattering reduces the thermal conductivity of SiC by two orders of magnitude, which is of great interest for potential thermoelectric applications.

Thirdly, we demonstrate that phonon transport can be hindered to a large extent in a Si nanowire with periodically distributed twinning boundaries. A minimum thermal conductivity is observed due to a pure geometrical effect, which produces a thorough disappearance of favored phonon polarization directions at a specific period length. The minimum thermal conductivity and the corresponding period length are diameter dependent. The advantage of this structure is that it largely suppresses the thermal transport without deteriorating the electron transport.

Finally, the transition from heat conduction to near field radiation in a SiO<sub>2</sub> cluster chain system is investigated with the phonon Green's function. Three

conductance variation regions within the studied distances are identified, more specifically, the heat conduction region with shared electrons in the middle of a gap, the near field region predominated by surface charge interactions, and the near field region predominated by volume dipole-dipole interactions. This study finally provides a description of the transition between radiation and heat conduction in gaps smaller than a few nanometers.

# Résumé

Cette thèse se concentre sur l'étude de l'impact de divers défauts de réseau, c'est-à-dire de dislocations, de parois entre phases inversées, de décalages de mailles et de gaps, sur la conductivité thermique de nano-fils par simulation de dynamique moléculaire et les calculs de fonctions de Green atomiques.

Tout d'abord, nous calculons la conductivité thermique de nanofils de silicium orientés  $\langle 110 \rangle$  incluant une dislocation spirale par la dynamique moléculaire de non-équilibre. Nous constatons qu'avec l'inclusion d'une dislocation, le taux de diffusion phonon-phonon est amélioré de façon significative en raison de l'existence du champ de déformation induit. Ce processus de diffusion anharmonique augmente avec le vecteur de Burger. Par conséquent, la conductivité thermique de nano-fils disloqués est largement réduite et le pourcentage de réduction est proportionnel à la grandeur du vecteur de Burger.

Deuxièmement, le concept de nano-fils de super-réseau anti-phase est proposé et leur conductivité thermique est étudiée avec la dynamique moléculaire d'équilibre. On constate que la frontière anti-phase peut diffuser fortement les phonons et réduire la vitesse de groupe des phonons. Le jeu entre le transport cohérent de phonons et la diffusion de surface conduit à une conductivité thermique minimale à une période de longueur spécifique. La combinaison de la diffusion des phonons à l'interface et la diffusion de surface des nanofils réduit la conductivité thermique de SiC de deux ordres de grandeur, ce qui est d'un grand intérêt pour les applications en thermoélectricité.

Troisièmement, nous démontrons que le transport des phonons peut être entravé en grande partie dans un nano-fil de Si avec une structure en zig-zag périodique. Une conductivité thermique plus faible est observée du fait d'un pur effet géométrique, qui produit une disparition complète des directions principales de polarisation de phonon à une période de longueur spécifique. La conductivité thermique minimale et la longueur de période correspondante sont dépendantes du diamètre. L'avantage de cette structure est qu'elle supprime en grande partie le transport thermique sans détériorer le transport d'électrons.

Enfin, la transition entre la conduction de la chaleur et le rayonnement de

champ proche dans un système de chaîne de clusters de  $\text{SiO}_2$  est étudiée avec la méthode des fonctions de Green. Trois régions de variation de la conductance dans ce domaine de largeur de gap sont identifiés, plus particulièrement, la région liée à la conduction où les électrons des deux corps sont mis en commun au milieu du gap, la région de champ proche prédominée par des interactions de charges de surface, et la région de champ proche prédominée par des interactions dipôle-dipôle de volume. Cette étude fournit finalement une description de la transition entre le rayonnement et la conduction de la chaleur dans les gaps de dimensions inférieures à quelques nanomètres.

# Contents

<b>Abstract</b>	<b>v</b>
<b>Résumé</b>	<b>vii</b>
<b>1 Introduction</b>	<b>1</b>
1.1 Energy Challenges . . . . .	1
1.1.1 Thermoelectric Materials . . . . .	2
1.1.2 Thermal Interface Materials . . . . .	5
1.1.3 Thermal Diode Materials . . . . .	7
1.1.4 Thermal Cloak Materials . . . . .	9
1.2 Scientific Background . . . . .	11
1.2.1 Lattice Vibrations and Phonons . . . . .	11
1.2.2 Phonon Transport in Nanoscale . . . . .	16
1.2.3 Phonon Engineering with Defects . . . . .	18
1.3 Organization of the Thesis . . . . .	21
<b>2 Methods</b>	<b>23</b>
2.1 Molecular Dynamics . . . . .	23
2.1.1 Background . . . . .	23
2.1.2 Thermal Conductivity from Equilibrium Molecular Dynamics Simulation . . . . .	26
2.1.3 Thermal Conductivity from Non-equilibrium Molecular Dynamics Simulation . . . . .	28
2.1.4 Challenges of Molecular Dynamic Simulations . . . . .	29
2.2 Phonon Green's Function . . . . .	30
2.2.1 General Formulation . . . . .	30
2.2.2 Recursive method for surface Green's function calculation . . . . .	33
2.3 Lattice Dynamics . . . . .	36
2.3.1 Phonon Dispersion Relation . . . . .	36
2.3.2 Phonon Group Velocity . . . . .	38
2.3.3 Vibrational Mode Analysis . . . . .	39
2.4 Conclusions . . . . .	41
<b>3 Strain Defects in Nanowires: Thermally-Active Screw Disloca-</b>	

<b>tions in Si Nanowires and Nanotubes</b>	<b>43</b>
3.1 Introduction . . . . .	43
3.2 Impact of Dislocation on Thermal Conductivity: The Classical Theory . . . . .	46
3.3 Simulation Details . . . . .	47
3.4 Physical Analysis of SD NWs and NTs Thermal Conductivity . . . . .	49
3.4.1 Structure Optimisation and Eshelby Twist Angle . . . . .	49
3.4.2 Thermal Conductivity . . . . .	51
3.4.3 Eigen-mode Analysis . . . . .	55
3.4.4 Green's Function Analysis . . . . .	56
3.5 Conclusions . . . . .	58
<b>4 Structural Defects in Nanowires: Efficiently Phonon Blocking in SiC with Antiphase Superlattice Nanowires</b>	<b>61</b>
4.1 Introduction . . . . .	61
4.2 Structure and Simulations . . . . .	64
4.3 Physical Analysis of SiC AP SLNW Thermal Conductivity . . . . .	66
4.3.1 Thermal Conductivity . . . . .	66
4.3.2 Coherent and Incoherent Phonon Transport . . . . .	68
4.3.3 Phonon Density of States Analysis . . . . .	70
4.3.4 Phonon Group Velocity Analysis . . . . .	73
4.4 Conclusions . . . . .	75
<b>5 Geometrical Defects in Nanowires: Minimum Thermal Conductivity in Si Twinning Superlattice Nanowire Based Phononic Metamaterial</b>	<b>77</b>
5.1 Introduction . . . . .	78
5.2 Structure and Simulation details . . . . .	80
5.3 Thermal Conductivity Analysis of Twinning SL NWs . . . . .	82
5.3.1 Thermal Conductivity . . . . .	82
5.3.2 Phonon Polarization Analysis . . . . .	85
5.3.3 Phonon Dispersion and Transmission . . . . .	87
5.3.4 Temperature Dependent Thermal Conductivity . . . . .	89
5.3.5 Coating Effects on Thermal Conductivity . . . . .	91
5.4 Conclusions . . . . .	93
<b>6 Void Defects in Nanowires: Transition from Heat Conduction to Radiation in Nanoscale Gaps</b>	<b>95</b>
6.1 Introduction . . . . .	95
6.2 Structure and Simulation methods . . . . .	99
6.3 Physical Analysis of the Thermal Conductance between Two Clusters . . . . .	100
6.3.1 Thermal Conductance . . . . .	100
6.3.2 Electron Density Analysis . . . . .	103

CONTENTS

xi

6.3.3 Phonon Transmission Spectra . . . . .	104
6.4 Conclusions . . . . .	106
<b>7 Conclusions and Future works</b>	<b>109</b>
7.1 Conclusions . . . . .	109
7.2 Future Works . . . . .	111
<b>References</b>	<b>123</b>



# List of Tables

3.1	Number of Si atoms in the objective cell, twist, energetics, and thermal conductivity of (12,0) NWs and (12,4) NTs. The magnitude of the Burgers vector ( $1b$ , $2b$ , and $3b$ , where $b = 3.8 \text{ \AA}$ ) is indicated in the subscript notation. . . . .	52
4.1	List of the Tersoff two body potential parameters used in Eq. 4.3 and 4.4. . . . .	72
5.1	Thermal conductivities of pristine NWs and twinning SL phononic metamaterial NWs with different diameters at 300 K. The resulting reductions in percentage are reported in the last line. . . . .	82
5.2	Summarize of the fitting parameters of $a$ and $b$ used in Eq. 5.5. . . . .	91



# List of Figures

1.1	World energy demand in the past and future 30 years (Source: EIA, World Energy Outlook 2008). . . . .	2
1.2	Schematic of the thermoelectric module for both cooling and power generation. The arrows indicate the direction of charge flow. Figure from G. Jeffrey and Eric S. Toberer, Nat. Mater., 2008, 7: 105 . . . . .	3
1.3	A summarize of the figure of merit of state-of-the-art for (a) n-type and (b) p-type commercial thermoelectric materials. Figure from G. Jeffrey and Eric S. Toberer, Nat. Mater., 2008, 7: 105 . . . . .	4
1.4	Schematic of a rough interface with (right) and without (left) thermal interface material filling. Heat can only propagate through sparse spots when no thermal interface material is used while heat can dissipate through the entire interface when a thermal interface material is filled. Figure from internet ( <a href="http://www.bit-tech.net/hardware/2009/02/16/all-about-tim/">http://www.bit-tech.net/hardware/2009/02/16/all-about-tim/</a> ) . . . . .	6
1.5	Sketch of the thermal diode module (up) and the heat current vs the relative temperature bias behavior of a thermal diode (down). Figure from Li, Lan and Wang, 2005, Phys. Rev. Lett. 95: 104302 . . . . .	7
1.6	Experimental realization of thermal rectification with mass-loading nanotubes. (a) Scanning electron microscope images of BNNTs after deposition of C <sub>9</sub> H <sub>16</sub> Pt. (b) Sensor temperature ( $\Delta T_s$ ) vs heater temperature ( $\Delta T_h$ ) for the NTs before and after deposition of C <sub>9</sub> H <sub>16</sub> Pt. Figure from Chang, Majumdar, and Zettl, 2006 Science, 314: 1121 . . . . .	9
1.7	Thermal invisibility cloak: Heat is passed around the central area from the left to the right. Temperature characteristics (white lines) remain parallel. Figure from internet: <a href="http://www.sciencedaily.com/releases/2013/05/">http://www.sciencedaily.com/releases/2013/05/</a>	
1.8	An one-atomic chain with the lattice constant $a$ and mass $M$ at the equilibrium position (up) and with a displacement for each atom (down) . . . . .	11
1.9	(a) Phonon dispersion curve and (b) phonon group velocity of the diatomic chain . . . . .	15

1.10	Experimentally measured normalized thermal conductance with the change of temperature. When the temperature is below 0.8 K, a saturation in conductance at a value near the expected quantum of thermal conductance. Figure from K. Schwab et al. Nature (2000) 404: 974. . . . .	19
1.11	Calculated thermal conductivity for defected bulk $\text{Bi}_2\text{Te}_3$ as a function of the vacancy concentration. Left side of the figure corresponds to $\text{Bi}_{40-x}\text{Te}_{60}$ and right side to $\text{Bi}_{40}\text{Te}_{60-y}$ . Figure from Konstatinos et al. J. App. Phys. (2013) 113: 013506 . . .	20
2.1	An example of heat flux autocorrelation function with the fitting of different methods. The insert represents the integral of the thermal conductivities over time. Figure from McGaughey, A. and M. Kaviany (2004), International Journal of Heat and Mass Transfer 47: 1783 . . . . .	27
2.2	The inverse of the thermal conductivities measured with NEMD simulations for Si and diamond at specified temperatures versus $1/L$ and the corresponding fitting with Eq. 2.16. $\kappa_\infty$ is get at $1/L = 0$ . Figure from Schelling et al (2002), Phys. Rev. B 65: 144306 . . . . .	28
2.3	Schematic for the Green's function calculation with the left and right leads and the central scattering region. The force constant matrices for the three regions are denoted as $K^L$ , $K^R$ and $K^C$ , respectively. The coupling matrices between the left lead and the central region, the right lead and the central region are denoted as $V^{LC}$ and $V^{RC}$ , respectively . . . . .	32
2.4	Schematics for the surface Green's function calculation by gluing each sections together. All the blocks are firstly isolated (top). After the second block is glued on the first block (middle) and the Green's function of each section can be calculated. By repeating the process, the $N^{\text{th}}$ section can be attached on the $n^{\text{th}}$ section and forming a chain with $N$ blocks (bottom). The Green's functions of each blocks can be evaluated consequently.	34
2.5	An example of the dynamic force constant summation (Eq. 2.39) in a two dimensional lattice. Due to the cut off of potential energy, only the near neighbour cells have non-zero elements in the real space force constant matrices. As a result, the summation is restricted to the near interact neighbour cells. . . . .	37
3.1	Schematic of the formation of an edge and a screw dislocation from a perfect lattice (left). . . . .	44

3.2	(a) SEM microscopy of screw dislocations in a PbS nanowire; (b) schematic representation of screw-dislocation-driven trunk growth combined with slower epitaxial vapor-liquid-solid-driven branch growth; (c) a simplified scheme illustrating that the self-perpetuating steps of a screw dislocation spiral at the tip of a trunk can enable 1D crystal growth of nanowires. Figure from M. J. Bierman et al, Science, 2008, 320: 1060. . . . .	45
3.3	Schematic presentation of a simulated pristine Si nanowire (left) and a dislocated Si nanowire with Eshelby twist (right). . . . .	47
3.4	Optimal configuration (left) and total energy vs. twist angle (right) for (a) (12,0) NW and (b) (12,4) <sub>b</sub> NT. The dashed line indicates the cut made to create the dislocation. . . . .	49
3.5	Eshelby twist angles as a function of the Burger's vector magnitude for SD NWs with specific diameters. . . . .	50
3.6	Formation energies as a function of the ratio $h/L$ with $L = 12$ . (a) formation energies compared to bulk state ( $E_f$ ); (b) formation energies compared to the corresponding pristine structures ( $E_{fd}$ ). . . . .	51
3.7	Example of thermal conductivity measuring set up with NEMD method for a SD NW with 2b Burger's vector (top). The atoms at the two ends are fixed and next to the fixed layers, a couple of atom layers are coupled to the Nosé-Hoover thermal bath with the temperature $T_0 + \Delta/2$ and $T_0 - \Delta/2$ , respectively. (a) Raw data of the averaged temperature profile (solid line) and the linear fit (dashed line) for the intermediate region; (b) Energy $E$ injected into and subtracted from the hot and cold thermal baths, respectively. . . . .	53
3.8	Dependence of $1/\kappa$ on $1/L_z$ for pristine and SD (a) (12,0) NWs and (b) (12,4) NTs. The intercept of the linear fit with the vertical axis gives for infinitely-long structures. Relative comparison of for (c) NWs and (d) NTs with $L_z = 20$ nm. The filled (open) symbols correspond to untwisted (twisted) structures. Here $b = 3.8 \text{ \AA}$ . . . . .	54
3.9	Phonon polarization distributions of a longitudinal acoustic mode for (a) (12,0) and (b) (12,0) <sub>3b</sub> NWs at the frequency 2 THz. . . . .	56
3.10	(a) Phonon transmission function and (b) thermal conductance under harmonic approximation for (12,0) pristine and SD NWs; (c) modified phonon transmission function and (d) thermal conductance with manually introduction of anharmonicity. . . . .	57
4.1	(a) The observation of a local anti-phase domain in GeTe nanowire from a TEM image. (b) electron diffraction image shows spot splitting (circled in white) along the nanowire growth direction. Figure from Pavan Nukala et al, Nano Lett. 14: 2201 (2014) . . . . .	63

4.2	Stacking sequence of double layers of the four most common SiC polytypes. Figure from <a href="http://staff.csc.fi/~raback/sic/thesis/node6.html">http://staff.csc.fi/~raback/sic/thesis/node6.html</a> . . . . .	65
4.3	Schematics of the SiC APSLs; (a) A SL with two periods along the $z$ direction showing the stacking sequence of Si and C atoms and the Si-Si and C-C interfaces; (b) An example of hexagonal cross-section of APSL nanowires. . . . .	65
4.4	Example of a heat flux autocorrelation function (a) and its integral (b) vary with the correlation time for the antiphase nanowire with period of 9.06 nm. The black and blue curves are the ACF and ACF integral of each simulation (in total 24). The red curve in (a) and pink curve in (b) are the average of ACF and integral of ACF, respectively. . . . .	66
4.5	Thermal conductivity of APSL NWs with diameter of 3 nm. (a), $\kappa$ as the function of period length $L_p$ at 300 K (blue circles). Triangles correspond to thermal conductivities calculated with Eq. 4.1 and the dashed line denotes the thermal conductivity of pristine NW with the same cross-section. All these conductivities data refer to the left coordinate axis. Green diamonds, corresponding to the relative thermal conductivity decrease with respect to the one of pristine NWs, are referring to the right coordinate axis. (b), $\kappa$ as a function of temperature for pristine and APSLs with specified periods. . . . .	67
4.6	Temperature profile along $z$ direction obtained from NEMD simulations for APSL NWs with periods $L_p = 3$ nm, 6 nm and 18.1 nm, respectively. The arrows indicate the position of interfaces. . . . .	69
4.7	Vibrational density of states obtained with Eq. 4.2 for the Si-C region, the Si-Si region and the C-C region with period $L_p = 18.1$ nm. (a), total VDOS in the three regions; (b), VDOS projected on C atoms in the three regions; (c), VDOS projected on Si atoms in the three regions. . . . .	71
4.8	Inter-atomic potential energies (a) and force constants given by the second derivative of the corresponding potential energies (b) as a function of the inter-atomic distance described by eq. 4.3 and 4.4, respectively. The equilibrium positions obtained from the potential energy minimum are indicated with the dashed lines. The parameters used for this plot is listed in table 4.1. Note that this plot is only valid in the range $r_{ij} < R - D$ . . . . .	72
4.9	Phonon group velocity $v_g$ calculated with Eq. 4.5 of a pristine NW and an APSL NW with $L_p = 1.5$ nm. The diameter is chosen as $D = 2$ nm in order to reduce the number of atoms in the unit cell. . . . .	73

5.1	Schematic of a twin boundary in a diamond lattice. The twin boundary is indicated with the red line and the lattices on the two sides of the twin boundary are mirror-symmetric. Figure from <a href="http://www.tf.uni-kiel.de/matwis/amat/def_en/kap_7/backbone/r7_1_1.html">http://www.tf.uni-kiel.de/matwis/amat/def_en/kap_7/backbone/r7_1_1.html</a> . . . . .	78
5.2	(a) High resolution TEM image of a InP twinning SL nanowire. Long-range superlattice periodicity can be clearly identified. (b) Fourier-filtered high resolution TEM image of the twinning SL in the dashed line box shown in (a). The inset is a space-filling model of the twinning boundary. Figure from Xiong et al Nano Lett. 2006, 6: 2736-2742. . . . .	79
5.3	Schematic figure of the twinning SL phononic metamaterial stacking with diameter $D$ and period length $L_p$ . (a) three possible stacking sites labelled with A, B, and C in closely packed structures. The three sites are identical but are shifted in the $\langle 112 \rangle$ direction one from another; (b) example of hexagon cross section with the diameter $D$ of the twinning SL NWs; (c) stacking sequence of a Si twinning SL NW. . . . .	81
5.4	Temperature profile of the twinning SL phononic metamaterial NW with period $L_p = 5$ nm and diameter $D = 4$ nm. . . . .	83
5.5	(a) Thermal conductivities of the twinning SL phononic metamaterial NWs as a function of the period for different diameters at 300 K. A minimum thermal conductivity appears at different period lengths for different diameters. (b) Period length $L_P$ and shift length $L_s$ corresponding to the minimum thermal conductivity versus the diameter. $L_P$ and $L_s$ are linked together with the relation $L_s = L_p/2 \times \sin(\theta/2)$ . . . . .	84
5.6	Y-Z components of the LA mode vectors around the frequency $4.0 \text{ cm}^{-1}$ for (a) the straight, (b) $L_p = 1.25$ nm, (c) $L_p = 1.9$ nm, and (d) $L_p = 10.6$ nm phononic metamaterial NWs with 2 nm in diameter. The color represents the number of modes and the maximum value has been normalized to 1. The corresponding structures are indicated in each panel. . . . .	86
5.7	Phonon dispersion relation of the pristine NW with $D = 2$ nm (a) and the twinning SL phononic metamaterial NW with $L_p = 3.1$ nm, $D = 2$ nm; (c) and (d) are corresponding zoomed in figures of (a) and (b), respectively. . . . .	88
5.8	Phonon transmission functions calculated with the phonon Green's function vary with the frequency. . . . .	89
5.9	Temperature dependent thermal conductivity of the pristine and twinning SL phononic metamaterial NWs with different periods and a diameter of 4 nm. The corresponding solid lines are fitted with Eq. 5.5 . . . . .	90

5.10	Thermal conductivity variation with the twinning SL period for the Si and the Si/Ge core/shell structures with one- and two-atom thick Ge atom layers. $D = 4$ nm for the pure Si NWs and the Si core in the core/shell NWs. . . . .	92
6.1	Near field heat transfer measurements. (a) experimental data (diamond points) from 13 heat transfer-distance measurements by Narayanaswamy. The dashed line is predicted by proximity approximation, which is far from the experimental data. This comparison indicates the break down of proximity approximation in describing near field radiation. (b) experimental measurement (solid circles) of thermal conductance between a sphere with diameter $40 \mu m$ and a plate by Rousseau. The red line is the prediction with proximity approximation. the comparison clearly shows the perfect agreement between experimental data and theory predictions. Figure from Narayanaswamy et al Phys. Rev. B 2008, 78: 115303 and Rousseau et al Nat. Photonics 2009, 3: 514. . . . .	96
6.2	Thermal conductance between two silica clusters varies with the separation distance by means of molecular dynamics simulation. An interesting transition from heat conduction to radiation is observed. Figure from Domingues et al Phys. Rev. Lett. 2005, 94: 085901. . . . .	98
6.3	Schematics of the silica cluster systems considered in the Green's function calculations (top) and the <i>ab-initio</i> computations (bottom). For Green's function calculation, the clusters are $N \times N \times N$ unit cells cubes with $\text{SiO}_2$ lattice constant of $4.52 \text{ \AA}$ . In <i>ab-initio</i> calculations, two parallel Silica planes separated with different gap distances are used and electron densities inside the gaps are calculated with this model. . . . .	99
6.4	Thermal conductance between two neighboring clusters at 300 K for different cluster sizes versus the distance $d$ indicated in Figure 1. In our calculations, the cluster is a cube $N \times N \times N$ unit cells in volume. The diameter $D$ is set in such a way that the sphere volume is equivalent to that of the simulated cube. The distance $d$ was used as the abscissa instead of the gap distance $l$ in order to discriminate the curves otherwise superimposed. The MD results are taken from Domingues et al Phys. Rev. Lett. 2005, 94: 085901, where the same BKS potential parameters as those adopted in this work were used. . . . .	101
6.5	<i>Ab-initio</i> computation of the electron density generated by two parallel silica films separated by different gap widths. . . . .	104

6.6	Angular frequency dependent cumulative phonon transmission for different gap distance $l$ in the cluster of diameter $D = 1.3$ nm. Inset: phonon transmission function versus angular frequency at low frequencies. . . . .	105
-----	---	-----



# Chapter 1

## Introduction

### 1.1 Energy Challenges

The world's demand for energy is causing a dramatic escalation of social and political unrest. With the development of modern civilizations, the expense of energy has increased progressively and the energy crisis has become a global issue (Snyder and Toberer 2008). World energy demand will expand by 45% between now and 2030 – an average rate of increase of 1.6% per year – with coal accounting for more than a third of the overall rise, as presented in Fig.1.1 (<http://www.energy4me.org/energy-facts/energy-sustainability/>). This latter figure also shows that more than 85% of the world's current energy needs are met through fossil fuels such as coal, oil and natural gas. However, fossil energy will become rare and expensive in a not very distant future. If oil production remains constant until its disappearance, resources will last 42 years. Oil wells produce less as they become depleted which will make it impossible to keep production constant. Similarly, there is enough natural gas to last 61 years and there is enough coal to last 133 years. Also, energy efficiency has yet to impact expectations of rising demand. By improving the efficiency of energy processes, less total energy will be needed to power devices that we use. Besides, a large amount of heat is wasted in factories, home cooking, vehicle driven. Rather than letting this heat escape as wasted energy, it is possible to convert it to another energy like electric power with the help of energy converters.

On the other hand, the consumption of fossil fuels massively produces carbon dioxide, which causes greenhouse effect and changes the global climate. As a result, expansion of economic and clean energy sources will be required, such as nuclear, biomass, other renewables, and unconventional oil. Options like these are part of a concept called energy sustainability.

It goes without saying that sustainable energy is one of the pressing problems

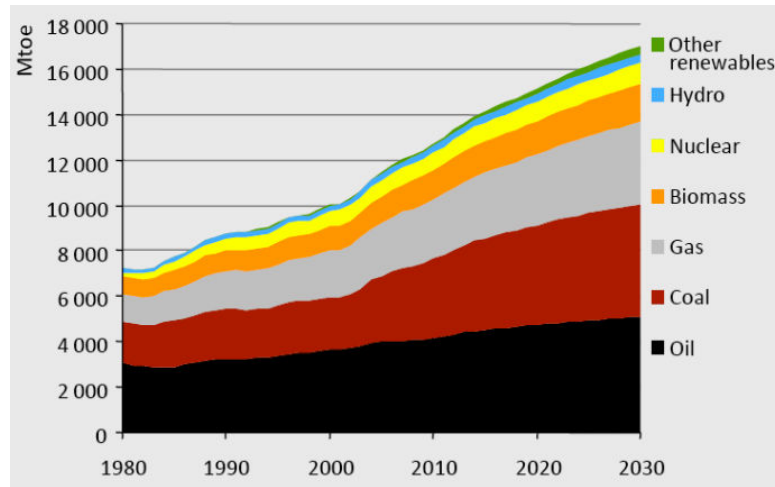


**Figure 1.1:** World energy demand in the past and future 30 years (Source: EIA, *World Energy Outlook 2008*).

facing modern society with materials at the heart of its solutions. Whether it is high-temperature materials for efficient combustion, nanostructures for high-power density batteries, or metastructures for light harvesting, breakthroughs in energy conversion and efficiency have relied on breakthroughs in materials research. What remains to be said, loudly and forcefully, is that society has taken mere baby steps toward a sustainable energy future (Haile 2014).

### 1.1.1 Thermoelectric Materials

Thermoelectric materials, which can generate electricity from waste heat or be used as solid-state coolers, could play an important role in a global sustainable energy solution. Home heating, automotive exhaust, and industrial processes all generate an enormous amount of unused waste heat that could be converted to electricity by using thermoelectrics. As thermoelectric generators are solid-state devices with no moving parts, they are silent, reliable and scalable, making them ideal for small, distributed power generation (Snyder and Toberer 2008; Rowe 1995).

The Seebeck and Peltier effects are the two major phenomena involved in thermoelectric performances. When an electric conductor is subjected to a temperature gradient, a voltage can be generated between the two ends of the conductor, which is known as the Seebeck effect. By using the Seebeck effect, one can convert waste heat to electric power. Inversely, for the Peltier effect, a temperature difference can be obtained when a voltage is applied on the conductor, which allows us to use thermoelectric materials as cooling packages or solid state refrigeration devices.

Thermoelectric devices contain many thermoelectric couples consisting of n-type (containing free electrons) and p-type (containing free holes) thermoelectric elements wired electrically in series through metallic electric contact pads and thermally in parallel as shown in Fig. 1.2. The efficiency of a thermo-

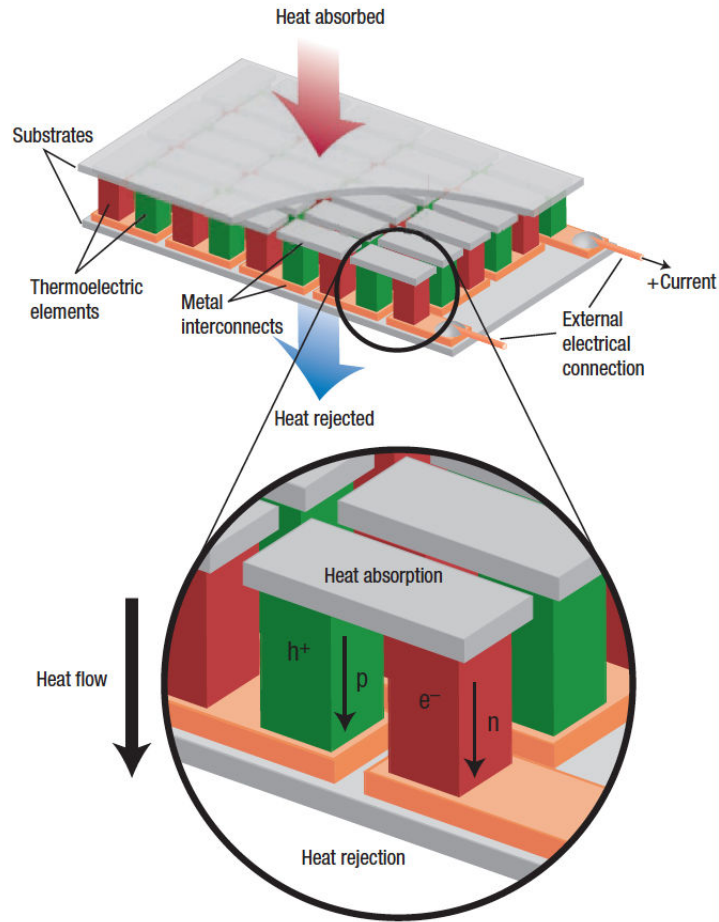


**Figure 1.2:** Schematic of the thermoelectric module for both cooling and power generation. The arrows indicate the direction of charge flow. Figure from G. Jeffrey and Eric S. Toberer, *Nat. Mater.*, 2008, 7: 105

electric material for both power generation and cooling is characterized by the dimensionless figure of merit ( $ZT$ ):

$$ZT = \frac{S^2 \sigma T}{\kappa} \quad (1.1)$$

where  $T$  denotes the absolute temperature.  $\sigma$  and  $S$  are the electrical conductivity and the Seebeck coefficient, respectively.  $\kappa = \kappa_e + \kappa_{ph}$  is the thermal conductivity with  $\kappa_e$  and  $\kappa_{ph}$  being the electronic and lattice thermal conductivities. The  $ZT$  value is expected to be the higher the better. To improve the

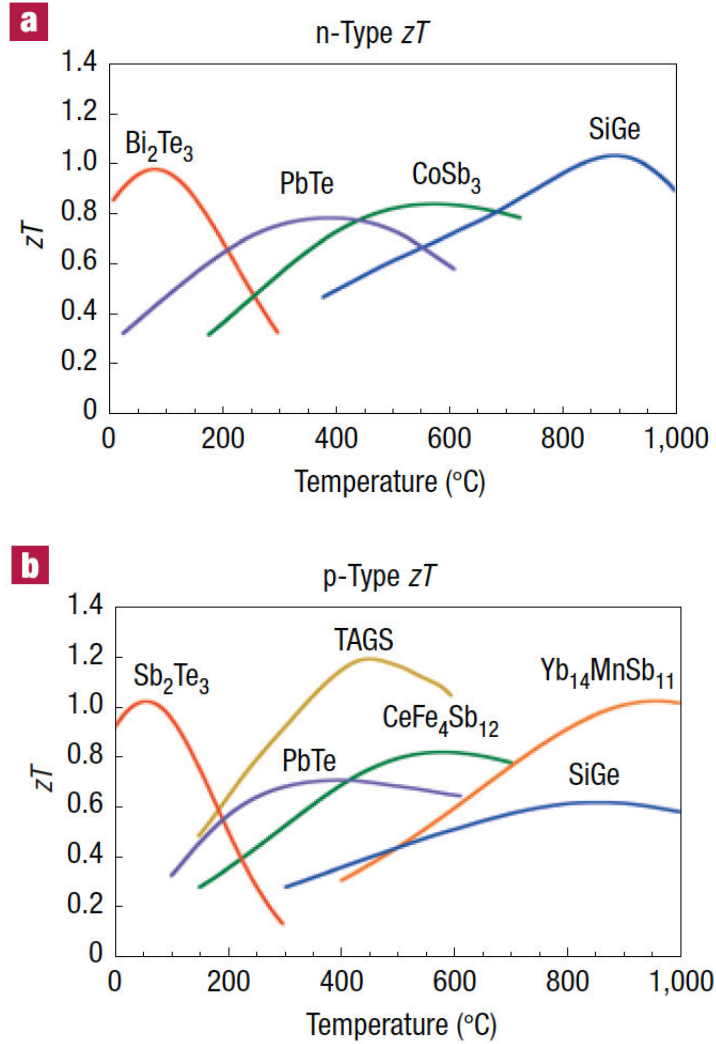


**Figure 1.3:** A summarize of the figure of merit of state-of-the-art for (a) n-type and (b) p-type commercial thermoelectric materials. Figure from G. Jeffrey and Eric S. Toberer, *Nat. Mater.*, 2008, 7: 105

figure of merit, one must therefore maximize the power factor  $S^2\sigma$  and/or minimize the thermal conductivity  $\kappa$ . As  $S, \sigma$  and  $\kappa$  are coupled to each other and as all depend strongly on the detailed electronic structure, carrier concentration, and crystal structure, the task of finding new compounds with large values of  $ZT$  is extremely difficult (Madsen 2006). The best thermoelectric materials to date have  $ZT$  between 1 and 2; however  $ZT \sim 4$  is needed for competitive power generation. The figure of merit of state-of-the-art commercial thermoelectric materials for both n-type and p-type has been summarized in Fig. 1.3. Since 1960s, only slow progress has been made in enhancing figure of merit, either

in the widely used  $\text{Bi}_2\text{Te}_3$  alloys or in other thermoelectric materials. Until 1993, a pioneering work was done by Hicks and Dresselhaus (Hicks and Dresselhaus 1993), where they theoretically showed that  $ZT$  can be enhanced with nanostructured materials. In nanomaterials, the electrons can be confined in a quantum well, as a result, the Seebeck coefficient can be largely enhanced. In the meantime, the numerous boundaries in nanomaterials can significantly increase the scattering of phonons. As a result, the phonon mean free path will be shortened dramatically, which makes the thermal conductivity to be suppressed to a large extent. Stimulated by their ideas, excellent figures of merit have been realized in different systems including  $\text{Bi}_2\text{Te}_3/\text{Sb}_2\text{Te}_3$  superlattices (Venkatasubramanian et al. 2001),  $\text{PbSe}_{0.98}\text{Te}_{0.02}/\text{PbTe}$  quantum dot superlattices (Harman et al. 2002), quantum nanodot bulk  $\text{AgPb}_m\text{SbTe}_{2+m}$  alloys (Hsu et al. 2004), and  $\text{SrTiO}_3/\text{SrTi}_{0.8}\text{Nb}_{0.2}\text{O}_3$  superlattices (Ohta et al. 2007).

On the other hand, high figures of merit have also been obtained in recent years with heavy elements doping. For example, filled skutterudite antimonides  $\text{La}_{0.9}\text{Fe}_3\text{CoSb}_{12}$  ( $ZT=0.9$  at 750 K) (Sales et al. 1996),  $\text{Zn}_4\text{Sb}_3$  ( $ZT=1.3$  at 670 K) (Snyder et al. 2004), and half-Heusler alloys (Poon 2001). These developments have essentially been derived from chemical manipulation, on the basis of the guiding principle of the use of heavy elements as constituents to reduce the thermal conductivity. Due to the excellent thermal stability, transition metal oxides have attracted growing attention for thermoelectric power generation at high temperatures. However, the large thermal conductivity (3-10 W/mK) of metal oxides originating from the high phonon frequencies of  $\text{O}^{2-}$  ions (Touloukian et al. 1970) makes it a great challenge for the realization of  $ZT \sim 2$  (Ohta et al. 2007). As a result, one of the key points for improving the figure of merit is to suppress the thermal conductivity.

### 1.1.2 Thermal Interface Materials

With the development of nanotechnology in recent decades, electronic devices continue to scale down in dimension and scale up in power density (increasing processing speeds and higher frequencies). The excessive heat generated during operation not only harms their performance, but also degrades the performance and reliability of the overall system and can cause system failure. As a result, thermal management becomes a critical issue to ensure high device performance (Ni et al. 2012).

Roughness is inevitably existing on the surface of materials. When two solid surfaces are apparently in contact, they actually touch each other only at a few individual spots while other spaces are filled by air. Consequently, the heat is constrained to flow through the sparsely spaced actual contact spots (Fig. 1.4) and the insulating air gaps created by multiple voids of "contacting" hard surfaces are large thermal barriers. The discontinuity of heat flow at the interface

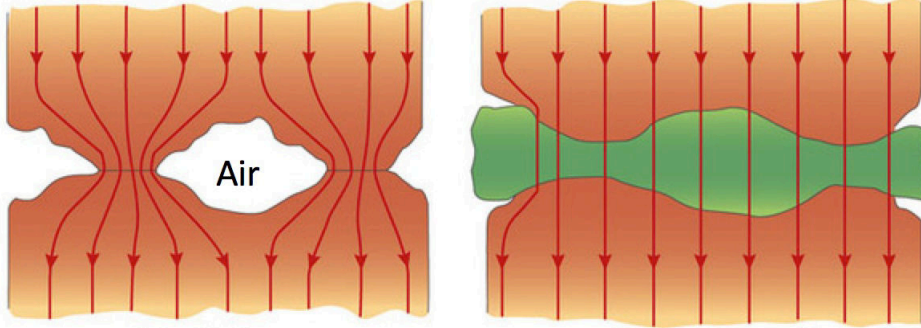


**Figure 1.4:** Schematic of a rough interface with (right) and without (left) thermal interface material filling. Heat can only propagate through sparse spots when no thermal interface material is used while heat can dissipate through the entire interface when a thermal interface material is filled. Figure from internet (<http://www.bit-tech.net/hardware/2009/02/16/all-about-tim/>)

of different components in the system makes the thermal management even more complicated. To reduce the thermal interface resistance, a third medium is usually used to fill the space between the two solids to eliminate these interstitial air gaps from the interface by conforming to surface irregularities and uneven mating surfaces (Fig. 1.4). This kind of conducting media is usually referred as thermal interface materials (TIMs). Extreme compliance of TIMs reduces component stress while higher thermal conductivity provides thermal performance required for next generation designs that continue to pack more power into smaller spaces. The TIMs are used in many applications such as notebook computers, mass storage devices, and audio and video components. It has been theoretically shown by Yovanovich et al. (Yovanovich et al. 1997) that simply replacing air with Si grease between aluminum/ceramic interface can reduce the thermal resistance by a factor of five.

An efficient thermal interface material should be highly thermal conducting itself and also should have a small contact resistance between itself and the host materials. The total thermal resistance  $R_{Total}$  for heat flowing from one solid to another by crossing the TIMs can be written as follows:

$$R_{Total} = R_1 + R_{TIM} + R_2 \quad (1.2)$$

where  $R_1$  and  $R_2$  are the thermal resistances between the TIMs and solid 1, the TIMs and solid 2, respectively.  $R_{TIM} = \frac{t}{\kappa_{TIM}}$  represents the resistance of the TIMs with  $t$  and  $\kappa_{TIM}$  being the thickness and the thermal conductivity of TIMs, respectively.

Based on the principle of high efficiency, ease of use in assembly, and long-term stability/reliability, several types of TIMs, including greases, elastomeric pads,

phase change materials, thermal tapes, thermally conductive adhesives and so on, has been developed in response to the changing needs of the electronic packaging market.

### 1.1.3 Thermal Diode Materials

Analogously to electric diode, a thermal diode that provides an asymmetric heat conduction is one of the most important building blocks for phononics (Wang and Wu 2014). It has become a focus since the theoretical models where clear physical underlying mechanisms and great performances were proposed from nonlinear lattices in the past decade (Terraneo et al. 2002; Li et al. 2004; Li

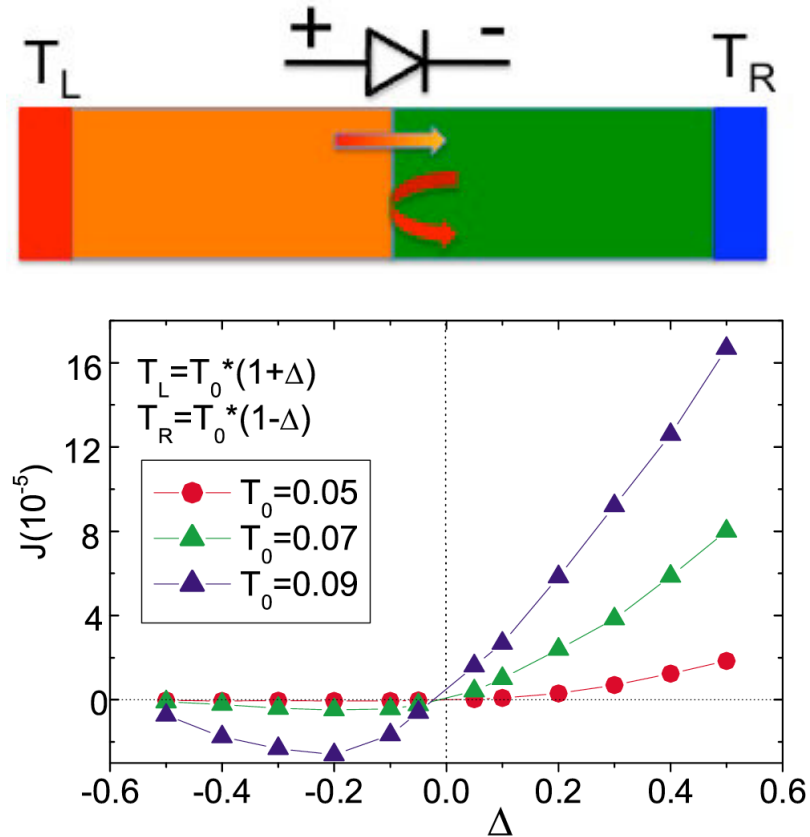


**Figure 1.5:** Sketch of the thermal diode module (up) and the heat current vs the relative temperature bias behavior of a thermal diode (down). Figure from Li, Lan and Wang, 2005, *Phys. Rev. Lett.* 95: 104302

et al. 2005; Hu et al. 2006). The concept of thermal diode involves, just as in its electronic counterpart, the presence of a symmetry-breaking mechanism. This symmetry breaking is most conveniently realized by merging two materials

exhibiting different heat transport characteristics.

Fig 1.5 shows the module of a thermal diode composed by the junction between two dissimilar materials and the heat rectification with the change of temperature difference. It can be clearly seen that when a positive temperature bias ( $T_L > T_R$ ) is applied, the heat current gradually increases with increasing of the temperature difference  $\Delta$ , i.e., the setup behaves as a "good" thermal conductor. However, when a negative temperature bias ( $T_L < T_R$ ) is applied, most of the heat is reflected at the interface and the transmitted heat is almost zero. The two-segment structure thus behaves as a "poor" thermal conductor. This rectification behavior is explained with the overlap of the power spectra of the two junction materials (Li et al. 2004). If the power spectrum in one part of the device matches the one in the neighbouring part, heat energy is exchanged efficiently. In the absence of such overlapping spectral properties, the exchange of energy becomes strongly diminished. In particular, the response behavior of realistic materials is typically anharmonic by nature. As a consequence, the corresponding power spectra become strongly dependent on temperature. If an asymmetric system is composed of different parts with different physical parameters, the resulting temperature dependences of the power spectra will differ likewise (Li et al. 2012). This match or mismatch of spectral properties provides the salient mechanism for thermal rectification.

Because the power spectra of an arbitrary nonlinear material typically become temperature dependent, any asymmetric nonlinear system is expected to display an inequivalent heat transport upon reversal of the temperature bias. Experimentally, the thermal rectification has been realized with mass-loading carbon nanotubes (CNTs) and boron nitride nanotubes (BNNTs) by Chang (Chang et al. 2006). In their experiments, CNTs and BNNTs were firstly synthesized and then trimethyl-cyclopentadienyl platinum ( $C_9H_{16}Pt$ ) was deposited non-uniformly along the length of the nanotubes in an attempt to achieve the non-uniform mass-loading geometry (Fig. 1.6). Thermal rectification of the nanotube is obtained as:

$$Rectification = \frac{K_{H \rightarrow L} - K_{L \rightarrow H}}{K_{L \rightarrow H}} \times 100 \quad (1.3)$$

where  $K_{L \rightarrow H}$  and  $K_{H \rightarrow L}$  are the thermal conductances of the nanotube when heat flows from the low-mass to high-mass ends or from the high-mass to low-mass ends, respectively. As can be seen from Fig. 1.6, no thermal rectification is observed with the pristine NTs while after the mass-loading, a clear thermal rectification is achieved.

Except for the mass asymmetric nanostructures, the geometrically asymmetric nanostructures based thermal rectifiers were also extensively studied. For instance, carbon nanocones exhibiting a high asymmetric geometry was found to

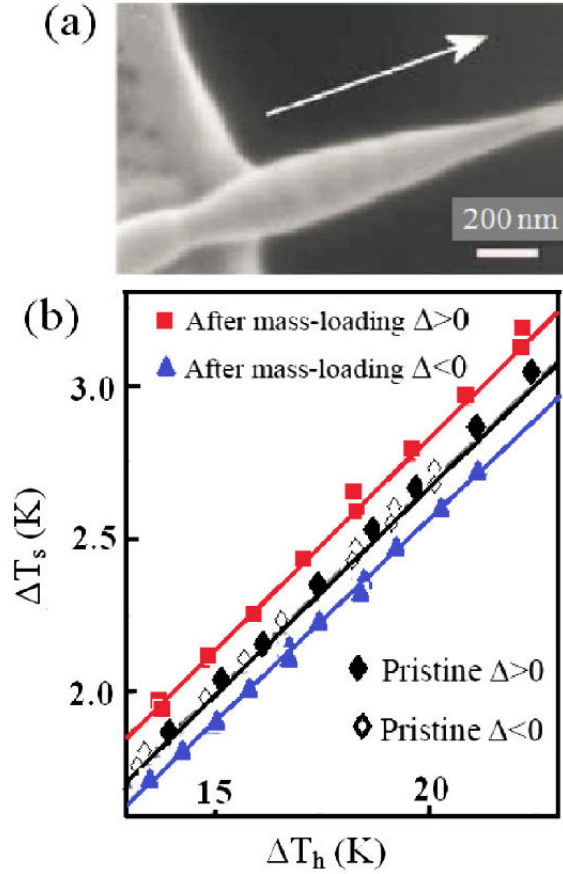


**Figure 1.6:** *Experimental realization of thermal rectification with mass-loading nanotubes. (a) Scanning electron microscope images of BNNTs after deposition of  $C_9H_{16}Pt$ . (b) Sensor temperature ( $\Delta T_s$ ) vs heater temperature ( $\Delta T_h$ ) for the NTs before and after deposition of  $C_9H_{16}Pt$ . Figure from Chang, Majumdar, and Zettl, 2006 Science, 314: 1121*

be a good thermal diode material (Yang et al. 2008). In order to compare the impact of mass asymmetry versus geometry asymmetry for thermal rectification, the same nanocone with a graded mass distribution was simulated. The results yield a rectification ratio of 10% in the uniformed mass case and 12% in the the mass-graded nanocone. This 2% increase for the mass-graded distribution evidences the role of geometric asymmetry as more effective in boosting thermal rectification (Yang et al. 2008).

#### 1.1.4 Thermal Cloak Materials

Transformation optics has made a major contribution to the advancement of modern electromagnetism and related research assisted by the development of metamaterials (Ma et al. 2013). Recently, many significant achievements of

invisibility cloaking have been achieved hitherto, owing to the pioneering theoretical proposals of Pendry (Pendry et al. 2006) and Leonhardt (Leonhardt 2006). On the basis of the invariance of heat conduction equation under coordinate transformations, transformation thermodynamics has provided a new method to manipulate heat flux at will (Han et al. 2013). The most attractive application is the thermal cloaking: making the temperature of a certain region invariant.

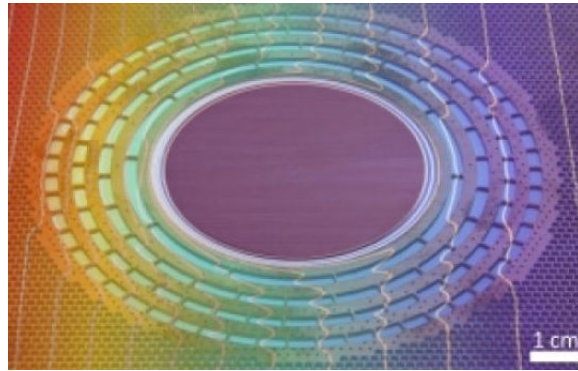


**Figure 1.7:** *Thermal invisibility cloak: Heat is passed around the central area from the left to the right. Temperature characteristics (white lines) remain parallel. Figure from internet: <http://www.sciencedaily.com/releases/2013/05/130508092924.htm>*

If a simple, solid metal plate is heated at the left edge, heat migrates uniformly to the right side. The temperature of the plate decreases from the left to the right. For a thermal cloak, for example, a metamaterial consisting of copper and silicon outside of the annular structure illustrated by Schittny et al (Schittny et al. 2013), exactly the same behavior is exhibited and no heat penetrates inside the annular structure. Outside, there is no indication of what happens inside, as shown in Fig.1.7. Clearly, by design, the cloak recovers the overall downstream heat flow of the homogeneously perforated plate under transient as well as under static conditions. It is important to stress that thermal cloaks cannot violate the classical laws of thermodynamics, which are still strictly preserved. Therefore, in the static or long-time limit, due to the finite heat conductivity of the innermost isolating ring, the to-be-protected inner region does eventually heat up. Hence, thermal protection works only transiently, as pointed out by Schittny et al.

Thermal invisibility cloaks are a rather new field in fundamental research. In the long term, they might be applied in areas needing effective heat management, such as in microchips, electric components, or machines.

As illustrated by the examples of the above sections, it is of vital importance to *control the heat transfer or manipulate phonons* as demanded by nowadays

technologies. Different thermal transport behaviours are needed for different applications (low thermal conductivity for thermoelectrics, high thermal conductivity for interface materials, preferred heat flow orientations for thermal diode and so on). So, it is essential to *design new structures* which allow us to control the heat transfer in a given point of view so as to feed back targeted applications.

## 1.2 Scientific Background

### 1.2.1 Lattice Vibrations and Phonons

In most solid materials, atoms or molecules are arranged in a regular array of sites, or points in a three-dimensional space, which is known as the crystal lattice. A crystal structure describes a highly ordered structure, occurring due to the intrinsic nature of molecules to form symmetric patterns. At any finite temperature, atoms vibrate about their equilibrium positions. Under the classical approximations, those atom motions can be mathematically described by the Newton's second law if the force applied on each atom and the atomic mass are known.

To simplify the formulation, we consider here an one-atomic chain with lattice parameter and atomic mass denoted as  $a$  and  $M$  as illustrated in Fig. 1.8. To describe the interatomic forces, we introduce a potential energy labelled as  $V$ , which is the function of the positions of all atoms and we assume that only the nearest-neighbours interact with each other. Expanding  $V$  around the equilibrium position according to Taylor series yields

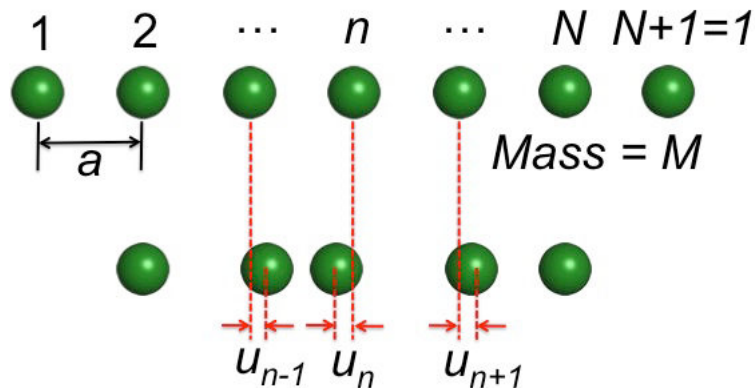


**Figure 1.8:** An one-atomic chain with the lattice constant  $a$  and mass  $M$  at the equilibrium position (up) and with a displacement for each atom (down)

$$V(\vec{u}) = V_0 + \frac{1}{2} \sum_{nk} u_n u_k \frac{\partial^2 V}{\partial u_n \partial u_k} + \frac{1}{3!} \sum_{nkl} u_n u_k u_l \frac{\partial^3 V}{\partial u_n \partial u_k \partial u_l} + \dots \quad (1.4)$$

where  $\vec{u} = (u_1, u_2, \dots, u_n, \dots, u_N)$  and  $u_n$  are the displacements off equilibrium of the  $n^{\text{th}}$  atom (Fig. 1.8). Since we are dealing with the problem around equilibrium positions, the first derivative of the potential in Eq. 1.4  $\partial V / \partial u_n = 0$ . The constant energy term  $V_0$  is arbitrary, and will be set to zero. Let  $K = \frac{\partial^2 V}{\partial u_n \partial u_k}$  represents the force constant between the  $n^{\text{th}}$  and  $k^{\text{th}}$  atoms and ignoring the third and higher orders of the potential energy in Eq. 1.4, the equation of motion can be easily casted as:

$$M\ddot{u}_n = K(u_{n-1} + u_{n+1} - 2u_n) \quad (1.5)$$

We call this relation the atomic motion equation in the *harmonic approximation* because it only includes the *harmonic force terms*. We now decompose the displacements into a set of normal modes with the plane wave form, i.e.,  $u_n = A_0 e^{i(qna - \omega t)}$ . Substituting  $u_n$  into the equation of motion, we derive

$$-\omega^2 M = K(e^{iqa} + e^{-iqa} - 2) \quad (1.6)$$

As a result, the relationship between the wave vector  $q$  and the frequency  $\omega$  can be obtained as:

$$\omega = \sqrt{\frac{4K}{M}} \left| \sin \frac{1}{2} qa \right| \quad (1.7)$$

This relation is called the *dispersion relation*.

The Hamiltonian of the system can be written as:

$$H = \frac{1}{2m} \sum_n p_n^2 + \frac{1}{2} K \sum_n (2u_n^2 - u_n u_{n+1} - u_n u_{n-1}) \quad (1.8)$$

where  $p_n$  is the momentum of the  $n^{\text{th}}$  atom. Let's transform the displacements and the momenta into coordinates of the reciprocal space with Fourier series:

$$U_q = \frac{1}{\sqrt{N}} \sum_n u_n e^{iqn} \quad P_q = \frac{1}{\sqrt{N}} \sum_n p_n e^{-iqn} \quad (1.9)$$

The corresponding inverse transform reads as:

$$u_n = \frac{1}{\sqrt{N}} \sum_q U_q e^{-iqn} \quad p_n = \frac{1}{\sqrt{N}} \sum_q P_q e^{iqn} \quad (1.10)$$

Substituting Eq. 1.10 into the Hamiltonian expression 1.8 and simplifying it, one obtains (Ziman 1960):

$$H = \frac{1}{2M} \sum_q P_q P_{-q} + K \sum_q U_q U_{-q} (1 - \cos q) \quad (1.11)$$

The states labelled with  $q$  and  $-q$  corresponding to running waves in the opposite directions. It can be easily find from the Fourier transform (Eq. 1.9) that the pairs  $P_q - P_{-q}$  and  $U_q - U_{-q}$  are complex conjugate to each other, i.e.,  $P_q^* = P_{-q}$ ,  $U_q^* = U_{-q}$ . So Eq. 1.11 can be recasted as:

$$H = \frac{1}{2} \sum_q \left\{ \frac{1}{M} P_q P_q^* + 2K(1 - \cos q) U_q U_q^* \right\} \quad (1.12)$$

Let's now introduce the second coordinate operators,  $a_q$  and  $a_q^*$ , which are defined in terms of  $P_q$  and  $U_q$  by the relations:

$$\begin{aligned} a_q &= \sqrt{\frac{1}{2m\hbar\omega}} P_q - i \sqrt{\frac{K(1 - \cos q)}{\hbar\omega}} U_q^* \\ a_q^* &= \sqrt{\frac{1}{2m\hbar\omega}} P_q^* + i \sqrt{\frac{K(1 - \cos q)}{\hbar\omega}} U_q \end{aligned} \quad (1.13)$$

It can be shown that the commutation relations of the above defined operators have the specially simple form

$$[a_q, a_q^*] = (i/2\hbar) \{ [P_q, U_q] + [P_q^*, U_q^*] \} = 1 \quad (1.14)$$

consequently the Hamiltonian reduces to

$$H = \sum_q \hbar\omega \left( a_q^* a_q + \frac{1}{2} \right) \quad (1.15)$$

The operators defined in Eq. 1.13 are known as the *annihilation* and *creation operators*. And  $n_q \equiv a_q^* a_q$  is called the number operator, whose eigenstates are characterized by sets of positive integers which tell us the number of 'particles' present in the field, or the number of *quanta* in the particular mode. So the total energy in the system is quantized with the quantum energy of  $\hbar\omega$ . Having analysed the motion into quanta distributed over the various modes, we find it convenient to give to each of such quantum the name of *phonon*. *Phonons* bear exactly the same relation to the vibrations of the solid as do *photons* to the vibrations of the electromagnetic field. We sometimes talk of them as if they are particles ('phonon gas'), but this is only in the Pickwickian sense. Unlike

the atoms which make up an ordinary gas, thermal phonons can be created and destroyed by random energy fluctuations. In the language of statistical mechanics this means that the chemical potential for adding a phonon is zero.

The phonon states comply to the Boltzmann definition of entropy and as those states exist within the canonical ensemble, the distribution of phonons are governed by the Bose-Einstein statistics, which reads as

$$f_{BE} = \frac{1}{\exp(\frac{\hbar\omega}{k_B T}) - 1} \quad (1.16)$$

where  $k_B$  is the Boltzmann constant, and  $T$  is the absolute temperature.

In Eq. 1.7, we have derived the phonon dispersion relation of the one-atomic chain. In the one-atomic chain case, the phonon dispersion has only one branch as the primitive cell contains only one degree of freedom. In the usual case, if there are more than one atoms in the primitive cell, the phonon dispersion has  $D \times N$  branches, where  $N$  is the number of atoms in the primitive cell and  $D$  denotes the degree of freedom of each atom. Among the  $DN$  branches, there are  $D$  acoustic branches having the frequency equalling to zero at the Brillouin zone center ( $\Gamma$  point,  $q = 0$ ) and  $(DN-D)$  optical branches. The acoustic branches describe the displacement of the primitive cell as a whole while the optical branches describe the relative displacement of the atoms in the primitive cell. Similar to the one-atomic chain, the phonon dispersion relation of the diatomic chain with atomic masses  $M_1$  and  $M_2$  can be easily obtained as follows:

$$\begin{aligned} \omega_{\pm}^2 &= K\left(\frac{1}{M_1} + \frac{1}{M_2}\right) \pm K\sqrt{\left(\frac{1}{M_1} + \frac{1}{M_2}\right)^2 - \frac{4\sin^2(qa/2)}{M_1M_2}} \\ &= \frac{K(M_1 + M_2)}{M_1M_2} \left\{1 \pm \left[1 - \frac{4M_1M_2}{(M_1 + M_2)^2} \sin^2(qa/2)\right]^{1/2}\right\} \end{aligned} \quad (1.17)$$

The phonon dispersion of the diatomic chain described by Eq. 1.17 is depicted in Fig. 1.9(a). The maximum frequency (cut off frequency) is known as the Debye frequency, which links with the Debye temperature  $\Theta$  according to the relation  $\Theta = \frac{\hbar\omega}{k_B}$ . According to the phonon dispersion relation, the phonon group velocity  $v_g$ , which is defined as the first derivative of the frequency  $\omega$  with respect to the wave vector  $q$ , i.e.,  $v_g = \frac{d\omega}{dq}$ , can be obtained (Fig. 1.9(b)). We now discuss two limit situations, i.e., at the Brillouin zone center  $qa \ll 1$  and at the Brillouin zone boundaries  $qa = \pm\pi$ .

At the Brillouin zone center,  $qa \ll 1$  and the dispersion relation described by Eq. 1.17 can be simplified as follows by considering the relationships  $\sin x \approx x$

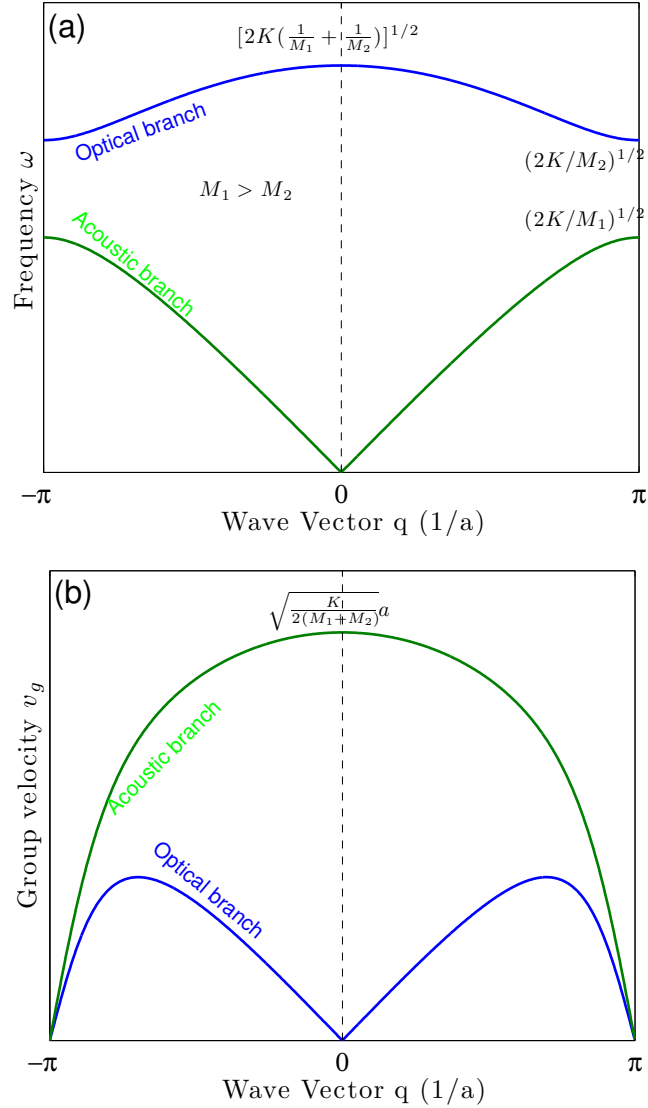


**Figure 1.9:** (a) Phonon dispersion curve and (b) phonon group velocity of the diatomic chain

and  $\sqrt{1-x} \approx 1 - \frac{1}{2}x$  when  $x \ll 1$ :

$$\begin{aligned} \omega^2 &\approx 2K\left(\frac{1}{M_1} + \frac{1}{M_2}\right) && \text{(optical branch)} \\ \omega^2 &\approx \frac{K}{2(M_1 + M_2)}q^2a^2 && \text{(acoustic branch)} \end{aligned} \quad (1.18)$$

This derivation provides a constant frequency and a linear dependence of frequency on  $q$  for the optical and acoustic phonons, respectively, which means

that the group velocity is zero for the optical phonons and a non-zero constant for the acoustical phonons (Fig. 1.9(b)). The non-zero constant velocity for acoustic phonons is known as the sound velocity in materials.

On the Brillouin zone boundary,  $qa = \pm\pi$  and Eq. 1.17 is reduced to:

$$\begin{aligned}\omega^2 &= 2K/M_2 && \text{(optical branch)} \\ \omega^2 &= 2K/M_1 && \text{(acoustic branch)}\end{aligned}\tag{1.19}$$

It comes out that the frequencies for both acoustic and optical modes are constants and the corresponding phonon modes are non-propagative.

### 1.2.2 Phonon Transport in Nanoscale

Phonon transport in nanostructures can be largely different from the situation in bulk and strongly depends on the system size. New phenomena such as phonon confinement, anomalous heat transport, breakdown of Fourier law, and quantization of thermal conductance emerge when the size is reduced to nanoscale. These new behaviours are of great importance for both fundamental considerations and modern technologies.

**Boundary Scattering and Confinement:** When the size of a material decreases, the density of boundary or interface increases dramatically. As a result, phonon boundary scattering is of key importance and the thermal conductivity in nanoscales could be one order of magnitude smaller than the one of the bulk material (Li et al. 2003). The scattering of phonons on the crystal boundaries has been known since the pioneering work of Casimir (Casimir 1938), but for many years it was thought to be essentially a low-temperature phenomenon. The strong boundary scattering can shorten the phonon mean free path  $\Lambda$  to the order of the size of systems. Let's take a cylindrical nanowire with diameter  $D$  for example, if the asperity of the surface is large, then the boundary scattering is purely diffusive. When the diameter  $D$  is smaller than the bulk mean free path  $\Lambda_{bulk}$ , the mean free path in the nanowire will be given by the diameter  $D$ .

When phonons scatter with a boundary, none of them will be transmitted and all of them will be reflected. Those backscattered phonons will interact with the incoming phonons and form a standing wave. This phenomenon is called *phonon confinement*. The group velocity of the confined phonons is zero, hence, they do not propagate heat.

**Anomalous Heat Transport:** Traditionally, the phenomenon of heat conduction is believed to follow the Fourier's law

$$J = -\kappa \nabla T\tag{1.20}$$

where  $J$  refers to the heat flux density in the system,  $\nabla T$  is the gradient of temperature and the coefficient  $\kappa$  is defined as the thermal conductivity, which is the intrinsic property of a material. Although the Fourier's law has met a great success in describing macroscopic heat transport in the past 200 years, recent studies of thermal conductivity in low dimensional systems show the breakdown of the Fourier's law and anomalous heat transport occurs (Liu et al. 2012). Theoretically, the findings that contradict our traditional understandings is that the thermal conductivity typically diverges with the system size (Liu et al. 2012; Lepri et al. 1997; Lepri, S. et al. 1998; Dhar 2001; Grassberger et al. 2002):

$$\kappa \sim L^\beta \quad (\beta > 0) \quad (1.21)$$

for one dimensional (1D) models and

$$\kappa \sim \log L \quad (1.22)$$

for two dimensional (2D) models. These models predict a very large thermal conductivity for low dimensional systems with large  $L$ .

Experimentally, Chang et al (Chang et al. 2008) measured the thermal conductivities of fully suspended multi-wall CNTs and BNNTs as the functions of NT length, where they found the violation of the Fourier's law even if  $L \gg \Lambda$ . By fitting their experimental data with Eq. 1.21, the  $\beta$  values are found to be 0.6-0.8 for CNTs and 0.4-0.6 for BNNTs. By using non-equilibrium molecular dynamics (NEMD) simulations, the length dependence of the thermal conductivity of SiNWs has been studied by Yang et al (Yang et al. 2010). It is found that the thermal conductivity of SiNWs increases with the length as  $\kappa \propto L^\beta$ , even when the wire length is as long as  $1.1 \mu m$ . The  $\beta$  value is found to be different in different length regimes. At room temperature, when SiNW length remains less than 60 nm, the thermal conductivity increases linearly with the length ( $\beta \approx 1$ ). For the SiNW with a length larger than 60 nm, the divergence exponent  $\beta$  reduces to 0.27. In addition, this divergence exponent  $\beta$  also depends on temperature. At 1000 K,  $\beta$  value is only 0.15 when the NW length is longer than 60 nm. The reduction of  $\beta$  is ascribed to the stronger phonon-phonon interactions at high temperatures.

**Quantized Thermal Conductance:** The thermal conductance of phonon waveguides in the ballistic, one-dimensional limit can be calculated using the Landauer formula. This approach leads to an expression for the reservoir-to-reservoir heat current  $J_{th}$  taking the form (Schwab et al. 2000; Yamamoto and Watanabe 2006):

$$J_{th} = \sum_m \int_0^\infty \frac{dk}{2\pi} \hbar \omega_m v_m [f_{hot} - f_{cold}] T r_m \quad (1.23)$$

where  $m$  is the phonon branch index,  $\omega_m$  and  $v_m$  are the frequency and group velocity of the  $m^{\text{th}}$  branch,  $f$  represents the Bose-Einstein occupation factor for the two (hot/cold) thermal reservoirs, and  $Tr_m$  is the transmission coefficient of the  $m^{\text{th}}$  branch. In the nanowire case, the group velocity can be cancelled with the density of states and Eq. 1.23 can be easily converted to an integral over frequency  $\omega$ . Let  $x = \hbar\omega/k_B T$  and in the limit of small temperature differences between the hot and the cold reservoirs, the thermal conductance  $\sigma = J_{th}/(T_{hot} - T_{cold})$  is given by

$$\sigma(T) = \frac{k_B^2 T}{h} \int_0^\infty dx \frac{x^2 e^x}{(e^x - 1)^2} Tr(k_B T x / \hbar) \quad (1.24)$$

In the low temperature limit, i.e., when  $T \rightarrow 0$ , only four acoustic phonon branches (one dilatational, one torsional, and two flexural) contribute to the conductance. For the ideal coupling between the ballistic thermal conductor and the reservoirs, yielding the transmission coefficient,  $Tr_m$ , to equal unity. Eq. 1.24 leads to a quantized thermal conductance  $\sigma_0$  defined as

$$\sigma_0 = \frac{\pi^2 k_B^2 T}{3h} \quad (1.25)$$

an expression devoided of any material related parameters. This quantum of thermal conductance,  $\sigma_0 = (9.456 \times 10^{-13} \text{W/K}^2)T$ , represents the maximum possible value of energy transported per phonon branch. Surprisingly, it does not depend on particle statistics, but is universal for fermions, bosons and anyons (Rego and Kirczenow 1999; Krive and Mucciolo 1999).

Differing from the electrical conductance quantization, a factor of  $T$  is included in Eq. 1.25, which provides to the thermal conductance quantum a linear dependence upon temperature. This reflects the fact that the transported quantity is energy (that is, entropy times temperature). In the case of electronic conduction, the corresponding quantity is the electron charge,  $e$ , and the electrical conduction quantum per spin-degenerated band is temperature independent,  $\sigma_0^e = 2e^2/h$ . The thermal conductance quantization has been experimentally observed by Schwab et al (Schwab et al. 2000) in suspended insulating nanostructures at very low temperatures. Fig. 1.10 shows the measured thermal conductance versus temperature, where a conductance plateau appears when the temperature is lower than 0.8 K, indicating the quantization of the thermal conductance.

### 1.2.3 Phonon Engineering with Defects

In materials science and engineering, defects are of vital importance in mechanical, electronic, optical, thermal and many other properties design. Usually,

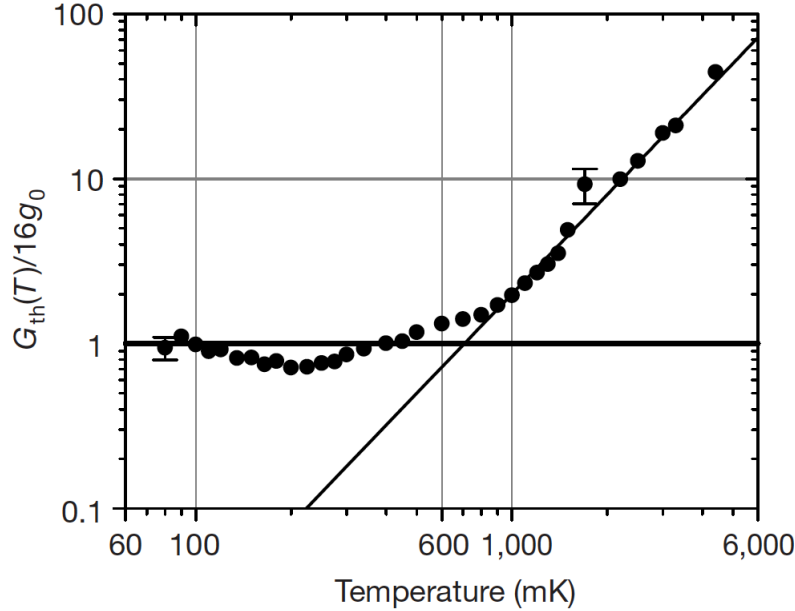


**Figure 1.10:** Experimentally measured normalized thermal conductance with the change of temperature. When the temperature is below 0.8 K, a saturation in conductance at a value near the expected quantum of thermal conductance. Figure from K. Schwab et al. *Nature* (2000) 404: 974.

crystal defects can be classified into 3 types: point defects, line defects, and plane defects. Since phonons are tightly linked with lattice vibrations, lattice imperfection will have a large impact on phonon transport.

The point defects such as vacancies and isotopes can produce localized modes around the vacancy and these localized modes can interact with the running phonons, especially with optical phonons which have shorter wavelength. For example, the thermal conductivity of the room temperature thermoelectric material  $\text{Bi}_2\text{Te}_3$  with Bi and Te vacancies has been studied by Termentzidis et al. (Termentzidis et al. 2013) and the results for thermal conductivity are shown in Fig.1.11. It is found that the thermal conductivity of bismuth telluride decreases both in the presence of Bi and Te vacancies. The decrease is greater than 60% when the bismuth vacancy concentration is 5% and it is greater than 70% for a tellurium vacancy concentration of 4%.

The presence of line defects, usually referring to the edge or screw dislocations, will produce non-uniformed strain in materials. Calculating the thermal conductivities in materials with dislocations is rather complicated because of the anisotropic nature of the displacement field. A dislocation usually can be divided into two parts, i.e., the core region undergoing a plastic deformation and having a volume limited by the radius  $r = b$ , where  $b$  is the magnitude

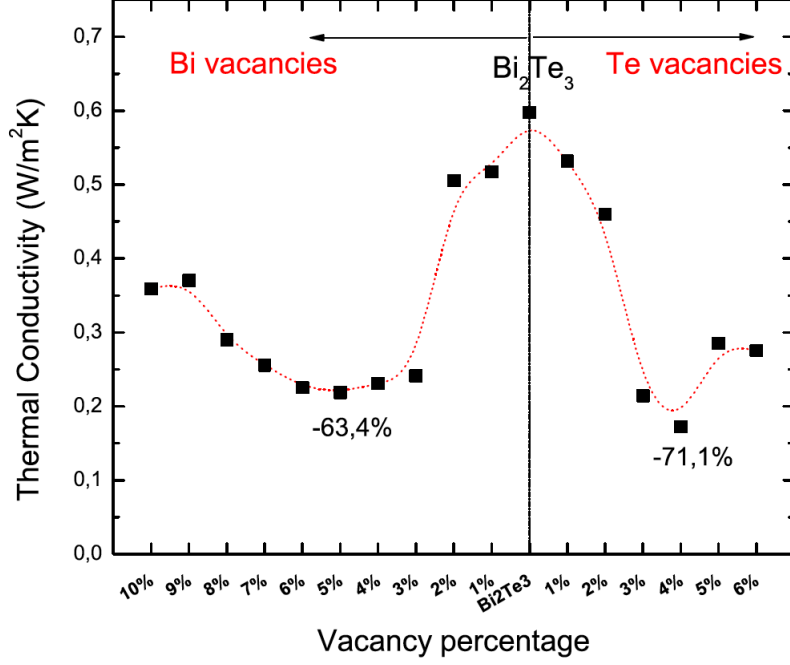


**Figure 1.11:** Calculated thermal conductivity for defected bulk  $Bi_2Te_3$  as a function of the vacancy concentration. Left side of the figure corresponds to  $Bi_{40-x}Te_{60}$  and right side to  $Bi_{40}Te_{60-y}$ . Figure from Konstatinos et al. *J. App. Phys.* (2013) 113: 013506

of the Burger's vector; the shell region with elastic deformation exists in the volume defined by  $r > b$ . The well known method for estimating the impact of dislocation on thermal conductivity is given by Klemens (Carruthers 1961). In Klemens' theory, the specific scattering by the core is in general small due to the small size of this region and it can be modelled as a row of vacancies. The relaxation time is given by  $1/\tau \propto \omega^3$ . In the shell region, the strain field has a very long range. One can approximate the relaxation time as follows according to the elastic theory:

$$\begin{aligned} \frac{1}{\tau} &\approx C\rho b^2 q && \text{(Edge dislocation)} \\ \frac{1}{\tau} &\approx \rho\gamma^2 b^2 \omega && \text{(Screw dislocation)} \end{aligned} \quad (1.26)$$

where  $C$  is defined as a constant related to materials properties, such as the elastic constant and the sound velocity,  $\rho$  is the dislocation density,  $q$  and  $\gamma$  represent the wave-vector and the Grüneisen parameter.

The plane defects are two dimensional crystal imperfections and have different types. Any interface or boundary in crystals such as twinning boundaries, grain boundaries, and heterostructure interfaces can be regarded as plane defects.

Plane defects can scatter phonons efficiently as they extend in two dimensions. The most studied systems containing plane defects in the heat transfer field in recent years are the heterostructure superlattices (SLs), which are periodic arrays of alternating materials where one layer in the array consists of  $n$ -atomic layers of material  $A$  and the alternating layer has  $m$ -atomic layers of material  $B$ . For a crystal SL, the thermal conductivity parallel to the layers is typically comparable to the average of the two bulk materials, as long as the interfaces between the layers do not have a large density of defects. While the most interesting measurement is the cross-plane thermal conductivity, which could be one order of magnitude smaller than the values of the corresponding bulk constituents, and in some cases, even smaller than the value of a random alloy with the same components due to the numerous interface scatterings (Volz et al. 2000; Cahill et al. 2014; Hyldgaard and Mahan 1997; Koh et al. 2009; Lee and Venkatasubramanian 2008). Also, in certain SLs, a minimal thermal conductivity exists at a specific period length (Simkin and Mahan 2000).

In this thesis, we will focus on the impact of the line defect of *screw dislocations*, of the plane defects of *anti-phase SLs*, of *twinning SLs* and of *vacuum gaps*, on the thermal transport phenomena by analysing the detailed physical mechanisms involved.

### 1.3 Organization of the Thesis

We begin Chapter 2 with a brief introduction to the methods that will be used for the heat transfer calculations and the corresponding phonon related calculations. These methods include the equilibrium molecular dynamics (EMD) and the nonequilibrium molecular dynamics (NEMD) simulations for thermal conductivity calculations, the phonon Green's function for ballistic thermal conductance calculations, and lattice dynamics for eigenmodes analysis.

In Chapter 3, we start with the investigation of the impact of line defect – screw dislocations on thermal conductivity. We consider  $\langle 110 \rangle$  Si nanowire and nanotube structures containing an axial screw dislocation, simulated by objective molecular dynamics including the classical Tersoff potential. By means of direct nonequilibrium molecular dynamics simulations, we uncover a decrease in thermal conductivity due to the presence of axial screw dislocations with closed and open cores. An analysis based on the atomistic Green function method reveals that this decrease originates in the phonon-phonon scattering due to the anharmonicity introduced especially by the highly distorted core region. As high-strain is intrinsic to dislocations, the effect should occur to various extents in other nano-materials.

From Chapter 4 on, we deal with the problems of how plane defects affect heat

transfer in nanowires. In Chapter 4, a new type of SiC superlattice, i.e. anti-phase superlattice nanowires (APSL NWs) composed of only SiC component but with different stacking sequence is addressed. Our equilibrium molecular dynamics simulations (EMD) show that the thermal conductivity of period modulated APSL NWs can be significantly reduced up to 52% at room temperature compared to the one of pristine NWs. Phonon density of states reveals that new vibrational modes emerge on the interfaces due to the formation of Si-Si and C-C bonds. We identified that the increased phonon interfacial scattering is the predominant factor that hinders the thermal transport along the wires with long period length. Phonon coherent transport is also observed in the structures with short period length, which leads to a minimum thermal conductivity at the period of 6 nm. These results provide clear guidelines to design structures with minimal thermal conductivity and possibly promote SiC as a competitive thermoelectric material.

In Chapter 5, by using Non-equilibrium Molecular Dynamic simulations, the thermal conductivity of a new type of Si nanowires with a twinning superlattice structure has been investigated. We first show that this latter structural modulation can yield a 65% thermal conductivity reduction compared to the one of the straight wire case at room temperature. Secondly, a purely geometry induced minimal thermal conductivity is observed at a specific period depending on diameter. Mode analysis reveals that the minimal thermal conductivity arises due to the disappearance of favored atom polarization directions. The current thermal conductivity reduction mechanism can also collaborate with the other well-known reduction mechanisms, such as the one related to coating, to further reduce the thermal conductivity, which enables the Si twinning superlattice nanowires to be a promising candidate for thermoelectric conversion.

Chapter 6 addresses the heat transfer between two silica clusters with a gap by means of the non-equilibrium Green's function method. Critical gap distances of 4 Å and 3-5 times of the cluster size are found. Beyond 4 Å the thermal conductance decreases as predicted by the charge-charge interaction in the range of 4 Å to 3 times the cluster size and by the dipole-dipole interaction in the range larger than 5 times the cluster size. However, when the distance becomes smaller than 4 Å, it is shown to be the range of a quantum interaction where the electrons of both clusters are shared. This quantum interaction leads to the dramatic increase of the thermal coupling between neighbor clusters due to the strong interactions. This study finally provides a description of the transition between radiation and heat conduction in gaps smaller than a few nanometers.

Finally, we conclude the thesis in Chapter 7.

# Chapter 2

## Methods

### 2.1 Molecular Dynamics

#### 2.1.1 Background

We carry out computer simulations in the hope of understanding the properties of assemblies of molecules in terms of their structure and the microscopic interactions between them. This serves as a complement to conventional experiments, enabling us to learn something new, something that cannot be found out in other ways. Computer simulations act as a bridge between microscopic length and time scales and the macroscopic world of the laboratory. It also act as a bridge in another sense: between theory and experiment ([Allen 2004](#)).

Molecular dynamics simulation consists of the numerical, step-by-step, solution of the classical equations of motion:

$$\frac{d^2\vec{r}_i}{dt^2} = \frac{\vec{F}_i}{m_i} \quad (2.1)$$

where  $t$  refers to the time,  $m_i$  is the mass of atom  $i$ ,  $\vec{r}_i$  is its position vector, and  $\vec{F}_i$  is the total force vector acting on the atom  $i$ . The force applied on any atom is derived from the first derivative of the potential energy  $U$ . For example, in a two body interaction situation,

$$\vec{F}_i = \sum_{j \neq i} \vec{F}_{ij} = - \sum_{i \neq j} \frac{\partial U(r_{ij})}{\partial \vec{r}_{ij}} \quad (2.2)$$

where  $\vec{F}_{ij}$  is the force applied on atom  $i$  by atom  $j$ ,  $\vec{r}_{ij} = \vec{r}_i - \vec{r}_j$  is the distance vector between the two atoms. The potential energy  $U$  is essentially the soul of molecular dynamics. A good potential can provide us with reasonable results comparable with the ones of experiments when the structure is properly set

up. Ideally, a potential energy function must combine simplicity, accuracy, and transferability. It is usually designed according to the fitting from experimental data, or density functional theory calculations. Generally, the total potential energy of a system can be expressed as a sum of terms involving single, pairs, triplets, and so forth, of atoms (Allen and Tildesley 1989):

$$U = \sum_i U_1(r_i) + \sum_i \sum_{j>i} U_2(r_i, r_j) + \sum_i \sum_{j>i} \sum_{k>j>i} U_3(r_i, r_j, r_k) + \dots \quad (2.3)$$

The first term in the potential energy function,  $U_1(r_i)$ , can be used to incorporate the effect of an external field acting on the system. The remaining terms denote the interactions between two atoms, three atoms and so on. The summation index relation  $i$ ,  $j$ , and  $k$  in the second and third terms prevents the inclusion of the interaction potential between a set of atoms more than once.

Molecular dynamics can usually be conducted in several ensembles with the conditions of constant energy ( $E$ ) or temperature ( $T$ ), constant atomic number ( $N$ ) or chemical potential ( $\mu$ ), and constant volume ( $V$ ) or pressure ( $P$ ), depending on the properties that one wants to measure. The most widely adopted statistical sampling ensembles are the microcanonical ensemble ( $NVE$ ), the canonical ensemble ( $NVT$ ) and the isobaric-isothermal ensemble ( $NPT$ ) for solids. However, there is increasing interest in conducting MD simulations which do not fall within the classification of these classical ensembles. According to statistical physics, all the macroscopic properties can be derived from the fluctuation-dissipation theorem. Here we list the formula of several of the most measured quantities in MD simulations.

The total energy of the system,  $E$ , is the sum of the total potential energy  $U$ , and the kinetic energy  $K_e$ :

$$\langle E \rangle = \langle U \rangle + \langle K_e \rangle \quad (2.4)$$

where the brackets  $\langle \rangle$  represent the ensemble average. The potential energy term is expressed in Eq. 2.3. The kinetic energy can be calculated as follows:

$$K_e = \frac{1}{2} \sum_i^N m_i v_i^2 \quad (2.5)$$

$N$  is the total number of atoms in the system.  $m_i$  and  $v_i$  are the mass and velocity of atom  $i$ . The kinetic energy is also tightly related to the temperature ( $T$ ) of the system with the following relation:

$$T = \frac{2\langle K_e \rangle}{3Nk_B} = \frac{\sum_i^N m_i v_i^2}{3Nk_B} \quad (2.6)$$

where  $k_B$  is the Boltzmann constant. This equation is derived from the *Energy equipartition theorem*, which states that, in thermal equilibrium, energy is shared equally among all of its various forms. At temperature  $T$ , the energy for each degree of freedom is  $k_B T/2$ . Without considering the spin motion of atoms, the kinetic energy of each atom can be written as  $E_s = \frac{3}{2}k_B T$  (3 is the degree of freedom of kinetic energy). So the temperature  $T$  can be expressed with Eq 2.6 in a system with atom number  $N$ . The pressure is also one of the frequently measured quantities in MD simulations and it is written as:

$$P = \frac{Nk_B T}{V} + \frac{1}{3V} \left\langle \sum_i^{N-1} \sum_{j>i}^N r_{ij} \cdot F_{ij} \right\rangle \quad (2.7)$$

Here  $V$  is the volume of the system of interest. In heat transfer simulations, one usually needs to calculate the heat flux in different directions in order to further cast the thermal properties like conductivity. The heat flux is defined as (Schelling et al. 2002):

$$\vec{J} = \frac{1}{V} \frac{d}{dt} \sum_i \vec{r}_i(t) E_i(t) \quad (2.8)$$

where  $\vec{r}_i(t)$  is the time-dependent coordinate of atom  $i$  and  $E_i$  is the total energy of atom  $i$ . Taking the pair term of potential energy in Eq. 2.3, one can derive the heat flux in the following form:

$$\begin{aligned} \vec{J} &= \frac{1}{V} \left[ \sum_i E_i \vec{v}_i + \sum_{i<j} (\vec{F}_{ij} \cdot \vec{v}_j) \vec{r}_{ij} \right] \\ &= \frac{1}{V} \left[ \sum_i E_i \vec{v}_i + \frac{1}{2} \sum_{i<j} (\vec{F}_{ij} \cdot (\vec{v}_i + \vec{v}_j)) \vec{r}_{ij} \right] \end{aligned} \quad (2.9)$$

where  $\vec{F}_{ij}$  is the force vector between atom  $i$  and  $j$ . With the obtained heat flux, one can calculate the thermal conductivity of the system of interest according to the Green-Kubo formula in EMD simulations or according to the Fourier's law together with the temperature profile in NEMD simulations. In the heat transfer analysis, one often needs to check the atomic vibrational density of states (VDOS), which measures the number of vibrations within a given frequency range. The VDOS can be numerically computed by decomposing the time correlation function of the atomic velocities into the Fourier space as:

$$\begin{aligned} VDOS(\omega) &= \frac{1}{k_B T} \sum_i m_i |v_i(\omega)|^2 \\ |v_i(\omega)|^2 &= \int_0^\infty \langle v_i(0)v_i(t) \rangle dt \end{aligned} \quad (2.10)$$

the sum index  $i$  is over all atoms and  $m_i$  is the atom mass of the  $i^{\text{th}}$  atom. By dumping the velocity trajectories of different regions, one can calculate the local VDOS, which is useful when the material is not homogeneous. By selecting different atom types, the relative contribution of VDOS from different atom types can be identified easily.

### 2.1.2 Thermal Conductivity from Equilibrium Molecular Dynamics Simulation

In equilibrium molecular dynamics simulations, we use the fluctuation-dissipation theorem from linear response theory to provide the connection between the energy dissipation in irreversible processes and the thermal fluctuations in equilibrium (Kubo et al. 1985). The net flow of heat in a solid, given by the heat current vector  $\mathbf{J}$ , fluctuates around zero at equilibrium. In the Green-Kubo (GK) method, the thermal conductivity is related to how long it takes to these fluctuations to relax to equilibrium. In the case of an isotropic material, the conductivity is defined by (Kubo et al. 1985)

$$\kappa = \frac{1}{k_B V T^2} \int_0^\infty \langle J_x(t) J_x(0) \rangle dt = \frac{1}{3k_B V T^2} \int_0^\infty \langle \vec{J}(t) \cdot \vec{J}(0) \rangle dt \quad (2.11)$$

where  $V$  represents the volume of the simulation cell,  $t$  is the time,  $J_x(t)J_x(0)$  and  $\vec{J}(t) \cdot \vec{J}(0)$  are the heat current autocorrelation functions (HCACF) in the  $x$  direction and all directions, respectively. In crystals where the fluctuations have long life times (i.e., the mean free path of phonons is large), the HCACF decays slowly. The thermal conductivity is related to the integral of the HCACF, and is accordingly large. In materials such as amorphous solids, where the mean free path of phonons is small, thermal fluctuations are quickly damped, leading to a small integral of the HCACF and a low thermal conductivity (McGaughey and Kaviany 2004).

In real computational procedures, instead of integrating up to infinity in Eq. 2.11, the upper limit is a finite but long enough time period that captures the correct statistics. The continuous integral is also replaced by a discrete summation. To remove the arbitrariness on the choice of the upper limit, different methods have been proposed in the literatures (Volz et al. 1996; Che et al. 2000; McGaughey and Kaviany 2004; Li et al. 1998). According to the Cattaneo-Vernotte's relation (Vernotte 1958; Cattaneo 1958), Volz et al derived the time autocorrelation function of the heat flux as (Volz et al. 1996)

$$\langle \vec{J}(t) \cdot \vec{J}(0) \rangle = \langle \vec{J}(0) \cdot \vec{J}(0) \rangle \exp(-t/\tau) \quad (2.12)$$

A similar exponential function was used by Li et al to fit the heat flux auto-

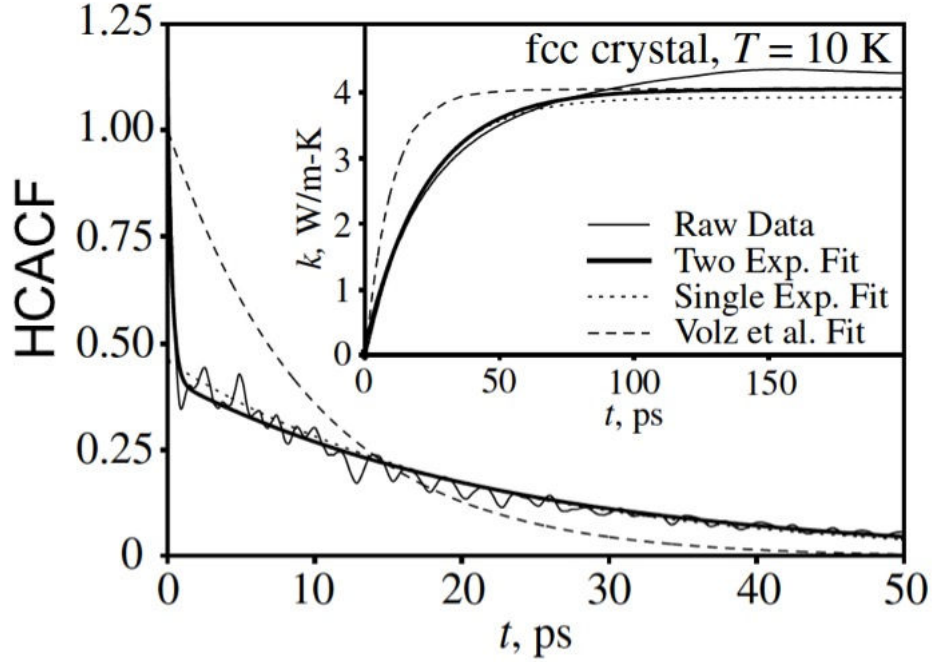


**Figure 2.1:** An example of heat flux autocorrelation function with the fitting of different methods. The insert represents the integral of the thermal conductivities over time. Figure from McGaughey, A. and M. Kaviany (2004), *International Journal of Heat and Mass Transfer* 47: 1783

correlation function

$$\frac{\langle \vec{J}(t) \cdot \vec{J}(0) \rangle}{3} = g \exp(-t/\tau) \quad (2.13)$$

However, in Li's approach, the single exponential function is not used to fit the whole HCACF curve but only the range  $[t_1, t_2]$ . This approach is used to determine the tail contribution of HCACF. Instead of using a single exponential function to fit the HCACF in the full time interval, Che et al (Che et al. 2000) proposed a double exponential function to fit the whole HCACF curve. This approach has also been used by McGaughey et al (McGaughey and Kaviany 2004) for solid Ar but with different explanations. The fitting function reads as

$$\frac{\langle \vec{J}(t) \cdot \vec{J}(0) \rangle}{3} = A_{sh} \exp(-t/\tau_{sh}) + A_{lg} \exp(-t/\tau_{lg}) \quad (2.14)$$

where the subscripts *sh*, and *lg* refer to short range and long range, respectively. Fig. 2.1 shows an example of HCACF obtained from solid Ar at 10 K and the corresponding fitting curves with Eq.2.12, 2.13 and 2.14.

### 2.1.3 Thermal Conductivity from Non-equilibrium Molecular Dynamics Simulation

Non-equilibrium molecular dynamics, also known as the direct method, extracts the thermal conductivity from the Fourier's law. In this method, one needs to impose a one-dimensional temperature gradient on a simulation cell by allowing thermal power exchange between the heat source and sink and measure the resulting heat flux. The thermal conductivity is then obtained as the ratio of the heat flux and the temperature gradient. An alternative, but equivalent way consists in inducing a heat flux and to measure the resulting temperature gradient. In both cases the system is first allowed to reach a steady state, after which long simulations are conducted allowing to obtain correct statistical measurements. The NEMD method is often the method of choice for studies of nanomaterials while for bulk thermal conductivity, particularly high-conductivity materials, the equilibrium method is typically preferred due to less severe size effects (Termentzidis and Merabia 2012).

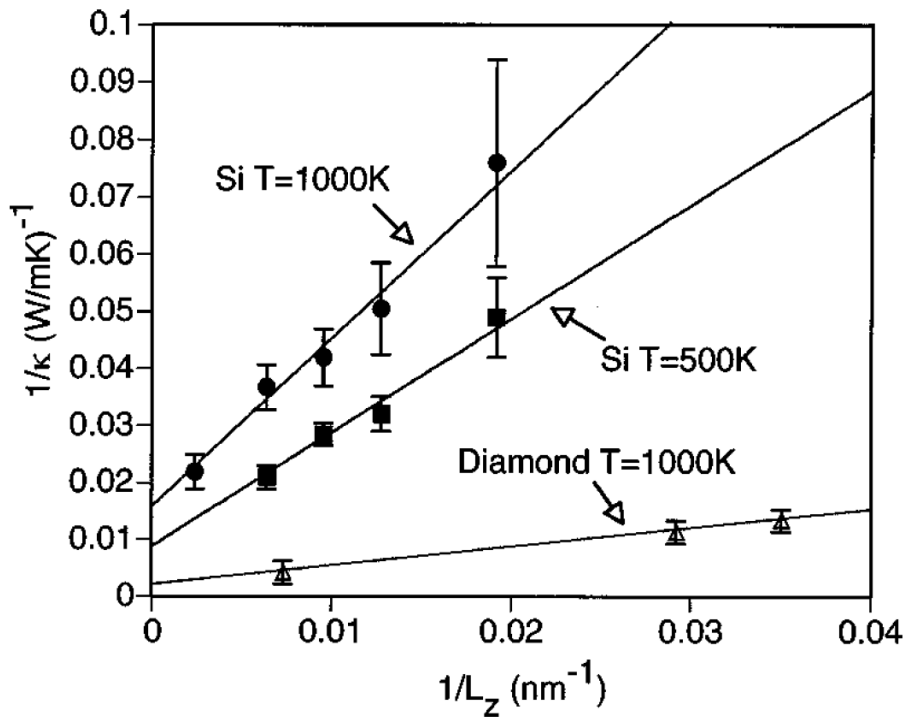


**Figure 2.2:** The inverse of the thermal conductivities measured with NEMD simulations for Si and diamond at specified temperatures versus  $1/L$  and the corresponding fitting with Eq. 2.16.  $\kappa_\infty$  is get at  $1/L = 0$ . Figure from Schelling et al (2002), *Phys. Rev. B* 65: 144306

In NEMD simulations, finite-size effects arise when the length of the simulation

cell  $L$  is not significantly longer than the phonon mean free path. This is understood to be a result of scattering that occurs at the interfaces with the heat source and sink. As a result, the phonon mean free path is limited by the system size. To eliminate the size effect, Schelling et al (Schelling et al. 2002) proposed a method based on the Matthiessen's rule to determine the effective mean free path  $\Lambda_{eff}$  when  $L \sim \Lambda_\infty$ , where  $\Lambda_\infty$  is the mean free path for an infinite system. The effective mean free path is obtained by the following relation:

$$\frac{1}{\Lambda_{eff}} = \frac{1}{\Lambda_\infty} + \frac{4}{L} \quad (2.15)$$

Here, the factor of 4 accounts for the fact that as phonons travel along the length of the simulation cell from the source to the sink, its average distance since the last scattering event should be  $L/4$ . In kinetic theory, the thermal conductivity is given as  $\kappa = \frac{1}{3}C_v v \Lambda$ , where  $C_v$  and  $v$  are the specific heat and the phonon group velocity. Combing with Eq. 2.15, the effective thermal conductivity is obtained:

$$\frac{1}{\kappa_{eff}} = \frac{1}{\kappa_\infty} + \frac{12}{C_v v} \frac{1}{L} \quad (2.16)$$

Eq. 2.16 suggests that a plot of  $1/\kappa$  vs  $1/L$  should be linear, and that the thermal conductivity of an infinite system can be obtained by extrapolating to  $1/L = 0$ . Fig. 2.2 shows the examples of using Eq. 2.16 to extract the thermal conductivity with infinite sizes for Si and diamond. Good linear fits are found in these cases imply the successful application of Eq. 2.16.

#### 2.1.4 Challenges of Molecular Dynamic Simulations

Molecular Dynamics has been widely used to predict various properties in bulk and nanomaterials. It has been regarded as a successful tool to assist the experimental designs and understand the mechanisms at the atomic scales. Despite its successful applications, it also suffers from several important and fundamental challenges.

The first challenge comes from the simulation size and time. Nowadays, with the assistance of supercomputing, the usual MD simulations contain hundreds to millions of atoms, corresponding to a cubic box with the side length less than 50 nm. However, in some of the simulations, the simulation box could exceed hundreds of nanometers. For example, if one needs to study the grain boundary properties, at least tens of grains should be contained in a simulation box and each grain could have a size of 50 nm in diameter. The simulation time normally ranges from several picoseconds to hundreds of nanoseconds, which

is far from enough in some cases. Examples can be listed from the studies of phase transitions. Most of the phase transitions takes place from milliseconds to minutes or even hours in bulk state, which is far beyond the timescales that can be achieved to date. The challenges from the simulation size and time are important but not fundamental and can be solved with the development of future supercomputing. The most fundamental challenges is that the simulation is classical, that is , the trajectories of the atoms are integrated according to the classical Newtonian mechanics without considering quantum effect. This is usually justified by stating that for most of the elements at room temperature, the atomic mass is sufficiently large in order the de Broglie wavelength to be considerably smaller than the interatomic distance and atoms can be treated classically. Nevertheless, due to the classical assumptions, phonons follow the Boltzmann distributions, i.e.,  $f = Ae^{E_i/k_B T}$  instead of the Bose-Einstein distributions, and as a result, energy equipartition principle applies. This means that at any temperature  $T$ , all phonon modes are fully populated and each phonon mode has the energy  $k_B T$ . This is valid at high temperatures ( $T \gg T_D$ ,  $T_D$  is the Debye temperature), at which the Bose-Einstein distribution can be simplified to the Boltzmann distribution. At the temperatures below the Debye temperature, the high-frequency modes will be at least partially unoccupied in contrast with MD simulations. Consequently, MD simulations are usually conducted above the Debye temperature (or approximately above  $T_D/2$ ). To overcome this fundamental shortcoming, different quantum corrections in MD simulations have been tried including a temperature correction (Wang et al. 1990) and a quantum thermal bath (Dammak et al. 2009). Besides, the size scaling in non-equilibrium MD calculations of thermal conductivity is far from been solved, especially in low dimensional systems (Yang et al. 2010).

## 2.2 Phonon Green's Function

The Green's function method has been developed originally for the calculation of electron transport (Keldysh 1965) and it was developed after to describe the phonon transport by Mingo et al (Mingo and Yang 2003; Zhang et al. 2006). It is a powerful method in dealing with ballistic transport phenomena.

### 2.2.1 General Formulation

In a harmonic system, the matrix form of the system Hamiltonian in Eq. 1.8 can be written as

$$H = \frac{M}{2} \dot{u}^\dagger \dot{u} + \frac{1}{2} u^\dagger \bar{K} u \quad (2.17)$$

Where  $M$  and  $\bar{K}$  are the mass matrix and force constant matrix. The dynamics

of a system is governed by the Hamilton-Jacobi equation, which reads as

$$\frac{dP}{dt} = -\frac{dH}{du} \quad (2.18)$$

substituting the matrix form of the system Hamiltonian into the Hamilton-Jacobi equation and considering the plane wave solution of the displacement, i.e.,  $u = A_0 e^{i(\mathbf{q}\mathbf{R} - \omega t)}$ , we obtain the equation of motion as

$$(\omega^2 I - K)u = 0 \quad (2.19)$$

Hence, the motion of atoms is completely determined by its mass normalized force constant matrix  $K$ , with matrix elements related to the second derivative of potential energy  $U$ , i.e.,

$$K_{ij} = \frac{1}{\sqrt{M_i M_j}} \bar{K} = \frac{1}{\sqrt{M_i M_j}} \frac{\partial^2 U}{\partial u_i \partial u_j} \quad (2.20)$$

where the subscript  $i$  or  $j$  represents the  $i^{\text{th}}$  or  $j^{\text{th}}$  degree of freedom. So the resolvent Green's function of the system is defined as

$$G(\omega) = \frac{1}{(\omega + i\Delta)^2 I - K} \quad (2.21)$$

where  $\Delta \rightarrow 0^+$  is an infinitesimal imaginary part that maintains the causality of the Green's function,  $I$  is a identity matrix.

Considering a system composed by three parts, the left and right leads and the central scattering region denoted with symbols  $L$ ,  $R$  and  $C$ , respectively (Fig. 2.3). To obtain the Green's function of the central scattering region, we rewrite the force constant matrix  $K$  in the following form

$$K = \begin{bmatrix} K^L & V^{LC} & 0 \\ V^{CL} & K^C & V^{CR} \\ 0 & V^{RC} & K^R \end{bmatrix} \quad (2.22)$$

With  $K^\alpha$  and  $V^\beta$  being the force constant matrices of different regions and coupling force constant matrices between different regions, respectively, as defined in Fig. 2.3. Correspondingly, we can write the system Green's function in terms of the three regions as

$$G = \begin{bmatrix} G^L & G^{LC} & G^{LR} \\ G^{CL} & G^C & G^{CR} \\ G^{RL} & G^{RC} & G^R \end{bmatrix} \quad (2.23)$$

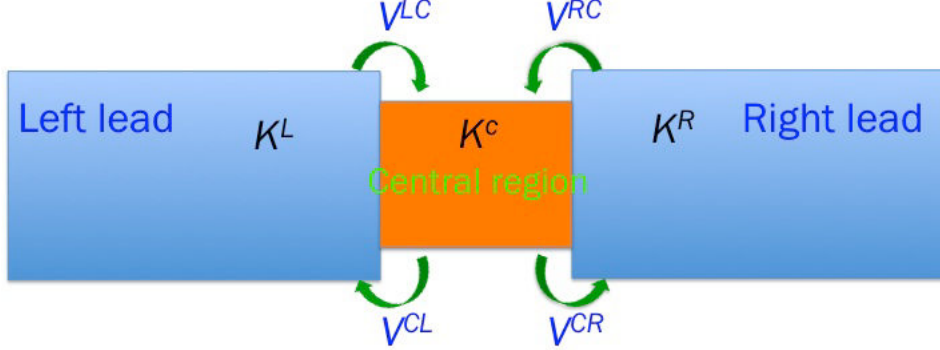


**Figure 2.3:** Schematic for the Green's function calculation with the left and right leads and the central scattering region. The force constant matrices for the three regions are denoted as  $K^L$ ,  $K^R$  and  $K^C$ , respectively. The coupling matrices between the left lead and the central region, the right lead and the central region are denoted as  $V^{LC}$  and  $V^{RC}$ , respectively

So Eq. 2.21 can be rewritten as follows in terms of Eqs. 2.22 and 2.23

$$\begin{bmatrix} (\omega + i\Delta)^2 I - K^L & -V^{LC} & 0 \\ -V^{CL} & (\omega + i\Delta)^2 I - K^C & -V^{CR} \\ 0 & -V^{RC} & (\omega + i\Delta)^2 I - K^R \end{bmatrix} \times \begin{bmatrix} G^L & G^{LC} & G^{LR} \\ G^{CL} & G^C & G^{CR} \\ G^{RL} & G^{RC} & G^R \end{bmatrix} = \begin{bmatrix} I & 0 & 0 \\ 0 & I & 0 \\ 0 & 0 & I \end{bmatrix} \quad (2.24)$$

From the above equation, the following three equations can be easily casted,

$$\begin{aligned} [(\omega + i\Delta)^2 I - K^L] G^{LC} - V^{LC} G^C &= 0 \\ V^{CL} G^{LC} + [(\omega + i\Delta)^2 I - K^C] G^C - V^{CR} G^{RC} &= I \\ -V^{RC} G^C + [(\omega + i\Delta)^2 I - K^R] G^{RC} &= 0 \end{aligned} \quad (2.25)$$

Now we define the surface Green's functions of the left and right leads as

$$g^\alpha = \frac{1}{(\omega + i\Delta)^2 I - K^\alpha} \quad (2.26)$$

with  $\alpha = L, R$ . The retarded Green's function of the central scattering region  $G_s^r$  can be derived with the combination of Eq. 2.25 and 2.26 as

$$G_s^r = G^C = \frac{1}{(\omega + i\Delta)^2 I - K^C - \Sigma_L - \Sigma_R} \quad (2.27)$$

where  $\Sigma_L$  and  $\Sigma_R$  are the self energies of the left and right leads and they are linked with the surface Green's functions as follows

$$\begin{aligned}\Sigma_L &= V^{CL}g^LV^{LC} \\ \Sigma_R &= V^{CR}g^RV^{RC}\end{aligned}\tag{2.28}$$

Here,  $V^{L(R)C}$  is the complex conjugate of  $V^{CL(R)}$ , i.e.,  $V^{L(R)C} = (V^{CL(R)})^\dagger$ . Once the Green's function of the central scattering region is obtained, the phonon transmission function  $Tr$  from the left side to the right side by crossing the central region can be derived in terms of the Landauer formula and it is expressed as

$$Tr(\omega) = \text{Trace}(G_s^r \Gamma_L G_s^a \Gamma_R)\tag{2.29}$$

where  $G_s^a = (G_s^r)^\dagger$  represents the advanced Green's function of the central region,  $\Gamma_{L/R}$  is the broadening function of the left or right lead and it is written as

$$\begin{aligned}\Gamma_L &= i(\Sigma_L - \Sigma_L^\dagger) \\ \Gamma_R &= i(\Sigma_R - \Sigma_R^\dagger)\end{aligned}\tag{2.30}$$

Assuming that the temperature difference between the two reservoirs is finite, the thermal conductance from the left to the right reservoir can be written as the integral of the transmission function over all frequencies

$$\sigma = \int_0^{\omega_{max}} Tr(\omega) \frac{\partial}{\partial T} \left( \frac{1}{e^{\hbar\omega/k_B T} - 1} \right) \hbar\omega \frac{d\omega}{2\pi}\tag{2.31}$$

where  $\omega_{max}$  is the Debye frequency. From Eq. 2.27 - 2.29 we know that in order to calculate the thermal conductance, the main task is to get the surface Green's functions.

### 2.2.2 Recursive method for surface Green's function calculation

The surface Green's functions can be computed rather quickly by recursive iterations (Sancho et al. 1985). Recursive methods for the evaluation of the Green's function are based on the division of the device in smaller sections, where the Green's functions can be calculated easily. These sections are then "glued together" by using the so-called Dyson's equation (Volz 2009).

$$G = g + gVG\tag{2.32}$$

which allows to relate the Green's function  $g$  of two disconnected subsystems to the Green's function  $G$  of the connected system, where  $V$  describes the connecting force constant matrix.

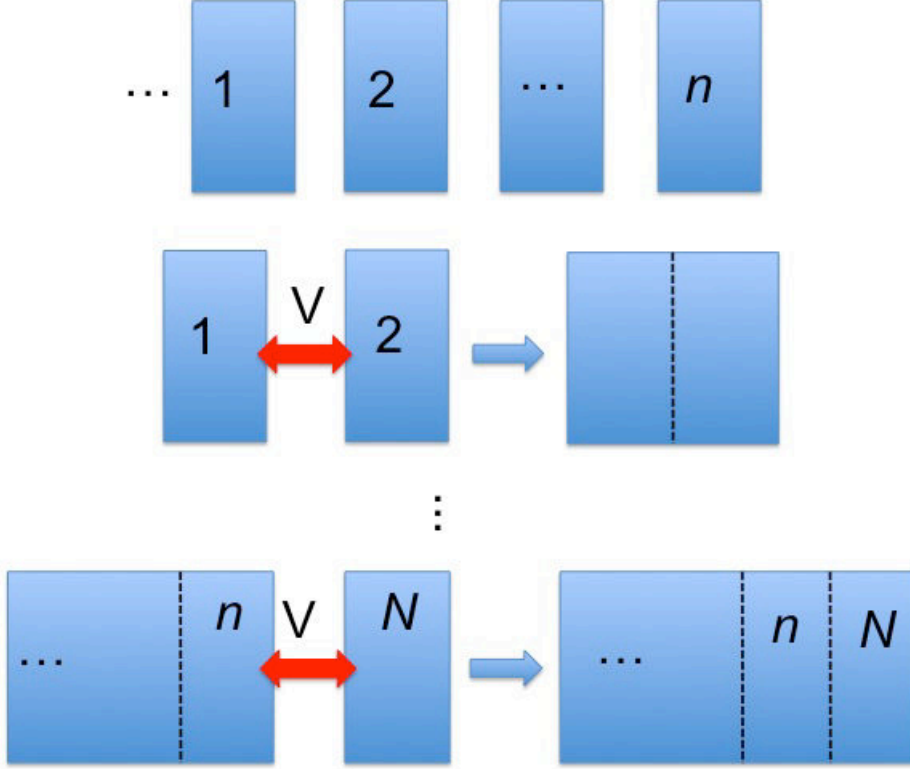


**Figure 2.4:** Schematics for the surface Green's function calculation by gluing each sections together. All the blocks are firstly isolated (top). After the second block is glued on the first block (middle) and the Green's function of each section can be calculated. By repeating the process, the  $N^{\text{th}}$  section can be attached on the  $n^{\text{th}}$  section and forming a chain with  $N$  blocks (bottom). The Green's functions of each blocks can be evaluated consequently.

Fig. 2.4 illustrates how these sections are glued together. We consider that all the sections are identical and only interact with their two neighbours. The force constant matrix of the whole system is

$$K = \begin{bmatrix} K_{00} & V & 0 & \dots \\ V^\dagger & K_{11} & V & 0 \\ 0 & V^\dagger & K_{11} & V \\ \dots & 0 & V^\dagger & \ddots \end{bmatrix} \quad (2.33)$$

The block  $K_{00}$  is the section immediately adjacent to the center region. At the beginning, all of the sections are isolated, so their Green's function can be

obtained according to the definition of Eq. 2.21. Then the first two sections can be glued together with the Dyson's equation and we can get the surface Green's function of both sections 1 and 2. Afterwards we glue the third, the fourth, ..., the  $N^{\text{th}}$  sections together, and can obtain the surface Green's functions of the first and  $N^{\text{th}}$  sections. For example, when the  $N^{\text{th}}$  section is coupled to the previous block, according to the Dyson's equation, we have

$$\begin{aligned} G_{NN} &= g_{NN} + g_{NN}V_{Nn}G_{nN} \\ G_{nN} &= g_{nn}V_{nN}G_{NN} \end{aligned} \quad (2.34)$$

where  $G_{NN}$  and  $G_{nN}$  are the coupled Green's function of the  $N^{\text{th}}$  section and the coupled Green's function between the  $n^{\text{th}}$  and  $N^{\text{th}}$  sections, respectively.  $g_{NN}$  is the decoupled Green's function of the  $N^{\text{th}}$  section.  $V_{nN} = V_{Nn}^\dagger = V$  is the coupling matrix between two neighbour sections as illustrated in Fig. 2.4. As a result, the surface Green's function of the  $N^{\text{th}}$  section can be obtained

$$G_{NN} = [I - g_{NN}V_{Nn}g_{nn}V_{nN}]^{-1} g_{NN} \quad (2.35)$$

The other useful Green's function such as  $G_{11}$  and  $G_{1N}$  can be derived similarly using the Dyson's equation .

The Green's functions allow one to treat semi-infinite, non-periodic systems. Thus, no spurious periodicities need to be imposed. The conductance calculation is based on the quantum Bose-Einstein distributions, so in such a way that the quantum effect is included. Generally, the atomistic Green's function is quite useful when the size of a system is comparable or shorter than the bulk mean free path, phonons travel nearly ballistically, and anharmonic effects are less important. The harmonic approximations simplifies the problem enormously, since it reduces to the question of non-interacting phonons. In a purely harmonic case, Green's functions have advantages over a molecular dynamics simulation at low temperatures where quantum effect is important. The anharmonic Green's function has also been developed in the literature (Mingo 2006; Wang et al. 2006). However, due to the dramatic increase of the computational time, it is limited to small systems such as molecular junctions.

Molecular dynamics represents an alternative to Green's function techniques. In summary, the two most fundamental differences between the two, physically speaking, are (Volz 2009):

- Green's function is quantum mechanical whereas MD is classical and thus restricted to high temperatures.
- MD includes anharmonic interactions to all orders, whereas Green's function is presently limited to length scales at which anharmonicity is of secondary

importance.

Therefore, despite their radically different formulations, the two techniques can complement one another, each of them working best in the cases where the other one might fail. It is thus important to carry out studies to compare the outcomes from both types of calculation.

## 2.3 Lattice Dynamics

### 2.3.1 Phonon Dispersion Relation

In the previous section, we derived the equation of motion of a system and it is expressed in Eq. 2.19. In principle, for a non-zero dimensional system,  $K$  and  $u$  are infinite and Eq. 2.19 is unsolvable. However, for a periodic system, the problem can be largely simplified. In a periodic system, the potential is also periodic, as a result, the wave function (atomic displacement here) has the Bloch wave form. The displacement vectors in different unit cells only differ with a phase factor of  $\mathbf{q}\mathbf{R}$ . That is the reason why a factor of  $e^{i\mathbf{q}\mathbf{R}}$  in the plane wave solution of  $u$  appears. Let  $u_0 = A_0 e^{-i\omega t}$  with  $A_0$  being a vector with  $3N$  components ( $N$  is the number of atoms within one unit cell),  $u$  is then written as the Bloch form as

$$u = u_0 e^{i\mathbf{q}\mathbf{R}} \quad (2.36)$$

Eq. 2.19 can be written as the following form when Eq. 2.36 is substituted

$$\omega^2 \begin{pmatrix} u_0 e^{i\mathbf{q}\mathbf{R}_1} \\ u_0 e^{i\mathbf{q}\mathbf{R}_2} \\ \vdots \\ u_0 e^{i\mathbf{q}\mathbf{R}_n} \\ \vdots \end{pmatrix} = \begin{pmatrix} k_{11} & k_{12} & \cdots & \\ k_{21} & k_{22} & \cdots & \\ & \vdots & & \\ & \cdots & k_{nm} & \cdots \\ & \vdots & & \end{pmatrix} \begin{pmatrix} u_0 e^{i\mathbf{q}\mathbf{R}_1} \\ u_0 e^{i\mathbf{q}\mathbf{R}_2} \\ \vdots \\ u_0 e^{i\mathbf{q}\mathbf{R}_n} \\ \vdots \end{pmatrix} \quad (2.37)$$

Here  $k_{nm}$  is a  $3N \times 3N$  matrix. The equivalence of each matrix element in the above equation yields

$$\omega^2 u_0 = \sum_m k_{nm} e^{i\mathbf{q}\mathbf{R}_{nm}} u_0 \quad (2.38)$$

where  $\mathbf{R}_{nm} = \mathbf{R}_m - \mathbf{R}_n$  is the unit cell vector difference between the unit cell  $m$  and  $n$ . Let

$$D(q) = \sum_m k_{nm} e^{i\mathbf{q}\mathbf{R}_{nm}} \quad (2.39)$$

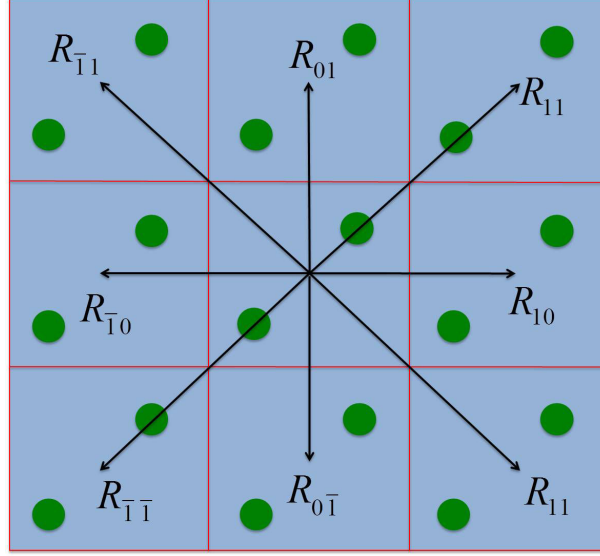


**Figure 2.5:** An example of the dynamic force constant summation (Eq. 2.39) in a two dimensional lattice. Due to the cut off of potential energy, only the near neighbour cells have non-zero elements in the real space force constant matrices. As a result, the summation is restricted to the near interact neighbour cells.

which is called the dynamical matrix. From the summation, we know that the dynamical matrix is just the Fourier transform of the real space force constant matrices into the reciprocal space ( $q$  space). It can be proved that  $D(q)$  is Hermitian for real valued wave numbers  $q$ . So Eq. 2.38 can be rewritten as

$$\omega^2 u_0 = D(q)u_0 \quad (2.40)$$

which is the dynamical equation in one unit cell of a periodic system (application form of Eq. 2.19). In principle, the discrete Fourier transform of the force constant matrices in Eq. 2.39 has infinite terms. However, due to the cut off of potential energy, it can always be restricted to a limited number of neighbours. For most of the empirical potentials, the interactions are limited to the nearest or second nearest neighbours. Consequently, the summation can be performed to the nearest or second nearest neighbours. Fig. 2.5 illustrates an example of the force constant summation of a two dimensional lattice. Once the dynamical matrix is obtained, the general eigenvalue problem in Eq. 2.40 can be solved numerically. The eigenfrequency-eigenvector pairs  $\omega - u_0$  can be obtained at each  $q$  point. This  $\omega - u_0$  pair is called the normal mode in a phonon analysis. The relation between  $q$  and frequency is called *phonon dispersion relation*, which is of vital importance in heat transfer calculations.

### 2.3.2 Phonon Group Velocity

The empirical models for calculating the thermal conductivities, e.g., the Boltzmann and Callaway-Holland model, take the group velocity as one of the basic input parameters. The predicted results by these models largely depend on the input group velocities. Also, group velocity is often used for qualitative analysis in heat transfer. So it is useful to derive the phonon group velocity at each frequency and wave vector. From Eq. 2.40,  $\omega$  is an implicit function of  $q$  which makes the explicit evaluation of the group velocity  $v_g$  seemingly difficult. However, an analytical expression for  $v_g$  can be derived by using a perturbation method (Zhao and Freund 2005). Here we take the group velocity in the x direction  $v_x$  for example. According to the definition of the group velocity,  $v_x$  is written as

$$v_x = \left. \frac{\partial \omega}{\partial q_x} \right|_{q_{y,z}} \quad (2.41)$$

Assuming that there are only the nearest neighbour interactions (long range interaction cases can be treated in a similar way), which is valid for most empirical potentials, the dynamical force constant in Eq. 2.39 can be divided into three parts as

$$D(q) = D_L e^{-iq_x L} + D_C + D_R e^{iq_x L} \quad (2.42)$$

where  $L$  is the distance between neighbouring cells (which is the lattice constant for a simple cubic lattice and half of the lattice constant for a FCC or a BCC lattice).  $D_L$ ,  $D_C$  and  $D_R$  are independent of  $q_x$  and represent lattice site interactions with atoms in neighbouring unit cells of the left, coincident, and of the right, respectively. For example, in the schematic presented in Fig. 2.5,  $D_L$ ,  $D_C$  and  $D_R$  can be expressed as

$$\begin{aligned} D_L &= K_{\bar{1}1} + K_{\bar{1}0} + K_{\bar{1}\bar{1}} \\ D_C &= K_{01} + K_{00} + K_{0\bar{1}} \\ D_R &= K_{11} + K_{10} + K_{1\bar{1}} \end{aligned} \quad (2.43)$$

Where  $K_{ij}$  represents the force constant matrix between the central unit cell (index 00) and its neighbouring cell with index  $ij$ . The notation  $\bar{i}$  means the opposite direction of  $i$ . If there is no phonon branch degeneracy, both  $\omega$  and  $u_0$  for a specific phonon branch are continuous functions of  $q_x$ . When a small perturbation  $\delta q_x$  is added to  $q_x$  in Eq. 2.40, the following differential relation can be derived (Zhao and Freund 2005)

$$\delta D(q)u_0 + D(q)\delta u_0 = 2\omega\delta\omega u_0 + \omega^2\delta u_0 \quad (2.44)$$

where

$$\delta D(q) = \delta q_x [-iLe^{-iq_x L} D_L + iLe^{iq_x L} D_R] \quad (2.45)$$

Taking the inner product of Eq. 2.44 with  $u_0$  and combining it with Eq. 2.40, a new relation is yielded

$$u_0^\dagger \delta D(q) u_0 = 2\omega \delta\omega |u_0|^2 \quad (2.46)$$

Note that the matrices  $D_L$  and  $D_R$  are complex conjugates of each other, therefore, the x component of the phonon group velocity has the simple expression

$$v_x = \frac{\partial\omega}{\partial q_x} = \frac{\delta\omega}{\delta q_x} = -\frac{\text{Im}[L\lambda u_0^\dagger D_R u_0]}{\omega |u_0|^2} \quad (2.47)$$

where

$$\lambda = e^{iq_x L} \quad (2.48)$$

So when the  $\omega - u_0$  pairs are obtained by solving Eq. 2.40, the group velocity can be evaluated analytically from Eq. 2.47. The group velocities in the other directions can be calculated in a similar way.

### 2.3.3 Vibrational Mode Analysis

The vibrational properties of a lattice can help us to understand the heat transfer behaviours. Except the VDOS extracted from MD simulations as shown in section 2.1.1, some other vibrational properties, such as mode localization and phase quotient, can be evaluated directly from lattice dynamics Eq. 2.40.

The VDOS or local VDOS provide information averaged over all vibrational modes existing in the structure. By contrast, the participation ratio  $p_\lambda$ , defined for each mode  $\lambda$  as (Schelling and Phillpot 2001; Bodapati et al. 2006)

$$p_\lambda^{-1} = N \sum_{i=1}^N \left( \sum_{\alpha} u_{i\alpha,\lambda}^* u_{i\alpha,\lambda} \right)^2 \quad (2.49)$$

where  $u_{i\alpha,\lambda}$  is the element component of the vibrational eigenvector  $u_0$  in Eq. 2.40,  $\alpha$  and  $i$  correspond to the Cartesian component (x, y or z) and the atom index. The participation ratio characterizes each mode individually and serves as a useful discriminant of spatial localization. The participation ratio measures the fraction of atoms participating in a mode and hence varies between  $O(1)$

(order 1) for delocalized states and  $O(1/N)$  for localized states and effectively indicates the fraction of atoms participating in a given mode. Like the local VDOS, we can define a parameter to characterize the relative contributions of individual modes from different regions in a non-homogeneous structure. This parameter is called the mode weight factor, which is defined as follows in the region  $J$

$$f_{J,\lambda} = \sum_j \sum_{\alpha} (u_{i\alpha,\lambda})^2 \quad (2.50)$$

where the summation over  $j$  is restricted to the atom indexes in the region  $J$ . The mode weight factors in all regions of the system are complementary to each other, i.e., the sum of  $f_{J,\lambda}$  over all regions equals to 1. The mode weight factor can be used to analysis the vibrational properties in different regions. For some purposes in a phonon analyse, sometimes we need to know the vibrational direction of each atom for a specific mode. This can be elucidated by examining the Cartesian components of the unitary polarization vectors  $e_{i\alpha,\lambda}$ , of an atom  $i$ , for a given mode  $\lambda$ , defined as (Allen et al. 1999)

$$e_{i\alpha,\lambda} = \frac{u_{i\alpha,\lambda}}{\sum_{\alpha} u_{i\alpha,\lambda}^* u_{i\alpha,\lambda}} \quad (2.51)$$

In a crystal without defects, the normal modes are all phonon modes and possess well-defined polarization vectors. For example, for a LA mode, if the polarization vector is parallel to  $q$  (say, the z direction), then each atom has a unitary polarization vector component of  $\pm 1$  in the z direction and 0 in the x and y directions. However, in amorphous structures, the atomic displacements are usually uncorrelated and  $e_{i\alpha,\lambda}$  fill in a sphere more or less uniformly (Bodapati et al. 2006). The phase quotient  $\Phi_{\lambda}$ , of a mode  $\lambda$ , which is a discriminant of the acoustic versus the optical nature of the mode, is defined as (Allen et al. 1999)

$$\Phi_{\lambda} = \frac{\sum_{\langle i,j \rangle} \left( \sum_{\alpha} u_{i\alpha,\lambda} u_{j\alpha,\lambda} \right)}{\sum_{\langle i,j \rangle} \left| \sum_{\alpha} u_{i\alpha,\lambda} u_{j\alpha,\lambda} \right|} \quad (2.52)$$

where  $i$  and  $j$  are the nearest neighbours. A value of  $\Phi_{\lambda} \rightarrow 1$  indicates that the nearest-neighbour atoms vibrate mostly in-phase like an acoustic mode while values near -1 indicate that they vibrate out of phase in a manner characteristic of an optical mode.

## 2.4 Conclusions

The most commonly used methods for thermal conductivity calculations in molecular dynamics simulations - EMD and NEMD methods-, have been firstly reviewed and formulated briefly in this chapter. The EMD method is based on the fluctuation and dissipation of the heat flux computed in a system that freely evolves with given interaction potentials and boundary conditions. The Green-Kubo formula is used for thermal conductivity calculations. While the NEMD method consists in applying a temperature gradient, and measuring the corresponding heat flux or vice versa. Thermal conductivity is then extracted with the Fourier's law. MD simulations have proven to be fairly robust in predicting thermal properties of dielectric materials. The main limitation is that the simulation is classic, which limits the simulations to the high temperature ranges ( $T > \Theta/2$ ), where quantum effects can be neglected.

The phonon Green's function, which is an alternative to MD simulations in heat transfer calculations, has also been introduced. The formulation of the Green's function is based on quantum mechanics, so quantum effect is basically included. However, due to the computational complexity, the Green's function is usually limited to the harmonic systems. Generally, the atomistic Green's function is quite useful when the size of a system is comparable or shorter than the bulk mean free path, phonons travel nearly ballistically, and anharmonic effects are less important. Since MD includes anharmonic interactions to all orders but limited to high temperatures, whereas the Green's function is presently limited to length scales and low temperatures at which anharmonicity is of secondary importance. Therefore, despite their radically different formulations, the two techniques can complement themselves, each of them working best in the cases where the other one might fail.

To analyse the phonon properties, we finally introduced the lattice dynamics method in this chapter. The phonon dispersion curve, phonon group velocity can be easily obtained from lattice dynamics. Based on the calculated phonon eigenvectors, the phonon participation ratio, mode weight factor, phonon polarization and phase quotient are evaluated. These parameters are quite useful to help better understand heat transport behaviours in different systems.

In the following chapters, we will use the introduced methods to calculate the thermal conductivities/conductances in various defect systems and also to investigate the corresponding mechanisms.



## Chapter 3

# Strain Defects in Nanowires: Thermally-Active Screw Dislocations in Si Nanowires and Nanotubes

In this chapter, we try to understand the effect of line defects on the thermal conductivity of nanowires. We choose screw dislocations as our study defects since it has been commonly found in nanowires and nanotubes. New properties appear when nanomaterials contain dislocations. Understandings whether these features, which arise naturally during growth, are beneficial or problematic becomes essential for developing applications. Here we investigate  $\langle 110 \rangle$  Si nanowire and nanotube structures containing an axial screw dislocation, as described by objective molecular dynamics coupled with the classical Tersoff potential. By means of direct nonequilibrium molecular dynamics simulations, we uncover a decrease in thermal conductivity in the presence of axial screw dislocations with closed and open cores. Analysis based on the atomistic Green function method reveals that this decrease originates in the phonon-phonon scattering due to the anharmonicity introduced especially by the highly distorted core region. As high-strain is intrinsic to dislocations, the effect should occur to various extents in other nano-materials.

### 3.1 Introduction

Dislocations are defined as a boundary between deformed and nondeformed regions in the crystalline structure. In other words, dislocation line represents the slip front of propagation of a line defect. The Burgers vector, which is generally used to define a dislocation in a crystal, depicts the direction and amount of slip. Its magnitude gives a characteristic discontinuity of displacement caused by dislocation. There are two basic types of dislocations, i.e., edge and screw

dislocations, which are schematically shown in Fig. 3.1.

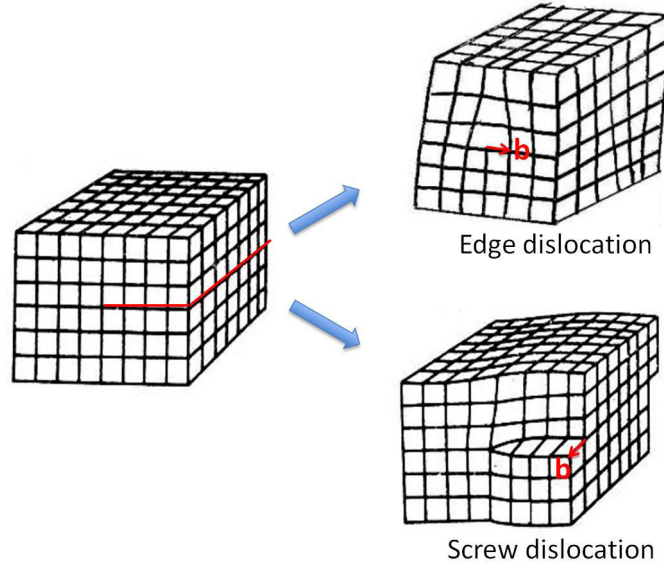


**Figure 3.1:** Schematic of the formation of an edge and a screw dislocation from a perfect lattice (left).

Typically, dislocations are studied in relation with the mechanical properties of materials. They allow plastic deformations to occur at lower applied stresses since they permit glide of one entire crystal plane over the one below in a discrete way. Besides, the motion, multiplication, and interaction of dislocations cause strain hardening, a common phenomenon in which continued deformation increases the strength of a crystal. The strength and ductility, and thereby the mechanical behavior of a crystal, are controlled by dislocations.

Dislocations distort the crystal structure in a complex manner. Away from the dislocation line, the deformation field can be well described with linear elasticity, the highly deformed core region is inaccessible to continuum methods, and it is largely treated on an empirical basis. For example, consider a screw dislocation of Burgers vector's magnitude  $b$ . The elastic strain energy is calculated by integrating the strain energy density and by simply adding an empirical core term  $E_c$ ,

$$E_{screw} = \frac{Gb^2}{4\pi} \ln\left(\frac{R}{r_c}\right) + E_c \quad (3.1)$$

where  $G$  is the shear modulus of a material,  $R$  and  $r_c$  denote the outer dimension of the structure and the dislocation core size, respectively.

Because screw dislocations offer a non-vanishing growth step at surface allowing the growth to advance in a spiral manner without the need for nucleation of a new layer, they are of importance for the growth of both bulk crystals and nanomaterials (Morin et al. 2010; Morin and Jin 2010; Bierman et al. 2008). Recent experiments presented convincing evidences that both nanowire (Bierman et al. 2008; Jin et al. 2010) and nanotubes (Morin et al. 2010; Morin and Jin 2010) can be grown via a common mechanism of the propagation of an axial screw dislocation (Fig. 3.2). According to classical crystal growth theory, the supersaturation of a system can be manipulated to dictate the growth mechanism. At low supersaturation, dislocation-driven spiral growth prevails, at intermediate the layer-by-layer growth dominates, while at high supersaturation, dendritic growth sets in. Therefore, screw dislocation line defects provide an endless source of crystal steps to enable nanostructure growth at low supersaturation conditions. As yet, screw dislocations have been identified in a variety of quasi-one-dimensional materials, including (Morin and Jin 2010; Bierman et al. 2008; Meng et al. 2013; Jacobs et al. 2008; Jia et al. 2008; Maestre et al. 2011; Wu et al. 2012; Hanrath and Korgel 2003) PbS, GaN, PbSe, PbTe, ZnO, Si, Ge, In<sub>2</sub>O<sub>3</sub>, InP, Cu<sub>2</sub>O, CdSe and CdS. Moreover, the dislocation-driven growth just reached the point where realistic progress can be made towards growing nanomaterials with controllable morphologies (Burgers vectors, chirality, nanotubes or nanowires), in large quantities, and at reasonable costs. Unfortunately, little is known about the way dislocations influence the properties of these new states of matter.

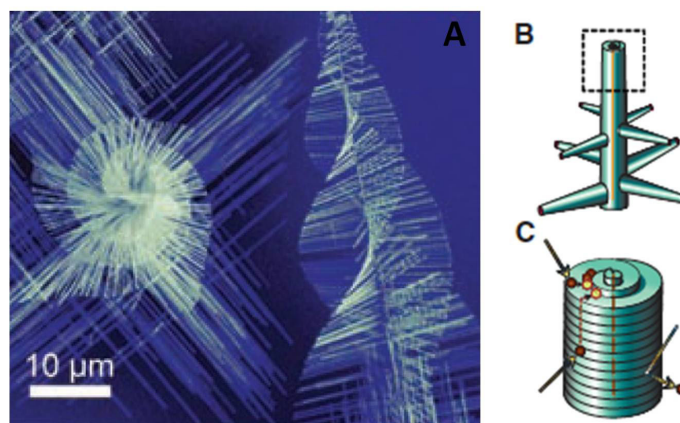


**Figure 3.2:** (a) SEM microscopy of screw dislocations in a PbS nanowire; (b) schematic representation of screw-dislocation-driven trunk growth combined with slower epitaxial vapor-liquid-solid-driven branch growth; (c) a simplified scheme illustrating that the self-perpetuating steps of a screw dislocation spiral at the tip of a trunk can enable 1D crystal growth of nanowires. Figure from M. J. Bierman et al, *Science*, 2008, 320: 1060.

### 3.2 Impact of Dislocation on Thermal Conductivity: The Classical Theory

In the early work of Klemens (Klemens 1958), dislocation was recognized as one of the main sources of phonon scatterers. The various scattering mechanisms are treated as perturbations to the harmonic approximation. Scattering probabilities are then computed with the Fermi Golden rule while transport properties are captured by the Boltzmann transport equation. After invoking the Debye approximation for the phonon dispersion, Klemens expressed the thermal conductivity as an integral over all possible phonon frequencies  $\omega$

$$\kappa = \frac{1}{2\pi^2 v} \int_0^{\omega_d} C_v(\omega) \omega^2 \tau d\omega \quad (3.2)$$

where  $C_v$  is the heat capacity at constant volume and at a given frequency,  $\omega_d$  to the Debye frequency, and  $\tau$  to the phonon lifetime. The phonon lifetime caused by the dislocation scattering is mixed in with different effects via the Matthiessen's rule (Berman 1976)

$$\frac{1}{\tau_{dis}} = \frac{1}{\tau_s} + \frac{1}{\tau_c} + \frac{1}{\tau_d} \quad (3.3)$$

where  $\tau_s$ ,  $\tau_c$ , and  $\tau_d$  are the contributions from the linear-elastic strain field of the dislocation, the non-linear elastic region of the dislocation, and the dislocation dynamics, respectively. The linear-elastic strain field contribution can be written as (Klemens 1958)

$$\frac{1}{\tau_s} \propto N_d b^2 \gamma^2 \omega \quad (3.4)$$

$N_d$  is the dislocation density,  $b$  is the magnitude of the Burger's vector, and  $\gamma$  the Grüneisen parameter. The effect of the non-linear elastic region of the dislocation is expressed as (Klemens 1958)

$$\frac{1}{\tau_c} = N_d \frac{r_c^4}{v_p^2} \gamma \omega^3 \quad (3.5)$$

where  $r_c$  is the radius of the dislocation core and  $v_p$  is the phonon phase velocity. Finally, the dislocation dynamics term, which accounts for the dislocation motion, can be approximated as (Kneeze and Granato 1982; Ninomiya 1968)

$$\frac{1}{\tau_d} \propto \frac{1}{\omega} \quad (3.6)$$

The analytical theory of Klemens correctly predicts a decrease in thermal conductivity *perpendicular* to the dislocation line. However, as it is well recognized nowadays, its use in the present context is limited to qualitative predictions. This theory fails by at least an order of magnitude in comparison with the experimental data (Sproull et al. 1959). Moreover, in the cases of screw dislocated nanowires and nanotubes, we encounter the unexplored case of thermal transport *along* the dislocation line. As a result, to predict the thermal conductivity of dislocated nanowires or nanotubes from the underlying atomic-level molecular dynamics resulting from rigorously described interatomic interactions is of vital importance to understand the impact of dislocation on heat transfer.

### 3.3 Simulation Details

We simulated a set of pristine and screw dislocation (SD) Si  $\langle 110 \rangle$  nanowires (NWs) and nanotubes (NTs) with cubic diamond structure and hexagonal cross sections. The number of 111 layers  $L$  in the cross-section was taken to be 12, 16, 20 and 30, so that the radii of the created NWs ranged from 18.8 Å to 47.1 Å. Next, from the pristine  $L = 12$  NW we created a set of  $(L, h)$  NTs, by systematically removing central atomic layers. We label by  $h$  the number of 111 inner layers that have been removed. Finally, in all these structures, we introduce SDs with the axis located at the center. We considered minimal Burgers vector of magnitude  $b = 3.8$  Å and multiples of it,  $2b$  and  $3b$ . In  $1b$  NWs, the created core structure is of Hornstra type, where all atoms remain fourfold coordinated.

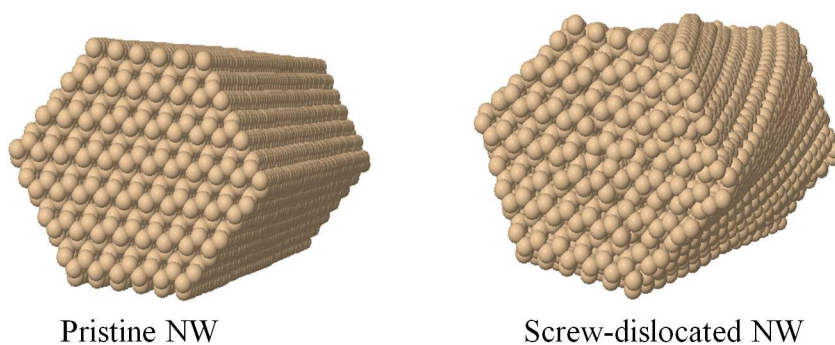


**Figure 3.3:** Schematic presentation of a simulated pristine Si nanowire (left) and a dislocated Si nanowire with Eshelby twist (right).

As evidenced by experiment (Morin et al. 2010; Morin and Jin 2010; Bierman et al. 2008; Jin et al. 2010) and theory (Akatyeva et al. 2012; Akatyeva and Dumitrică 2012; Nikiforov et al. 2011; Zhang et al. 2011), the axial screw dislocation couples to the shapes of NWs and NTs, by twisting them. This is the Eshelby twist (Eshelby 1953)  $\gamma_E$ , which is well known at the macroscale. Fig.

3.3 shows one example of a pristine and screw dislocated NWs. The presence of  $\gamma_E$  creates challenges for the atomistic simulations as it prevents the applicability of the standard periodic boundary conditions with the conventional small unit cells. Here, in order to find the optimal morphologies (atomic positions, unit cell length, and twist angles corresponding to minimum energy), we used objective MD (Dumitrica and James 2007) coupled with a Tersoff classical potential (Tersoff 1989). The method allows for performing simulations of SD NWs and NTs under arbitrary twist in an economic fashion without introducing any additional approximations, always using the same  $N$  number of atoms located in the primitive cell of the pristine structure. The infinitely long NWs and NTs are described as objective structures (James 2006; Akatyeva et al. 2012), with

$$\mathbf{X}_{j,\zeta} = \mathbf{R}^\zeta \mathbf{X}_j + \zeta \mathbf{T}, \quad j = 1, \dots, N; \quad -\infty < \zeta < \infty \quad (3.7)$$

where  $\mathbf{X}_{j,\zeta}$  and  $\mathbf{X}_j$  represent the cartesian coordinates of atom  $j$  located on the cell labeled by integer  $\zeta$  and initial cell, respectively. Matrix  $\mathbf{R}$  indicates a rotation with angle  $\theta$  around the direction indicated by the vector  $\mathbf{T}$ . In objective molecular dynamics, only the  $N$  atoms in the initial cell are explicitly simulated under the objective boundary conditions indicated by Eq. 3.7.

After the relaxation with objective molecular dynamics, non-equilibrium molecular dynamics simulations were carried out with LAMMPS code (Plimpton 1995) for long NWs and NTs constructed with the optimized structures. During this procedure, a temperature gradient was imposed on the system by thermostating different "bath" regions at different temperatures. From the variety of thermostating options, we used the Nosé-Hoover (Nosé 1984; Hoover 1985) thermostat. With the structure oriented along the  $z$  direction, we applied fixed boundary conditions on the end atomic layers. Next to these fixed layers, multiple layers of atoms were placed into hot and cold baths with temperatures  $T_H = T_0 + \Delta/2$  and  $T_C = T_0 - \Delta/2$ , respectively, with  $T_0 = 300K$  the mean temperature and  $\Delta = 20K$  the temperature difference. A 5 ns run was performed to reach steady-state, and another 5 ns run to time-average the local temperature  $T$  and heat flux  $j$  along  $z$ .  $\kappa$  was then extracted with the Fourier's law.

It is important to realize that the simulations are subject to size effects due to phonon scattering at the system (or thermostat) boundaries, and restrictions on the maximum phonon mean free path. The finite size thermal conductivity has been extrapolated up to the bulk value using analytical predictions (Schelling et al. 2002).

## 3.4 Physical Analysis of SD NWs and NTs Thermal Conductivity

### 3.4.1 Structure Optimisation and Eshelby Twist Angle

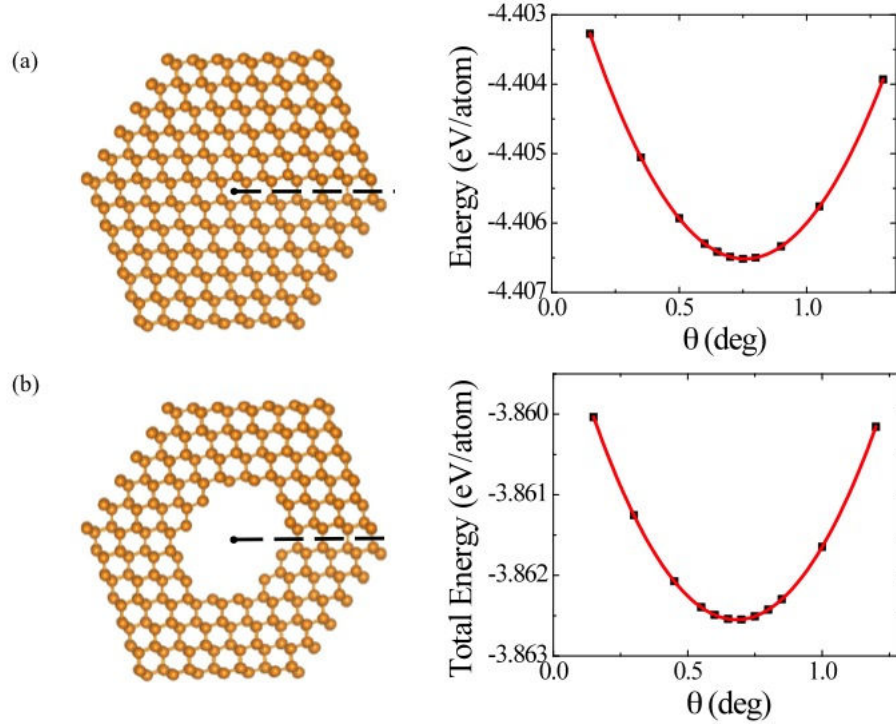


**Figure 3.4:** Optimal configuration (left) and total energy vs. twist angle (right) for (a)  $(12,0)$  NW and (b)  $(12,4)_b$  NT. The dashed line indicates the cut made to create the dislocation.

Examples of optimized structures are shown in Fig. 3.4. Each structure corresponds to the minimum of the computed total energy vs. twist angle  $\theta$ . As illustrated in table 3.1, in accordance with Eshelby theory (Eshelby 1953) we find that  $\gamma_E$  increases with the magnitude of the Burgers vector. As shown in Fig. 3.5, for all of the diameters studied, the twist angle increases linearly with the Burger's vector. Moreover, we find that  $\gamma_E$  decreases with the enlargement of the size of NWs, which is also in agreement with Eshelby theory. With the remove of the core (corresponding to NTs), the Eshelby twist decreases. This is because the Eshelby twist is originating from the highly distort core, where the deformation is plastic. With the remove of the core region, the strain energy produced by dislocation is released and the twist angle decreases. Moreover, the obtained  $\gamma_E$  and formation energies of the dislocations compare very well with those computed with a higher-level *ab initio* description of bonding (Akatyeva

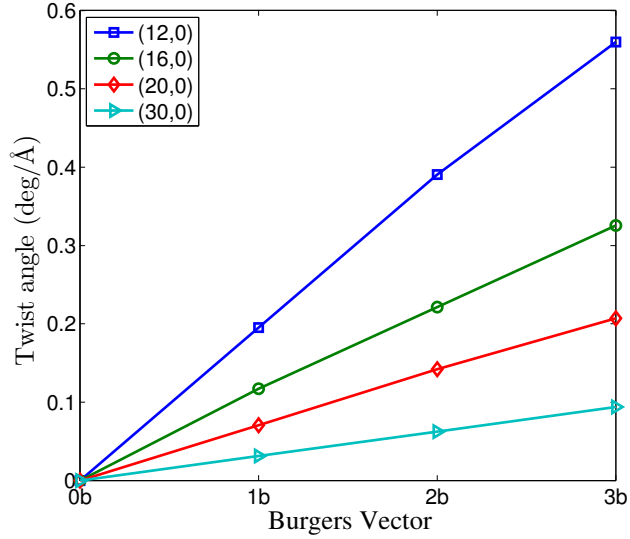


**Figure 3.5:** Eshelby twist angles as a function of the Burger's vector magnitude for SD NWs with specific diameters.

et al. 2012), thus indicating the reliability of our modeling. Note also that the dislocation does not affect the surface structural relaxation (Morin et al. 2010).

The formation energy  $E_f$ , which is defined as the difference between the total energy of a considered structure and its corresponding bulk state with the same number of atoms, has also been calculated. For a NW or NT,  $E_f$  contains only the surface energy term. While for a SD NW or NT, an additional strain energy of the dislocation term  $E_{fd}$  should be included.  $E_{fd}$  can also be explained as the formation energy of a dislocation and it can be deduced as

$$E_{fd} = E_f - E_f(p) \quad (3.8)$$

where  $E_f(p)$  is the formation energy of the corresponding NW or NT.

Fig. 3.6 represents the formation energies compared to the corresponding bulk state and NW/NT state as a function of  $h/L$  with  $L = 12$ . For the pristine NWs or NTs, due to the linear increase behavior of surface areas with  $h/L$ , the formation energy increases linearly with  $h/L$  as shown in Fig. 3.6(a). While for SD NWs and NTs,  $E_f$  increases slowly when  $h/L$  is small and the increase rate becomes larger and larger when enlarges the hole size and finally converges to the value of the pristine NT. This phenomenon originates from the fact that the strain energy of a dislocation is mostly stored at the core region of a dislocation. This is shown more clearly in Fig. 3.6(b), where the formation energy of a dislocation decreases quickly with the increase of the hole size.

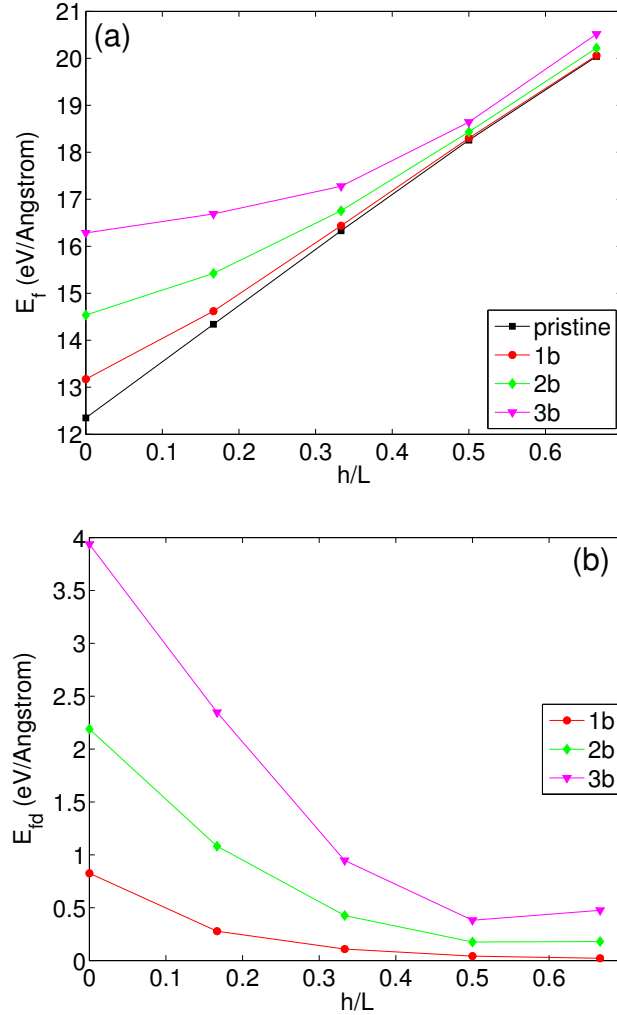


**Figure 3.6:** Formation energies as a function of the ratio  $h/L$  with  $L = 12$ . (a) formation energies compared to bulk state ( $E_f$ ); (b) formation energies compared to the corresponding pristine structures ( $E_{fd}$ ).

### 3.4.2 Thermal Conductivity

Having identified the atomic positions inside the objective cell and  $\gamma_E$ , we constructed long nanostructures. We computed the thermal conductivity with the direct method, based on nonequilibrium classical MD at a 300 K mean temperature as detailed in the previous section. During our MD runs, the NWs and NTs maintain their crystalline structure as well as the central location of the dislocation. Thereby, we recognize that scattering by other defects (vacancies, isotopes et al) and dislocation motion (Klemens 1958) contributions are not included in our results. Nevertheless, our MD simulations are subject to size effects. Therefore, for the (12,0) NWs and (12,4) NTs, we simulated structures

with lengths of 10, 20, 30, and 40 nm. The computed finite-size thermal conductivity has been extrapolated (Schelling et al. 2002) to predict  $\kappa$  for the infinitely-long structure.

**Table 3.1:** Number of Si atoms in the objective cell, twist, energetics, and thermal conductivity of (12,0) NWs and (12,4) NTs. The magnitude of the Burgers vector (1b, 2b, and 3b, where b = 3.8 Å) is indicated in the subscript notation.

(L,h)	N	$\gamma_E$ (deg/Å)	$E_f$ (eV/Å)	$\kappa$ (W/m·K)**
(12,0)	228	0	0	50
(12,0) <sub>b</sub>	228	0.19(0.19*)	0.79(0.94*)	36
(12,0) <sub>2b</sub>	228	0.39 (0.36*)	2.05 (2.15*)	20
(12,0) <sub>3b</sub>	228	0.56 (0.53*)	3.74 (3.40*)	12
(12,4)	204	0	0	28
(12,4) <sub>b</sub>	204	0.18	0.09	23
(12,4) <sub>2b</sub>	204	0.35	0.35	17
(12,4) <sub>3b</sub>	204	0.52	0.77	12

\* These values, shown here for a comparison, were obtained with a density-functional-theory based method (Akatyeva et al. 2012).

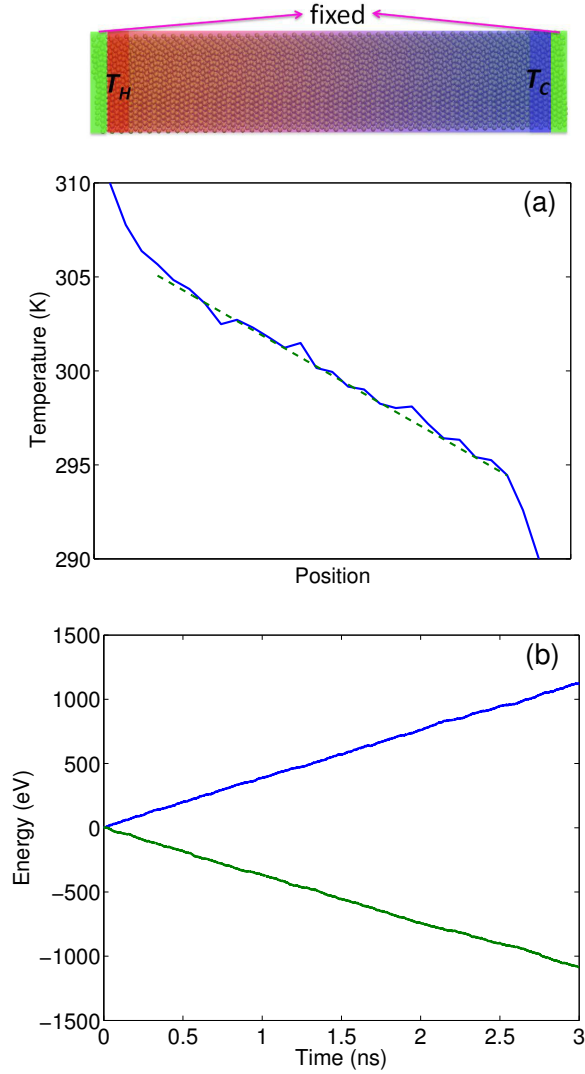
\*\* These values correspond to the infinitely-long structures.

Fig. 3.7 depicts an example of the simulation set up of a SD NW with a Burger's vector of 2b for measuring the thermal conductivity. Fixed boundary conditions are applied on the end atomic layers. Next to the fixed layers, multiple layers are coupled to thermal baths with temperatures 310 K and 290 K, respectively. The temperature profile averaged over 5 ns is shown with the solid line in Fig. 3.7(a). In the intermediate region, the temperature varies linearly along the NW and the temperature gradient can be measured in this region with a linear fit (dashed line). The time evolution of the total energy injected into the hot bath and subtracted from the cold bath is shown in Fig. 3.7(b). These two curves (corresponding to energy injection and subtraction) should be nearly symmetric according to energy conservation. The heat flux  $j$  used to deduce the thermal conductivity calculated as

$$j = \frac{1}{2} \left( \left\langle \frac{dE_{in}}{dt} \right\rangle - \left\langle \frac{dE_{out}}{dt} \right\rangle \right) \quad (3.9)$$

where  $E_{in}$  and  $E_{out}$  denote the total energy injection and subtraction.  $\langle \dots \rangle$  means the average over time.

Consistent with previous studies, we find that the presence of surfaces in pristine Si NWs leads to significant thermal conductivity reduction. For example, in a (12,0) NW we measured  $\kappa = 50$  W/m·K, which represents 25% of the



**Figure 3.7:** Example of thermal conductivity measuring set up with NEMD method for a SD NW with  $2b$  Burger's vector (top). The atoms at the two ends are fixed and next to the fixed layers, a couple of atom layers are coupled to the Nosé-Hoover thermal bath with the temperature  $T_0 + \Delta/2$  and  $T_0 - \Delta/2$ , respectively. (a) Raw data of the averaged temperature profile (solid line) and the linear fit (dashed line) for the intermediate region; (b) Energy  $E$  injected into and subtracted from the hot and cold thermal baths, respectively.

bulk Si value (He and Galli 2012) of 196 W/m·K. This value agrees well with that obtained from other simulations (Hu et al. 2011) but is larger than in experiment (Li et al. 2003) because realistic effects, such as structural defects (He and Galli 2012; Martin et al. 2009), are not included. Nevertheless, our pristine structures only serve here as useful references, to help us distinguish

the potential impact of SDs.

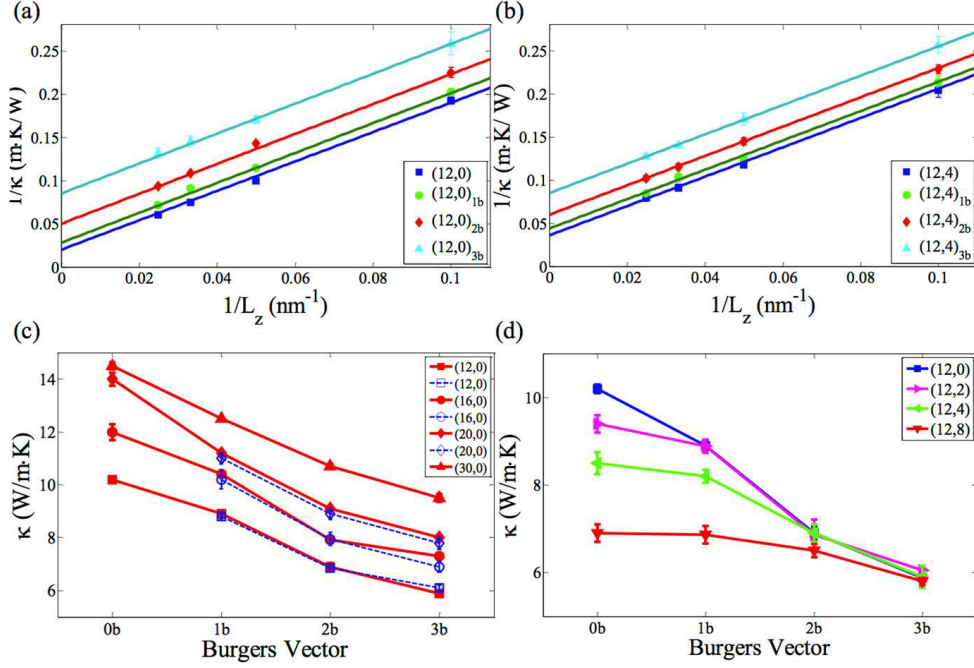


**Figure 3.8:** Dependence of  $1/\kappa$  on  $1/L_z$  for pristine and SD (a) (12,0) NWs and (b) (12,4) NTs. The intercept of the linear fit with the vertical axis gives for infinitely-long structures. Relative comparison of for (c) NWs and (d) NTs with  $L_z = 20$  nm. The filled (open) symbols correspond to untwisted (twisted) structures. Here  $b = 3.8$  Å.

Remarkably, a screw dislocation leads to a sizable  $\kappa$  decrease. The values entered in the last column of Table 3.1, demonstrate a consistent decrease in  $\kappa$  with the magnitude of the Burgers vector. Likewise, an open core dislocation in NTs is reducing  $\kappa$  to a similar extent. For example, in both (12,0)<sub>3b</sub> NWs and (12,4)<sub>3b</sub> NTs,  $\kappa = 12$  W/m·K, which represents only 6% of the bulk value.

For more insight, Fig. 3.8(c) shows the computed thermal conductivity for a series of NWs 20 nm in length. In Eshelby's theory, the amount of twist depends inversely on the cross-sectional area, so it decreases with the NW diameter. For example a (30,0)<sub>b</sub> NW stores a twist of only 0.03 deg/Å. Fortunately, Fig. 3.8(c) demonstrates that the Eshelby twist does not play a key role for heat transport. The reduction in  $\kappa$  occurs to the same extent in smaller and larger diameter untwisted and twisted NWs.

In Fig. 3.8(d) we compare the dependence of thermal conductivity on the Burgers vector for NTs with different inner diameters. In pristine NTs, we find that the effect of the gradual increase of the inner surface is beneficial for thermo-

electricity, as it leads to a  $\kappa$  decrease. When accounting for the size effects in the same manner as in Fig. 3.8(b), we obtained a 56%  $\kappa$  reduction between pristine (12,4) NTs and (12,0) NWs (see Table 3.1). This is an interesting result by itself considering the recent progress in the synthesis of pristine Si NTs (Ishai and Patolsky 2009). Examining now the SD data, we find that as the NT's wall gets thinner, the impact of SD on  $\kappa$  diminishes: While in (12,2) NT the strain field leads to a significant  $\kappa$  reduction, in (12,8) NT  $\kappa$  is hardly affected by the size of the Burgers vector. Moreover, the thermal conductivity of SD NT with a hollow size near to the Burger's vector is almost the same with the one without hollow, indicating the contribution of the thermal conductivity from the core region is negligible. As a result, hollow sizes smaller than the size of distorted core will not affect thermal conductivity of dislocated NWs. This phenomenon may lead to design metamaterials and tune the material properties. For example, in core-shell structures, if we introduce a dislocation in the centre of the structure and the core is of the same size as the one of the dislocation distort region, we may change the core material and the thermal conductivity will not be affected while the other properties, such as electronic properties, may be designed. Overall, this study shows that the thermal reduction is strongly linked to the complex SD strain field, which is most severe at the core and significantly diluted in strength near the outer surface.

### 3.4.3 Eigen-mode Analysis

What is the microscopic mechanism responsible for lowering the thermal conductivity? In search for the answer, we have first invoked the harmonic approximation and performed a mode analysis within the solution  $\vec{u}_{n,\lambda} \propto \vec{\epsilon}_{n,\lambda} \exp(i\omega_\lambda t)$ . Here  $\vec{u}_{n,\lambda}$  is the displacement of atom  $n$  and  $\lambda$  denotes the phonon-mode branch. The eigenfrequencies and eigenvectors were obtained by numerically solving the lattice dynamical equations. The oscillation direction of these modes is provided by the unit polarization vector  $\vec{\epsilon}_{n,\lambda}/|\vec{\epsilon}_{n,\lambda}|$  (More details for mode polarization calculation can be found in Chapter 2). In Fig. 3.9, points have the x and y components of the longitudinal acoustic polarization vectors near 2 THz.

We find that under dislocations, the polarization characteristics differ considerably: In Fig. 3.9(a), the points are concentrated around the center with x and y components near 0. Thus, the modes of the pristine (12,0) NW have one dominant polarization along z (wave vector direction), approaching the case of phonon in a bulk crystal with a well-defined polarization. In Fig. 3.9(b), points are distributed in a broader range, with x and y components much larger than the one of pristine for a large portion of modes. This depolarized nature of the (12,0)<sub>3b</sub> NW modes resembles instead the amorphous structure case. Since loss of polarization is associated (Bodapati et al. 2006) with low thermal conductivity, our analysis might suggest that the  $\kappa$  reduction is linked to the differences

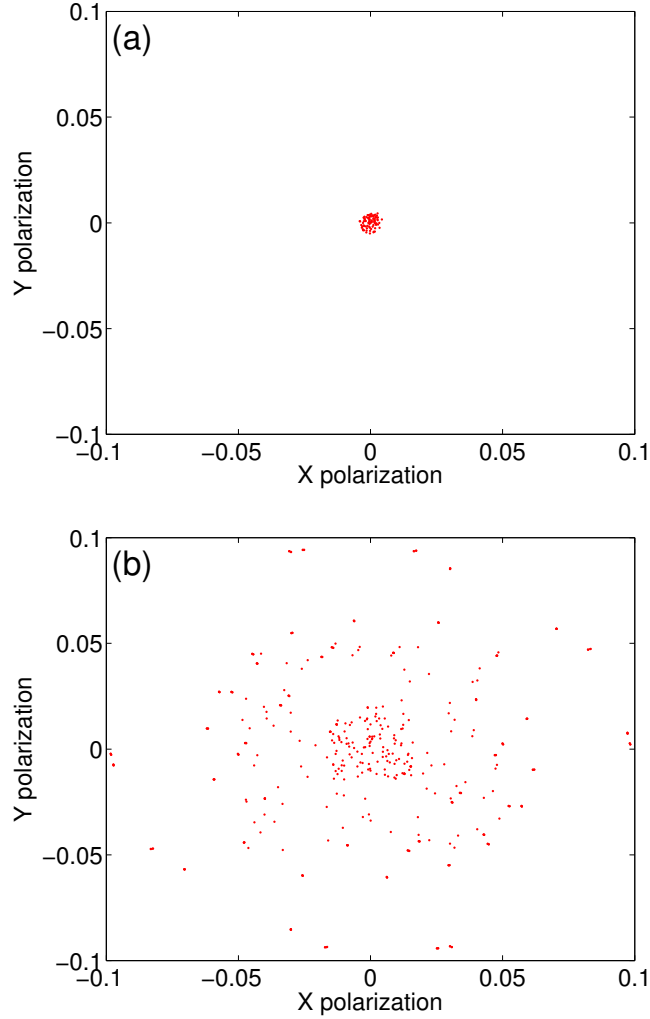


**Figure 3.9:** Phonon polarization distributions of a longitudinal acoustic mode for (a)  $(12,0)$  and (b)  $(12,0)_{3b}$  NWs at the frequency 2 THz.

in microscopic structure.

### 3.4.4 Green's Function Analysis

Before drawing a conclusion, we have further investigated how differences in vibrational modes impact thermal transport. For this, we performed atomistic Green's function (AGF) conductance calculations within the harmonic approximation, Fig. 3.10(a). Note that AGF captures all wave-related scatterings (including surface scatterings) and quantum populations of phonons. To our surprise, we find that the transmittance curves for the pristine and SD  $(12,0)$

NWs practically overlap, leading to small differences in thermal conductance, Fig. 3.10(b). For example, at 300 K there is a thermal conductance decrease of 7%, 12% and 18% for  $(12,0)_{1b}$ ,  $(12,0)_{2b}$ , and  $(12,0)_{3b}$  NWs, respectively. Overall, this amounts to only 25% of the total thermal conductivity decrease obtained in MD. The key point is that AGF analysis rules out the hypothesis that the significant  $\kappa$  reduction can be mainly attributed to differences in structure since all the structure information is contained in the force constant matrices.

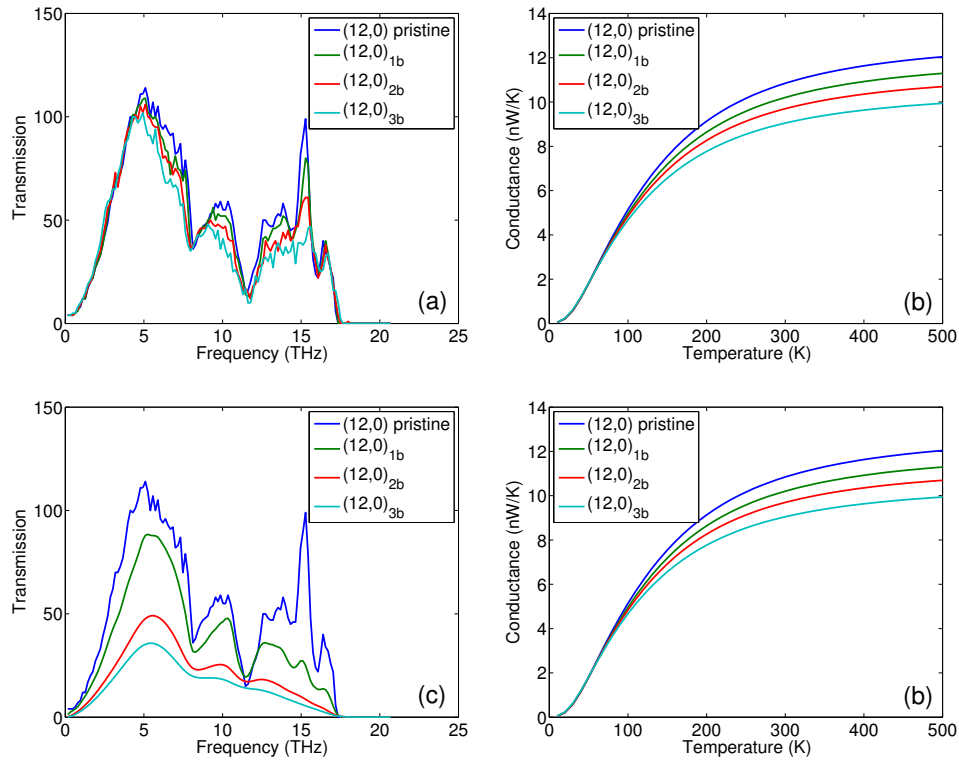


**Figure 3.10:** (a) Phonon transmission function and (b) thermal conductance under harmonic approximation for  $(12,0)$  pristine and SD NWs; (c) modified phonon transmission function and (d) thermal conductance with manually introduction of anharmonicity.

The only remaining way to explain our notable MD results is to go beyond the harmonic approximation and accept that phonons can be scattered by other phonons. Indeed, the harmonic approximation is permissible as long as atoms remain very close to their equilibrium positions, forming bond lengths of 2.36 Å. Instead, in SD NWs large strains are involved. For example we identified bond lengths measuring 2.5 Å in the Hornstra core of the  $(12,0)_{1b}$  SiNW. Thus, anharmonicity of the interatomic potential is expected, which leads in turn to

phonon-phonon scatterings (Li et al. 2010; Chalopin et al. 2012).

To implement the anharmonic effect in the AGF formalism, we manually insert anharmonicity by broadening each phonon eigenfrequency with a relaxation time  $\tau$ , by replacing the frequency by  $\omega + \frac{i2\pi}{\tau}$ . For qualitative predictions, we have used the frequency-independent  $\tau$  approximation, where the meaning of  $\tau$  becomes the mean-scattering time. The  $\tau$  values matching the MD data with the same decrease percentage were 9.5 ps, 4.7 ps and 2.7 ps for the (12,0)<sub>1b</sub>, (12,0)<sub>2b</sub>, and (12,0)<sub>3b</sub> NWs, respectively. (Note that the  $\tau$  decrease with the increase in the Burgers vector magnitude means an increase in phonon anharmonicity.) We emphasize that non-harmonic behavior exists in the pristine and SD NWs due to other causes, such as inelastic scattering on surfaces. The above  $\tau$  values solely capture the effects of SDs. With the incorporated  $\tau$ , the AGF-predicted transmission functions for SD NW are significantly reduced with respect to the pristine one, Fig. 3.10(c). This leads indeed to a more sizable conductance decrease at all temperatures, Fig. 3.10(d).

An attractive feature is that the effect uncovered here can act in combination with the known thermal conductivity limiting mechanisms. To illustrate this point, we have performed exploratory MD calculations on (12,0) Si NWs coated with four layers of Ge. After accounting for the size effects, we obtained that the addition of a Ge shell leads to  $\kappa = 40$  W/m·K for NW with pristine core, and to the even smaller values of 28.6, 11.8, and 7.2 W/m·K for (12,0)<sub>1b</sub>, (12,0)<sub>2b</sub>, and (12,0)<sub>3b</sub> NWs, respectively.

In conclusion, we investigated  $\langle 110 \rangle$  Si NWs and NTs containing an axial screw dislocation and uncovered a sizable thermal conductivity reduction with respect to the pristine structures. We attributed this effect to the enhanced phonon-phonon scattering caused by the potential anharmonicity in the highly-distorted cores and, to a lesser extent, to differences in structure. As high-strain is intrinsic to dislocations, the effect should occur to various extents in other nano-materials. Our finding is especially important for thermoelectricity. The thermal effect of SDs can be combined with other  $\kappa$ -lowering mechanisms.

### 3.5 Conclusions

In this chapter, we briefly introduced the line defect dislocation in materials and the classical Klemens theory accounting for the effect of dislocation on heat transfer in the direction perpendicular to dislocation lines. We emphasize the failure of this theory in quantitatively predicting the thermal conductivity decrease by dislocations and the uninvestigated heat transfer behavior along the dislocation line direction, especially in the recent fabricated SD nanomaterials (NWs and NTs). To quantitatively predict the thermal conductivity along

the dislocation line, we performed molecular dynamic simulations for SD Si NWs and NTs in the  $\langle 110 \rangle$  crystallographic direction. The structure relaxation, Eshelby twist angle, as well as formation energy of SD NWs and NTs were firstly carried out with objective molecular dynamics, which allows to perform the simulations with a small unit cell by applying the objective boundary conditions. We found that in accordance with the Eshelby theory, the twist angle of a SD NW or NT increases with the Burger's vector while decreases with the cross-section area. After identifying the Eshelby angle, long NWs and NTs were constructed and thermal conductivity was calculated with NEMD simulations for different wire lengths. The thermal conductivity was extrapolated to infinite long structures. It was found that a large thermal conductivity suppression can be achieved for the NWs and NTs containing an axial screw dislocation with respect to pristine structures. The phonon mode polarization calculation together with the phonon Green's function calculation reveal that the sizeable reduction of thermal conductivity by dislocation is attributed to the enhanced phonon-phonon scattering caused by the potential anharmonicity in the highly-distorted core and, to a lesser extent, to differences in structure. To further illustrate whether the uncovered effect by dislocation can collaborate with other well-known effects, such as coating, we performed the thermal conductivity calculation of SD Si NW with 4 layers of Ge atoms coating. We found the thermal conductivity can be further decreased with the introduction of dislocations, which is of vital importance for extreme low thermal conductivity design and for the improvement of thermoelectricity performance.



## Chapter 4

# Structural Defects in Nanowires: Efficiently Phonon Blocking in SiC with Antiphase Superlattice Nanowires

The high thermal conductivity of SiC prevents the improvement of its thermoelectric figure of merit although excellent power factor has been achieved. Here we propose a new type of SiC superlattice, i.e. anti-phase superlattice nanowires (APSL NWs) composed of SiC only. Thermal conductivity of period modulated APSL NWs can be significantly reduced up to 52% at room temperature compared to the one of pristine NW, as shown by means of equilibrium molecular dynamics simulations. Similar to the heterostructure SLs, a minimum thermal conductivity is found at the period of 6 nm, which arises from phonon coherent transport in short period structures. Density of states studies reveal that new vibrational modes emerge on the interfaces due to the new Si-Si and C-C bond. The reduction of thermal conductivity is explained by the modification of the phonon group velocity, which is markedly suppressed in APSL NWs. Clear guidelines are provided here to design structures with minimal thermal conductivity and possibly promote SiC as a competitive thermoelectric material.

### 4.1 Introduction

Silicon carbide (SiC) is a broadly used and available semiconductor with a wide electronic band gap and a high saturated electron drift velocity. It also presents excellent mechanical and physical/chemical properties such as excellent strength, hardness, corrosion resistance and oxidation resistance, which make of SiC an excellent candidate for high temperature, high power and high frequency devices (Morko et al. 1994; Yang et al. 2001; Yang et al. 2005;

Cheng et al. 2014; KIM et al. 2009). For example, SiC is widely used in high-temperature/high-voltage semiconductor electronics due to its high breakdown voltage and excellent physical stability at high temperatures (Morko et al. 1994). Nanometer-scale SiC resonators are also capable of yielding substantially higher frequencies than GaAs and Si resonators (Yang et al. 2001). With the incorporation of randomly oriented single-crystal SiC NWs in a SiC matrix, the fracture toughnesses and flexural strengths of the composites doubles (Yang et al. 2005).

Recently, the thermoelectric properties of SiC have also been studied and it is shown that doped SiC can be a potential thermoelectric candidate at high temperatures (Cheng et al. 2014; KIM et al. 2009; Kim et al. 2011; Ivanova et al. 2006; Kitagawa et al. 2002; Wang et al. 2003). The efficiency of a thermoelectric material is characterized by the dimensionless figure of merit  $ZT = \frac{S^2\sigma T}{\kappa}$ , where  $S$  represents the Seebeck coefficient,  $\sigma$  and  $\kappa$  refer to the electrical and thermal conductivities, respectively. Kim et al (KIM et al. 2009; Kim et al. 2011) found that the thermoelectric properties of SiC could be significantly tuned by the effect of diluent gases and the chemical vapor deposition temperatures. Ivanova et al (Ivanova et al. 2006) found that heavy nitrogen doped SiC has a high power factor  $S^2\sigma$  value of  $1.7 \times 10^{-3} \text{ W}/(\text{m} \cdot \text{K}^2)$  in the temperature range from 1400 to 1600 K. With the doping of  $\text{Si}_3\text{N}_4$ , Kitagawa et al (Kitagawa et al. 2002) found that the power factor of SiC increased dramatically at high temperatures benefiting from the increase of both Seebeck coefficient and electrical conductivity. By means of thermal plasma physical vapor deposition, 300  $\mu\text{m}$  thick SiC films doped by nitrogen was fabricated by Wang et al (Wang et al. 2003) and the corresponding power factor reaches as high as  $1.0 \times 10^{-3} \text{ W}/(\text{m} \cdot \text{K}^2)$  at 973 K. Although the above mentioned studies show that SiC has a good power factor at high temperatures, its figure of merit is small due to the fatal shortcomings of a fairly large thermal conductivity  $\sim 100 \text{ W}/(\text{m} \cdot \text{K})$  even though at high temperatures. As a result, to make SiC a competitive thermoelectric materials, it is crucial to block phonon transport at least by one order of magnitude.

In the past decade, several studies have proven superlattices (SLs) to be efficient in blocking phonon transport. The cross-plane thermal conductivity of a crystalline SL can be one order of magnitude smaller than the values of bulk materials with a single component, and in some cases, even smaller than the value of a random alloy with the same components due to interfacial scattering (Cahill et al. 2014; Hyldgaard and Mahan 1997; Simkin and Mahan 2000; Koh et al. 2009; Lee and Venkatasubramanian 2008; Volz et al. 2000; Rajabpour and Volz 2010). However, most of the previous studies were focused on the heterostructure SLs, where materials in the two sides of interfaces are different. As a result, mass mismatch and lattice mismatch are usually regarded as the main phonon scattering mechanisms at the interfaces.

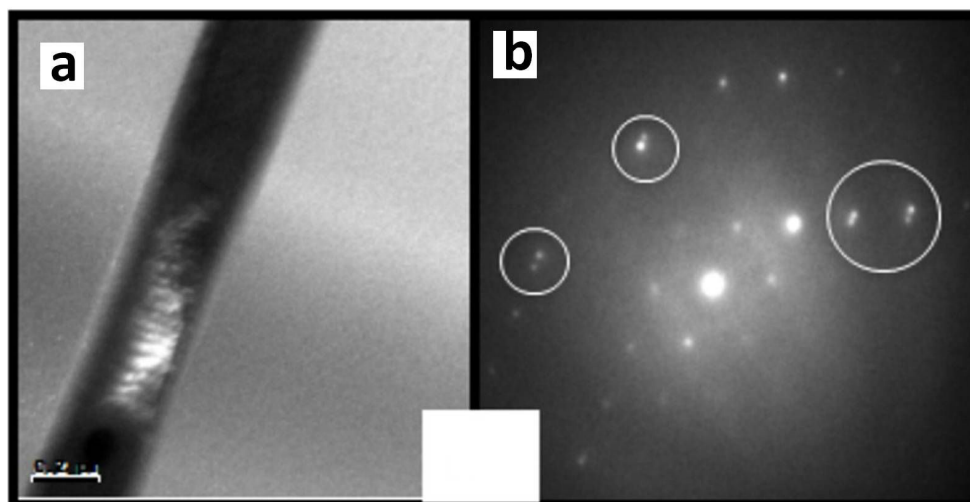


**Figure 4.1:** (a) The observation of a local anti-phase domain in GeTe nanowire from a TEM image. (b) electron diffraction image shows spot splitting (circled in white) along the nanowire growth direction. Figure from Pavan Nukala et al, *Nano Lett.* 14: 2201 (2014)

Anti-phase (AP) boundary/domain, in which the atoms are configured in the opposite order compared to the one of the perfect lattice, has been directly observed by experiments in many types of materials, such as GaN (Maria Kemper et al. 2011), Fe<sub>3</sub>Al (Marcinkowski and Brown 1962), SiC (Pirouz et al. 1987; Shibahara et al. 1987), and Fe<sub>3</sub>O<sub>4</sub> (Sofin et al. 2011). The peculiar properties and promising perspective in nanoelectronic design of domain boundaries have recently brought interest to this intriguing and challenging research subject. As one kind of domain boundary, AP domain shows attractive interest for both fundamental science and possible practical applications. For instance, the presence of AP boundary in Fe<sub>3</sub>O<sub>4</sub> films will induce a strong crystallographic direction dependence on the low-field magnetoresistance behavior (Sofin et al. 2011). AP boundaries in antiferroelectrics with a  $\pi$  phase shift of the order parameter exhibit polarity, implying the existence of local ferroelectricity (Wei et al. 2014) in the antiferroelectric material. The impact of AP domain on electronic properties has been investigated (Sofin et al. 2011; Wei et al. 2014), however, its influence on thermal properties is still unknown. Many materials possess translational AP boundaries, as a result, it is possible to fabricate SLs with AP domain. In fact, alternating AP domain has been locally found very recently in GeTe nanowires synthesised via vapor-liquid-solid process by Nukala et al (Fig. 4.1) (Nukala et al. 2014). This kind of new SLs are challenging for both electronic and thermal properties as the material on the two sides of the interfaces are composed by exactly the same elements but with atoms configured in the opposite order. Consequently, the conventional continuum models

for SLs properties, such as the effective mass model, are not applicable (Ikonić et al. 1993). In APSLs, the configuration of lattices are very much different from heterostructure SLs because no lattice mismatch and mass mismatch are involved. So it could be very interesting to study the fundamental phenomenons in the aspect of heat transfer, such as minimum thermal conductivity, phonon interface scattering and phonon coherence, which are commonly observed in heterostructure SLs.

In this chapter, we propose a new type of SiC SL nanowire – APSL nanowire for potential thermoelectric applications. Thermal conductivities of SiC APSL nanowires with different periods have been systematically studied with equilibrium molecular dynamics (EMD). It is found that the thermal conductivity of SiC APSLs can be significantly decreased, offering a possibility to increase the thermoelectric performance of SiC.

## 4.2 Structure and Simulations

SiC exhibits a variety of stable lattice structure and stacking fault polytypes, such as 2H, 3C, 4H and 6H. These structures differ only in the stacking order along the  $\langle 111 \rangle$  crystallographic direction, as shown in Fig. 4.2. In this work, we choose SiC with a 3C structure as our reference system. In the 3C structures, an  $\{111\}$  atomic layer contains one layer of Si and one layer of C atoms and the coordinates of Si/C layer can be obtained from C/Si layer with a shift of  $\frac{\sqrt{3}}{4}a$  in the  $\langle 111 \rangle$  direction, where  $a$  is the lattice parameter. So in a perfect SiC lattice, the arrangement of Si and C atoms in the  $\langle 111 \rangle$  direction can be either SiCSiC or CSiCSi. Now if the lattice stacks according to the SiCSiC sequence and changes at a given plane to the CSiCSi sequence, then an anti-phase boundary is formed. If this stacking sequence changes periodically, an anti-phase superlattice can be generated with C-C and Si-Si interfaces as shown in Fig. 4.3(a). The cross-section of APSL nanowires in the current study has been chosen as an hexagonal shape and with the diameter  $D = 3\text{nm}$  as depicted in Fig. 4.3(b).

The thermal conductivities were calculated by Equilibrium Molecular Dynamic (EMD) simulations with the LAMMPS code (Plimpton 1995). The interaction between atoms is described with the empirical Tersoff potential (Tersoff 1989). The equation of motion is solved with the velocity Verlet algorithm and a short integration time step of 0.15 fs was used to ensure the conservation of the total energy. Periodic boundary conditions are applied in all directions but with a vacuum surrounded in the x and y directions to mimic the infinite NW environment. The minimum length of the NWs in all the simulations is 18.2 nm, which is long enough to avoid the size effect on thermal conductivity. All the structures are fully relaxed in the isothermal-isobaric ensemble (NPT) corresponding

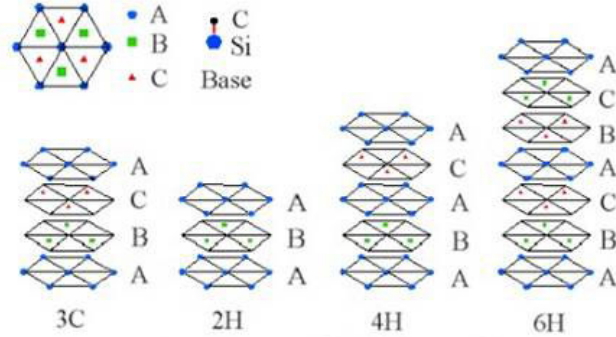


**Figure 4.2:** Stacking sequence of double layers of the four most common SiC polytypes. Figure from <http://staff.csc.fi/~raback/sic/thesis/node6.html>

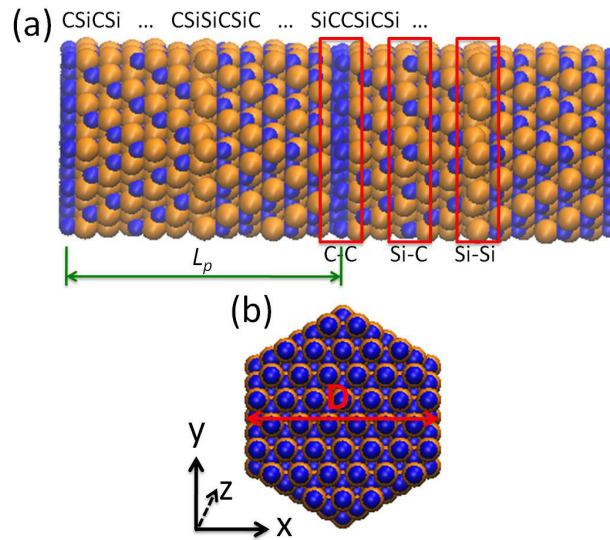


**Figure 4.3:** Schematics of the SiC APSLs; (a) A SL with two periods along the  $z$  direction showing the stacking sequence of Si and C atoms and the Si-Si and C-C interfaces; (b) An example of hexagonal cross-section of APSL nanowires.

to the target temperature and zero pressure for 1.5 ns with the coupling to a Nosé-Hoover thermostat (Nosé 1984; Hoover 1985) and in the canonical ensemble (NVT) for 1 ns. We then moved to the microcanonical ensemble (NVE) for 1 ns before collecting the data. Heat flux along the wire direction ( $z$ ) is then recorded every 60 timesteps (9 fs) for another 1 ns in the NVE ensemble. Thermal conductivity is calculated according to the Green-Kubo's formula (Kubo et al. 1985) with the averaging over 24 ensembles obtained by setting different initial random velocities.

### 4.3 Physical Analysis of SiC AP SLNW Thermal Conductivity

#### 4.3.1 Thermal Conductivity

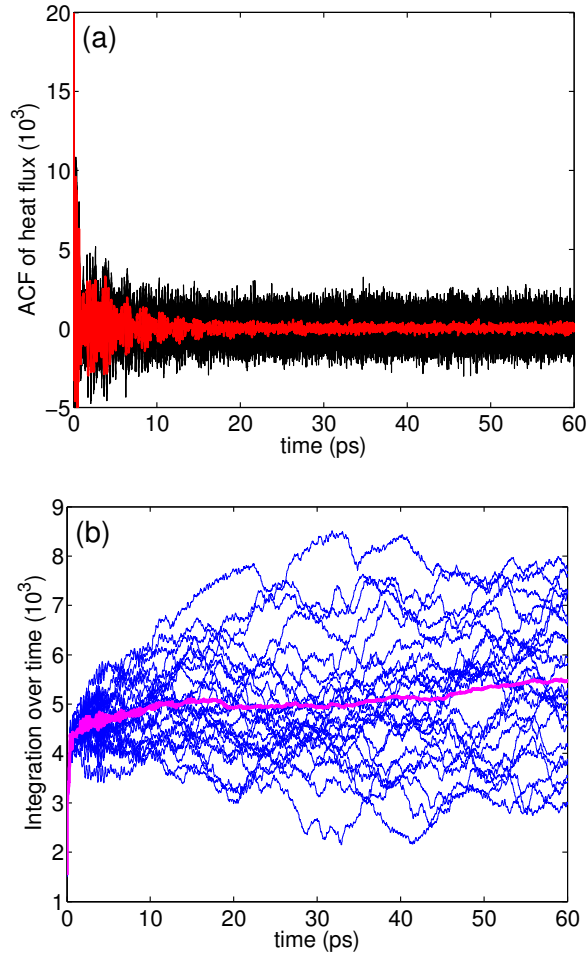


**Figure 4.4:** Example of a heat flux autocorrelation function (a) and its integral (b) vary with the correlation time for the antiphase nanowire with period of 9.06 nm. The black and blue curves are the ACF and ACF integral of each simulation (in total 24). The red curve in (a) and pink curve in (b) are the average of ACF and integral of ACF, respectively.

According to the fluctuation dissipation theory, thermal conductivity can be derived from the Green-Kubo formula, i.e., the integral of heat flux autocorrelation function (ACF). Fig. 4.4 depicts an example of ACF of the obtained heat flux during simulation and their corresponding integral. The averaged ACF (red curve in Fig. 4.4(a)) decreases rapidly at the beginning and then

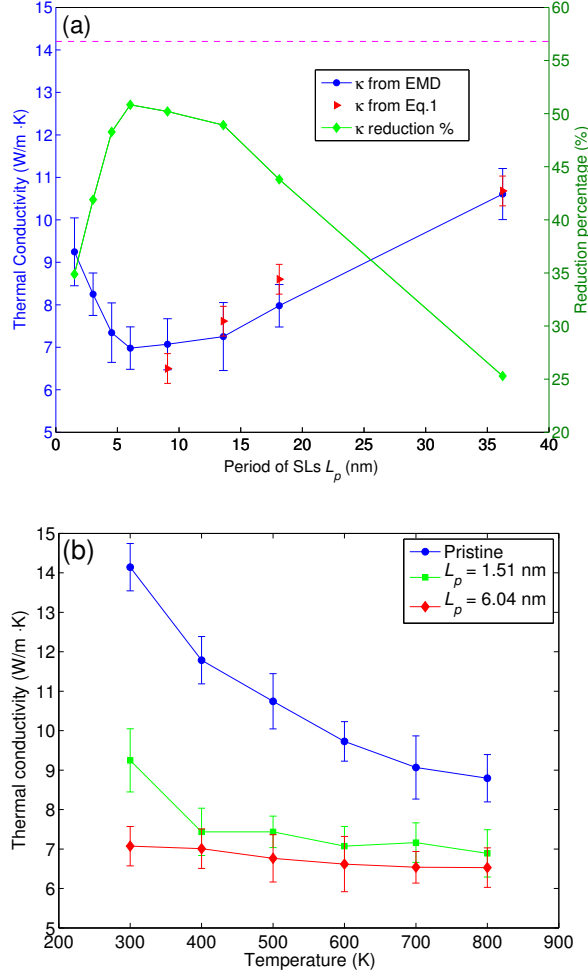


**Figure 4.5:** Thermal conductivity of APSL NWs with diameter of 3 nm. (a),  $\kappa$  as the function of period length  $L_p$  at 300 K (blue circles). Triangles correspond to thermal conductivities calculated with Eq. 4.1 and the dashed line denotes the thermal conductivity of pristine NW with the same cross-section. All these conductivities data refer to the left coordinate axis. Green diamonds, corresponding to the relative thermal conductivity decrease with respect to the one of pristine NWs, are referring to the right coordinate axis. (b),  $\kappa$  as a function of temperature for pristine and APSLs with specified periods.

changes to a smooth decrease with a long tail oscillating around zero. The rapid decay of ACF in short correlation time (about 1 ps) comes from the short mean free path phonons, which are scattered in a short time interval. While the long decay tail of ACF presents the long mean free path phonons having a long relaxation time. These phonons are typically long wave length acoustic phonons at the Brillouin zone centre. Due to the behavior of ACF, the

averaged integral of ACF (pink curve in Fig. 4.4(b)) increases with very large slope at the first 1 ps. After it increases gradually with time and reaches to a plateau. The value of the plateau is used to evaluate the thermal conductivity.

The thermal conductivity of APSL NWs 3 nm in diameter is depicted as the function of period in Fig. 4.5(a). Similar to heterostructure SLs, a minimum thermal conductivity is found around the period  $L_p = 6$  nm. The minimum thermal conductivity originates from the interplay between phonon wave effect and phonon particle behavior (Cahill et al. 2014). When the SL period is smaller than the wave packet coherence length, phonon wave effect is predominant and phonons do not scatter at the interfaces. This means that the atoms located in the two sides of the interface vibrate coherently and the phonons travel coherently along the wire. With the increase of the period, this coherence breaks down progressively and results in the decrease of the thermal conductivity. Now, if the period is larger than the wave packet size, the phonon particle behavior predominates. As a result, thermal conductivity increases monotonically with period as the interface density decreases. Compared to pristine NWs, the thermal conductivity of period modulated APSL NWs is notably reduced as revealed by the diamond symbols in Fig. 4.5(a). The maximum reduction around the thermal conductivity minimum can reach 52%, which corresponds to only 2.6% of bulk SiC value at 300 K (Samolyuk et al. 2011). With the increase of temperature, the thermal conductivity of the pristine NW decreases by a large amount due to the phonon-phonon scattering process while  $\kappa$  remains almost the same for period modulated APSL NWs as shown in Fig. 4.5(b). This latter behavior is due to the predominance of the interfacial scattering over the phonon-phonon scattering. The weak temperature dependence APSL thermal conductivity leads to a decrease of the relative  $\kappa$  suppression percentage with the increase of temperature. However, even at 800 K, the maximum thermal conductivity reduction can reach 33%, corresponding to about 6% of the bulk value (Samolyuk et al. 2011). This large thermal conductivity suppression may be beneficial to the thermoelectric performance of SiC in the form of APSL NWs especially if the electronic properties improve with increasing temperature.

### 4.3.2 Coherent and Incoherent Phonon Transport

To check the coherent phonon transport at short periods, we performed NEMD simulations of APSL NWs with different periods. The temperature profile along the wires is reported in Fig. 4.6. As clearly shown, the temperature profile is linear along the z direction for the small period case ( $L_p = 3$  nm). No temperature drop is observed across the interfaces, indicating that the atomic vibrations in the vicinity of the interfaces are coherent. With the increase of the period, phonon coherence becomes weaker and weaker and interfaces start to scatter phonons. As a result, a temperature drop at the interfaces starts to emerge.

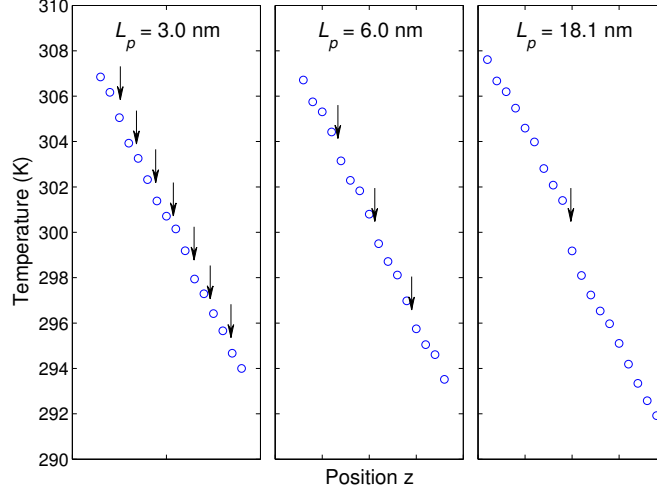


**Figure 4.6:** Temperature profile along  $z$  direction obtained from NEMD simulations for APSL NWs with periods  $L_p = 3$  nm, 6 nm and 18.1 nm, respectively. The arrows indicate the position of interfaces.

Since phonon interface scattering is predominant when the period is large, we measured the Kapiza resistance of APSL with large periods from NEMD simulations. Note that there are two kinds of interfaces in APSL NWs as depicted in Fig. 4.3, i.e., interfaces linked with C-C bonds, marked as a C-C interface type and interfaces linked with Si-Si bonds, marked as a Si-Si interface type. The measured Kapiza resistance  $R$  for the two interfaces are  $R_{C-C} = 4.7 \pm 0.4 \times 10^{-10} \text{ m}^2 \text{ K/W}$  and  $R_{Si-Si} = 3.6 \pm 0.4 \times 10^{-10} \text{ m}^2 \text{ K/W}$ , respectively. Considering the analogy between the thermal and the electrical resistance, the total thermal resistance equivalent to one period would be (Termentzidis et al. 2013)  $R_{tot} = R_{pris} + R_{Si-Si} + R_{C-C} = L_p/\kappa_{pris} + R_{Si-Si} + R_{C-C}$ , where  $R_{pris}$  and  $\kappa_{pris}$  refers to the thermal resistance and conductivity of pristine NW, respectively. Consequently, the thermal conductivity of the SLs  $\kappa_{SL}$  can be casted as,

$$\kappa_{SL} = \frac{L_p}{R_{tot}} = \frac{L_p}{L_p/\kappa_{pris} + R_{Si-Si} + R_{C-C}} \quad (4.1)$$

Substituting the obtained thermal conductivity of pristine NW and Kapiza resistance into Eq. 4.1, we can calculate the thermal conductivity for long period APSL NWs and the results are reported in Fig. 4.5(a) with triangles. The obtained thermal conductivities agree well with EMD simulation results.

### 4.3.3 Phonon Density of States Analysis

To check the vibrational properties of the interface atoms, vibrational density of state (VDOS) of three regions, i.e. the C-C interface region, the Si-Si interface region and the Si-C region far from both interfaces, which are highlighted in Fig. 4.2 with red boxes, has been calculated. In the three regions, atomic velocities of 4 atomic layers including 2 layers of Si and 2 layers of C atoms are recorded every 1.5 fs during 75 ps. The VDOS is then numerically computed by decomposing the time correlation function of the atomic velocities into the Fourier space as:

$$VDOS(\omega) = \frac{1}{k_B T} \sum_i m_i |v_i(\omega)|^2 \quad (4.2)$$

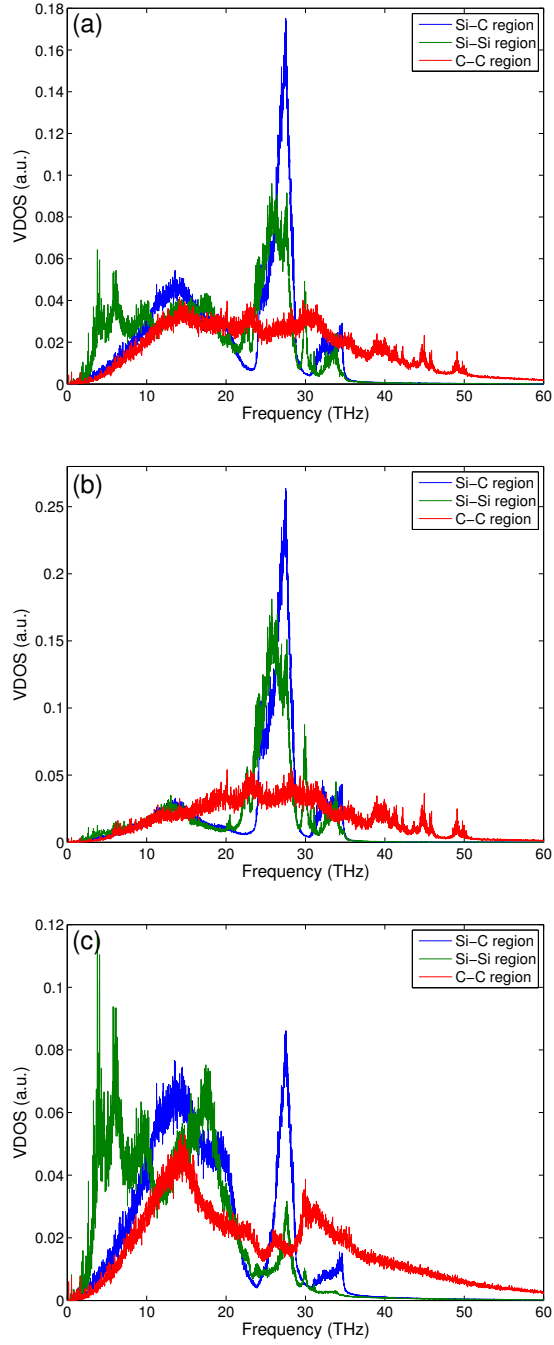
The total VDOS is presented in Fig. 4.7(a). As clearly shown, the VDOS of the two interface atoms are quite different from the atoms far from interfaces. For the Si-C region, the VDOS has a similar shape with that of bulk 3C SiC lattices, where it shows three typical peaks separated by two gaps. The three peaks correspond to the acoustic phonon modes, transverse optical phonon modes and longitudinal optical phonon modes. In the Si-Si interfaces, those three peaks remain while new properties also appear. Around 5 THz, two strong peaks emerged, which can be identified as Si atom vibrational modes as shown in the Si partial DOS depicted in Fig. 4.7(c). These new peaks are also observed in the diameter modulated SiC NWs interfaces (Termentzidis et al. 2013). Besides the low frequencies peaks, new modes are also observed in the two gaps around 22 THz and 30 THz. These new gap modes are produced by the C atom vibrations, shown clearly in Fig. 4.7(b). In the C-C bonding interface regions, the VDOS changed remarkably compared to the one in the Si-C region. The main feature of the VDOS is that it shows a long tail above the cut off frequency of 35 THz, which is due to the much stiffer C-C interactions.

To check the interaction between different types of bonds, the two body potential energy which is the main part of the total potential energy, as well as the second derivative of the two body potential (force constant) as a function of the inter-atomic distance are plotted in Fig. 4.8. Since the equilibrium position is in the range  $r_{ij} < R - D$ , where  $r_{ij}$  is the inter-atomic distance and  $R$  and  $D$  are parameters listed in table 4.1, we only plot the potential energy and force constant functions in the range  $r_{ij} < R - D$ . In this range, the potential energy  $V_{ij}$  between a pair atoms is written as:

$$V_{ij} = A \exp(-\lambda_1 r_{ij}) - B \exp(-\lambda_2 r_{ij}) \quad (4.3)$$

as a result, the force constant  $FC_{ij}$  between a pair is deduced as follows:

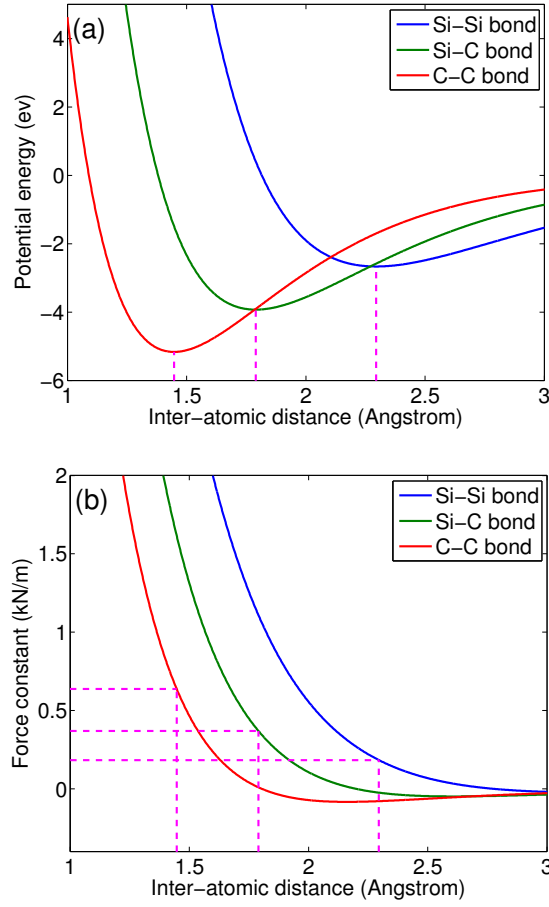
$$FC_{ij} = A\lambda_1^2 \exp(-\lambda_1 r_{ij}) - B\lambda_2^2 \exp(-\lambda_2 r_{ij}) \quad (4.4)$$



**Figure 4.7:** *Vibrational density of states obtained with Eq. 4.2 for the Si-C region, the Si-Si region and the C-C region with period  $L_p = 18.1$  nm. (a), total VDOS in the three regions; (b), VDOS projected on C atoms in the three regions; (c), VDOS projected on Si atoms in the three regions.*

**Table 4.1:** List of the Tersoff two body potential parameters used in Eq. 4.3 and 4.4.

	A	B	$\lambda_1$	$\lambda_2$	R	D
Si-Si	1830.8	471.18	2.4799	1.7322	2.85	0.15
Si-C	1597.3	395.15	2.9839	1.9721	2.3573	0.1527
C-C	1393.6	346.74	3.4879	2.2119	1.95	0.15



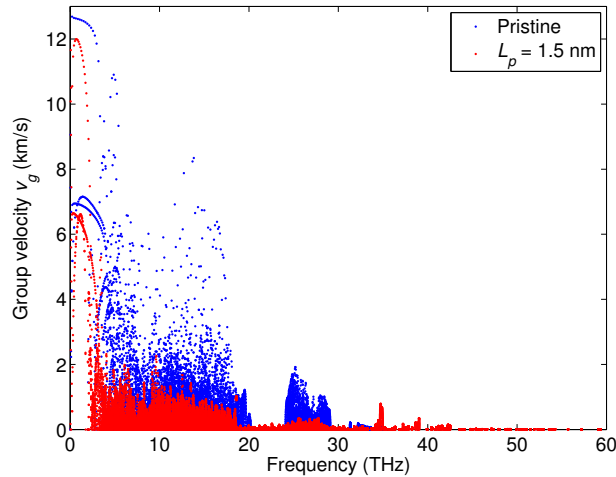
**Figure 4.8:** Inter-atomic potential energies (a) and force constants given by the second derivative of the corresponding potential energies (b) as a function of the inter-atomic distance described by eq. 4.3 and 4.4, respectively. The equilibrium positions obtained from the potential energy minimum are indicated with the dashed lines. The parameters used for this plot is listed in table 4.1. Note that this plot is only valid in the range  $r_{ij} < R - D$ .

Fig. 4.8 depicts the inter-atomic potential energy and force constant for the three types of bonds described with Eq. 4.3 and 4.4, respectively. The equilibrium inter-atomic distance (potential energy minimum) of the three types of bonds follows  $r_{si-si} > r_{si-c} > r_{c-c}$  (Fig. 4.8(a)). The corresponding force con-

starts around their equilibrium position indicated by the dashed lines in Fig. 4.8(b) follow the relationship  $F_{si-si} < F_{si-c} < F_{c-c}$ . A quantitative calculation on the second derivative of the two body part potential around the equilibrium position provides a force constant  $K = 387$  N/m for the Si-C bond, which is almost half of the C-C bond value of 664 N/m. This strong coupling makes the vibration of both Si and C atoms complex and shows long tails above the usual cut off frequency (Fig. 4.7(b) and 4.7(c)). However, those high frequency modes are localized on the C-C bond interface atoms and do not carry heat. This can be identified from the VDOS of atoms located next to the C-C interface regions (not shown), showing that the long tail is suppressed dramatically and almost has the same cut off as that of the Si-C region. The localization of high frequency modes is also supported by group velocity calculations (Fig. 4.8), where almost zero group velocity is obtained for the modes above 35 THz. Compared with the C-C region, the VDOS of the Si-Si region matches more with the VDOS in the Si-C region. This explains the lower Kapiza resistance in the Si-Si interface than in the C-C one.

#### 4.3.4 Phonon Group Velocity Analysis

To elucidate the origin of the thermal conductivity decrease of APSL NWs compared to the one of pristine NWs, the phonon group velocity  $v_g$  for pristine NW and APSL NW with  $L_p = 1.5$  nm is calculated based on lattice dynamics as follows (Zhao and Freund 2005),



**Figure 4.9:** Phonon group velocity  $v_g$  calculated with Eq. 4.5 of a pristine NW and an APSL NW with  $L_p = 1.5$  nm. The diameter is chosen as  $D = 2$  nm in order to reduce the number of atoms in the unit cell.

$$v_g = \frac{\partial \omega}{\partial k} = - \frac{\text{Im}[a\lambda u^H D_R u]}{\omega |u|^2} \quad (4.5)$$

where  $\lambda = \exp(ika)$ ,  $k$  and  $a$  are the wave vector and the unit cell length.  $D_R$  denotes the mass normalized coupling force constant matrix between neighbouring unit cells. The superscript  $H$  means conjugate transpose.  $\omega - u$  are frequency - eigenvector pairs, which are obtained by solving the atomic equation of motion  $D(k)u = \omega^2 u$  with  $D(k)$  being the atomic mass normalized dynamic matrix.

The phonon group velocities variations with frequency for pristine and APSL NWs having a period length  $L_p = 1.5$  nm and a diameter  $D = 2$  nm, are depicted in Fig. 4.9. This latter figure demonstrates that the APSL NW group velocity is dramatically decreased compared to that of pristine NWs. This trend is especially clear in the frequency range of 3 THz to 10 THz, where these phonons carry most of the heat in pristine NW. The averaged phonon group velocity of APSL is only 30% to 50% of the value of pristine NWs in this frequency range. The strong decrease of group velocity finally leads to the significant thermal conductivity reduction in APSL NWs. We also note that the group velocity above 35 THz is almost zero, indicating that these frequency modes do not contribute to heat transfer. This also support the argument that the high frequency modes above the cut off frequency of bulk SiC only localizes on the C-C interfacial region.

To summarize, the thermal conductivity of a new type of superlattice - APSL NWs - has been simulated with equilibrium molecular dynamics. A minimal thermal conductivity is found for a period of about 6 nm due to the interplay between phonon wave effect and phonon particle effect. Thermal conductivity of period modulated APSL NWs is largely suppressed compared to that of pristine NWs. The maximum conductivity reduction can be as high as 52% at 300 K while increasing the temperature reduces the suppression percentage. Due to the formation of new Si-Si bonds and C-C bonds on interfaces, new vibrational states are observed for interface atoms. The origin of the large thermal conductivity reduction is investigated by the phonon group velocity calculation. This analysis shows that phonon group velocity is greatly decreased for APSL NWs compared to that of pristine NWs. The significant reduction of thermal conductivity of SiC NWs may help to improve the thermoelectric performance of SiC, where the high thermal conductivity is the main hurdle for increasing the figure of merit.

## 4.4 Conclusions

In this chapter, experimental measurements of SiC thermoelectric properties have been specially introduced. The measured values indicate that the thermoelectric figure of merit of SiC is not optimum due to its high thermal conductivity. Moreover, the experimental synthesis of locally distributed anti-phase boundary domains as well as the impact of anti-phase boundaries on electrical properties are reviewed. Based on these experimental findings, we proposed a new type of superlattice, i.e., the anti-phase superlattice, with potential thermoelectric conversion efficiency. We simulated heat transfer properties in the SiC APSL NWs with equilibrium molecular dynamics. The period length and temperature have been chosen as variables to tune the thermal conductivity of superlattice NWs. It was found that the thermal conductivity of the period modulated APSL NWs can be suppressed noticeably when compared to that of the pristine one. The maximum reduction can be as high as 52% at 300 K. This minimal value corresponds only to 2.6% of the bulk SiC value at 300 K (Samolyuk et al. 2011). This means that the thermal conductivity of SiC can be reduced twofold with the combination of APSL and NW effects, which is beneficial for thermoelectric performance. The origin of the large thermal conductivity reduction is investigated with phonon group velocity calculations. The analysis shows that phonon group velocity is greatly decreased for APSL NWs compared to that of the pristine NW. Besides, a minimal thermal conductivity was found for a period of about 6 nm. By means of non-equilibrium molecular dynamics simulations, we show that this minimal thermal conductivity originates from the interplay between phonon wave effect and phonon particle effect. Since new Si-Si bonds and C-C bonds are formed on interfaces, we studied the vibrational density of states in both interface regions and the region far from interfaces. Phonon density of states reveals that new vibrational states appear for interface atoms. In the Si-Si interfaces, two strong peaks emerge around 5 THz, which are identified as Si atom vibrational modes. Besides the low frequency peaks, two gap modes around 22 THz and 30 THz are also observed due to the C atom vibrations. Because of the stiff C-C interactions, the VDOS in the C-C bonding interface regions shows a long tail above the usual cut off frequency of 35 THz. The current study shows that SiC APSL NWs may serve as a new candidate to improve the thermoelectric performance of SiC, where the high thermal conductivity is the main hurdle for increasing the figure of merit.



## Chapter 5

# Geometrical Defects in Nanowires: Minimum Thermal Conductivity in Si Twinning Superlattice Nanowires

Using Non-equilibrium Molecular Dynamic simulations, the thermal conductivity of Si phononic metamaterial nanowires with twinning boundaries distributed periodically along the nanowire has been investigated in this chapter. We first show that this latter structural modulation can yield 65% thermal conductivity reduction compared to the straight wire case at room temperature. Secondly, a purely geometry-induced minimal thermal conductivity of the phononic metamaterial is observed at a specific period depending on the nanowire diameter. Mode analysis reveals that the minimal thermal conductivity arises due to the disappearance of favored atom polarization directions. The loss of a single polarization direction yields a suppression of phonon group velocity in a large extent, which directly reduces the thermal conductivity. The current thermal conductivity reduction mechanism collaborates with the other known reduction mechanisms, such as the one related with coating, to further reduce the thermal conductivity of the metamaterial. The current studies reveal that the twinning superlattice phononic metamaterial nanowire is a promising candidate for efficient thermoelectric conversion benefited from the large suppression in thermal transport without deterioration of electron transport properties.

### 5.1 Introduction

Thermoelectric material, which can convert heat to electric power and vice versa, is one of the promising candidates for energy harvesting. The dimensionless figure of merit  $ZT$ , measuring the conversion efficiency, depends on the electrical conductivity, the Seebeck coefficient and the thermal conductivity.

ity ( $\kappa$ ). Due to its abundance in nature, to the sum of knowledge accumulated on its properties and also to its environment friendly features, silicon has been extensively studied as a thermoelectric material and  $ZT = 1$  was achieved for Si nanowires (NWs) (Hochbaum et al. 2008), a remarkable accomplishment in view of the poor thermoelectric conversion potential of the bulk counterpart. This significant progress in figure of merit for Si is largely attributed to the remarkable reduction in thermal conductivity of Si NWs. Both experimental (Hochbaum et al. 2008; Boukai et al. 2008; Li et al. 2003; Bux et al. 2009; Chen et al. 2013) and theoretical (He and Galli 2012; Hu and Poulikakos 2012; Volz and Chen 1999; Jiang et al. 2013; Chen et al. 2010; Xiong et al. 2014; Volz and Lemonnier 2000; Kazan et al. 2010) works show that with the introduction of defects, such as surface roughness, heterogeneous coating, the thermal conductivity of Si NWs can be two orders of magnitude smaller than that of the crystalline bulk one. Although this significant achievement has been reached, it is still far from the desired efficiency of solid state thermoelectric devices, where  $ZT \sim 4$  is required (T. M. Tritt 2011). Consequently, new mechanisms for  $\kappa$  reduction are greatly needed to reach the next milestone of Si thermoelectrics.

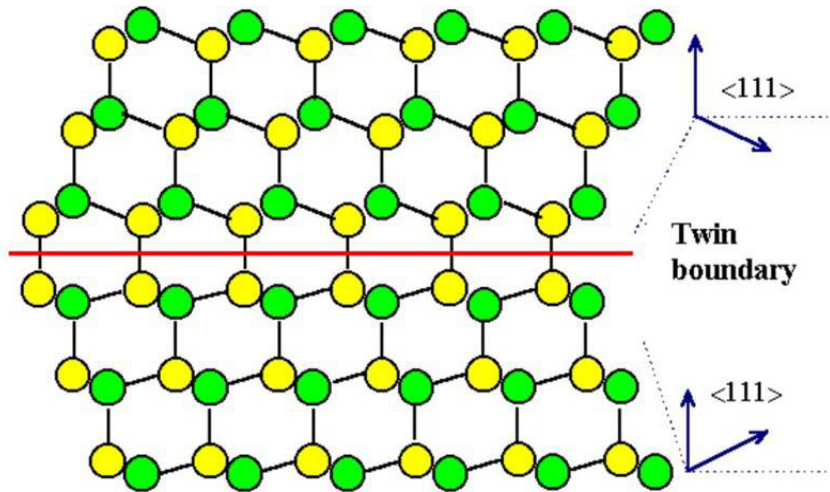


**Figure 5.1:** Schematic of a twin boundary in a diamond lattice. The twin boundary is indicated with the red line and the lattices on the two sides of the twin boundary are mirror-symmetric. Figure from [http://www.tf.uni-kiel.de/matwis/amat/def\\_en/kap\\_7/backbone/r7\\_1\\_1.html](http://www.tf.uni-kiel.de/matwis/amat/def_en/kap_7/backbone/r7_1_1.html)

Twinning, also known as the planar stacking fault, is one of the most important defects in materials science and it is most often related to mechanical properties (Wang and Huang 2006; Lin et al. 2010). A twin boundary can be obtained by stacking in a mirror-symmetry way compared to a previous stacking order (Fig. 5.1). To stack in this mirror-symmetric way, we obtain the structure

without changing any bond lengths or bond angles. This indicates that a twin boundary is coherent and has a smaller formation energy compared to other grain boundaries.

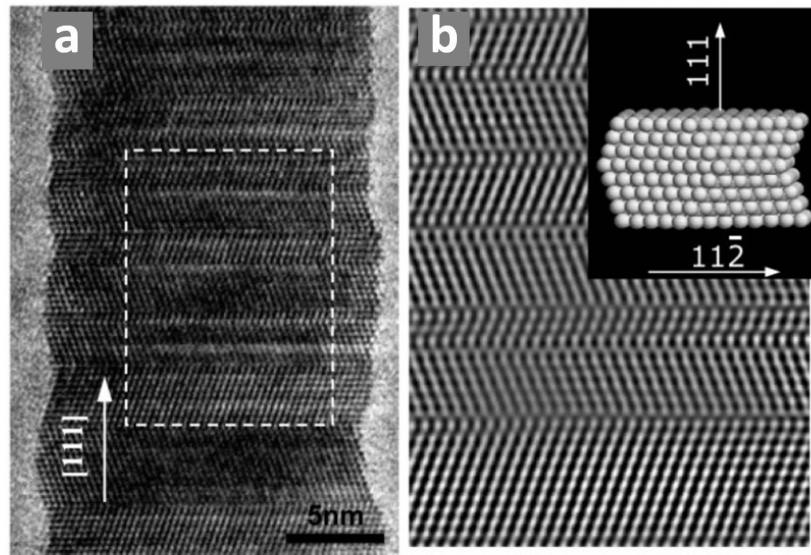


**Figure 5.2:** (a) High resolution TEM image of a InP twinning SL nanowire. Long-range superlattice periodicity can be clearly identified. (b) Fourier-filtered high resolution TEM image of the twinning SL in the dashed line box shown in (a). The inset is a space-filling model of the twinning boundary. Figure from Xiong et al Nano Lett. 2006, 6: 2736-2742.

Recent experiments (Lopez et al. 2009; Algra et al. 2008; Xiong et al. 2006; Wang et al. 2008) show that twin planes are commonly found in NWs with FCC structures grown in the  $\langle 111 \rangle$  direction, e.g., InP, SiC, GaP, Si etc. These twin planes are distributed periodically along the NWs and form a twinning SL metamaterial NW. The diameter and period length of this metamaterial NWs can be controlled during the synthesis process, offering the degree of freedoms for tuning their properties. More interestingly, NWs with twinning SLs feature a zigzag arrangement of periodically twinned segments with a rather uniform thickness along the entire growth length, offering a new mechanism for shape controlling during the growth of NWs (Fig. 5.2). The impact of twinning on mechanical (Wang and Huang 2006; Lin et al. 2010), electronic (Ikonić et al. 1993; Ikonic et al. 1995), as well as on optical properties (Ikonic et al. 1995) has been widely studied while this impact remains unexplored concerning thermal properties. Unlike heterostructure SLs with fundamental A and B units, where the units A and B differ either in local crystalline structure or local composition or both, the units A and B of a twinning SL exhibit the same local structure and composition and they differ only by a relative rotation of

the crystal orientation, i.e., A and B are "twins" (Xiong et al. 2006). As a result, the conventional mechanisms for SL interface scattering, such as mass mismatch and lattice mismatch, are not applicable and new phonon scattering mechanisms taking place in twinning SLs should be investigated.

In this work, we perform nonequilibrium molecular dynamics (NEMD) simulations to calculate the thermal conductivity of the Si metamaterial NWs with twinning SLs. We show that the thermal conductivity of the twinning SL NWs can be remarkably reduced up to 65% at room temperature compared to their pristine counterpart. A minimum thermal conductivity due to the geometric effect is found with a specific SL period, which equals to 1/3 of the diameter.

## 5.2 Structure and Simulation details

Fig. 5.3 depicts the structure formation of the twinning SL with the diameter  $D$  and period  $L_p$ . For a close-packing structure, there are usually three types of stacking sites with exactly the same configuration but having a shift one from another in a specific direction. The three stacking sites are usually labelled as A, B, and C. The B and C sites can be obtained from the A site with a shift of  $(1 + 3n)b_v$  and  $(2 + 3n)b_v$ , respectively, where  $b_v$  is the minimum shift length as shown in Fig. 5.3(a) and  $n$  is an integer. The stacking sequence of ABCABC in the  $\langle 111 \rangle$  direction forms the FCC structure and the ABABAB one forms the HCP structure. For Si having a FCC diamond lattice, the shift between different sites is along the  $\langle 112 \rangle$  crystal orientation with  $b_v = 2.217 \text{ \AA}$ . The cross section of the wire is chosen as hexagonal with the diameter  $D$ , which is shown in Fig. 5.3(b). The wire firstly grows according to a FCC structure, i.e., following a stacking in the ABCABC sequence with the same shift given by the vector  $b_v$  between the neighboring layers. After several ABC periods, a stacking fault is introduced, instead of stacking a A layer, a B layer is directly introduced after the C layer with a shift of  $b_v$  in the opposite direction. After the stacking fault, the stacking sequence changes to CBACBA, which is purely symmetrical to the previous stacking as is shown in Fig. 5.3(c). As a result, a kink is formed with the angle  $\theta = 109.4^\circ$ .

NEMD simulations are performed by using LAMMPS software (Plimpton 1995) with the commonly adopted Stillinger-Weber potential (Stillinger and Weber 1985; Ding and Andersen 1986) describing the interactions between atoms. The velocity Verlet algorithm with an integration time step of 0.8 fs is used to solve the equations of motion. All the structures are fully relaxed at zero pressure and at target temperatures (NPT) for 4 ns and then moved to NVE ensemble with fixed boundary conditions on the two ends atomic layers. Next to those fixed layers, with the help of the Nosé-Hoover thermostat (Nosé 1984; Hoover 1985), several layers of atoms were coupled to hot and cold baths having temperatures

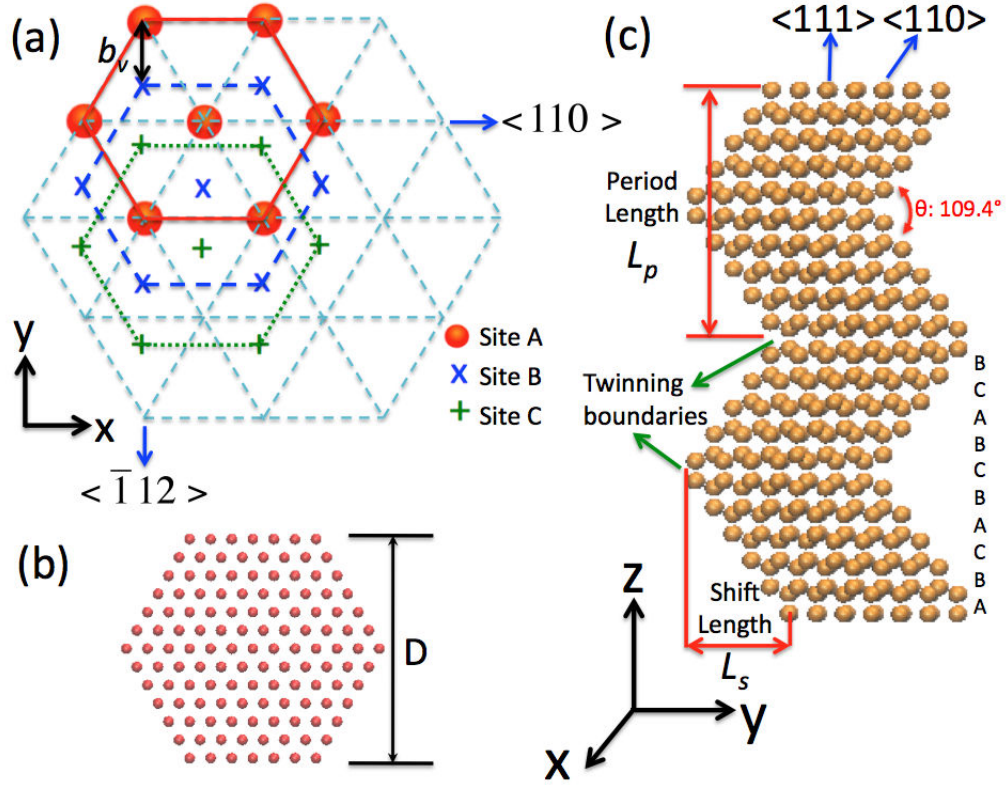


**Figure 5.3:** Schematic figure of the twinning SL phononic metamaterial stacking with diameter  $D$  and period length  $L_p$ . (a) three possible stacking sites labelled with A, B, and C in closely packed structures. The three sites are identical but are shifted in the  $\langle 112 \rangle$  direction one from another; (b) example of hexagon cross section with the diameter  $D$  of the twinning SL NWs; (c) stacking sequence of a Si twinning SL NW.

$T_0 + \Delta/2$  and  $T_0 - \Delta/2$ , respectively, where  $\Delta = 20$  K in all simulations. 5 ns runs were performed to reach non-equilibrium steady state, and another 5 ns to time-average the local temperature  $T$  and the microscopic heat flux  $j$  along the  $z$  direction. The thermal conductivities  $\kappa$  were then extracted from the Fourier's law, i.e.,  $\kappa = j(dT/dz)^{-1}$ . All the NWs thermal conductivities were measured with the same kink leg length of 34.5 nm.

## 5.3 Thermal Conductivity Analysis of Twinning SL NWs

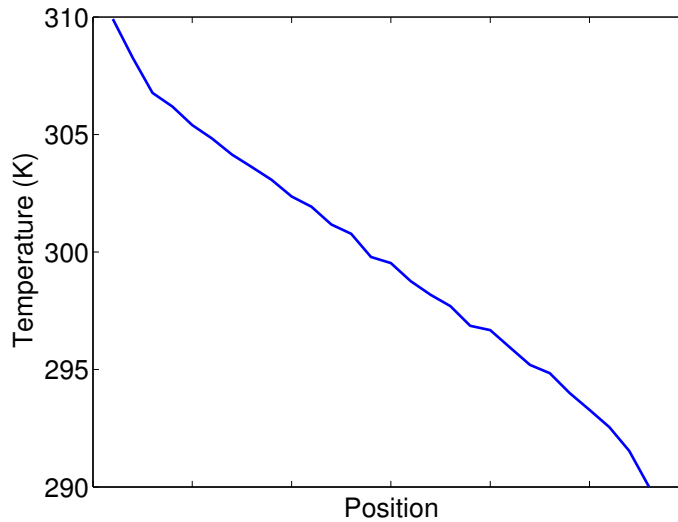
### 5.3.1 Thermal Conductivity

Fig. 5.5(a) represents the thermal conductivities of the Si twinning SL NWs as a function of period  $L_p$  and specified diameter  $D$  at 300 K. The thermal conductivities of the pristine NWs having the same diameters and lengths are

also calculated and summarized in table 5.1. Note that the length dependent thermal conductivity in nanostructures has been extensively reported (Hu and Poulikakos 2012; Chang et al. 2008; Yang et al. 2010). In this study, we focus on the relative reduction of thermal conductivity by the twinning rather than the absolute value or on the length effect on thermal conductivity. As a result, we fix the length of the simulated NWs to 34.5 nm and consider thermal conductivity as a function of SL period, temperature, and diameter of NWs.

**Table 5.1:** Thermal conductivities of pristine NWs and twinning SL phononic metamaterial NWs with different diameters at 300 K. The resulting reductions in percentage are reported in the last line.

Diameter (nm)	2	4	6	8	10
Pristine NW $\kappa$ (W/m·K)	$18.4 \pm 0.15$	$19.4 \pm 0.17$	$21.0 \pm 0.10$	$22.7 \pm 0.08$	$24.5 \pm 0.11$
SL Minimum $\kappa$ (W/m·K)	$6.5 \pm 0.22$	$7.7 \pm 0.20$	$9.9 \pm 0.15$	$11.3 \pm 0.10$	$12.5 \pm 0.12$
Maximum reduction (%)	64.7	60.3	53.0	50.0	49.0



**Figure 5.4:** Temperature profile of the twinning SL phononic metamaterial NW with period  $L_p = 5$  nm and diameter  $D = 4$  nm.

As shown in Fig. 5.5(a), the thermal conductivities of the NWs with twinning SL are largely decreased compared to the one of the pristine NW. A first guess regarding the thermal conductivity reduction may arise from two reasons, i.e., the zigzag geometric effect and the twinning boundary scattering. To check the

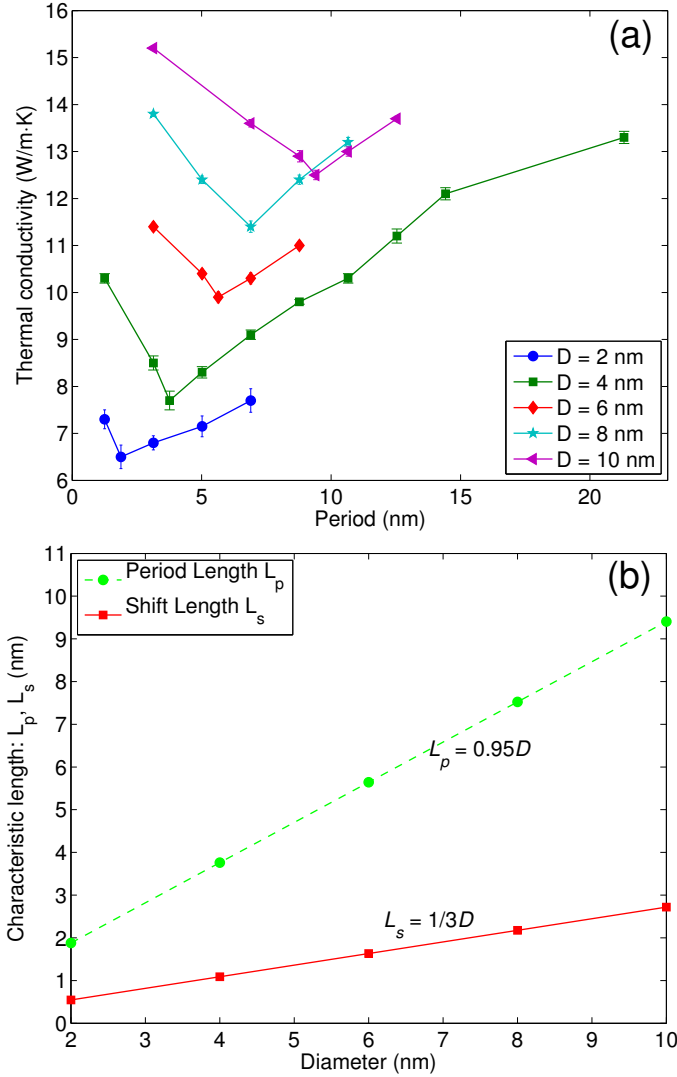


**Figure 5.5:** (a) Thermal conductivities of the twinning SL phononic metamaterial NWs as a function of the period for different diameters at 300 K. A minimum thermal conductivity appears at different period lengths for different diameters. (b) Period length  $L_P$  and shift length  $L_s$  corresponding to the minimum thermal conductivity versus the diameter.  $L_P$  and  $L_s$  are linked together with the relation  $L_s = L_p/2 \times \sin(\theta/2)$

relative contribution of these two aspects, we calculated the thermal conductivities of the bulk Si twinning SLs by applying periodic boundary conditions in the x and y directions and compared them with the one of the silicon bulk material. With the periodic boundary condition in the x and y directions, the geometric effect is eliminated and we can purely focus on the scattering by the twinning boundaries. Surprisingly, regardless of the number of boundaries, the

results show nothing difference with the value of the perfect bulk, indicating no impact on heat transfer from the twinning boundaries. All the thermal conductivity reduction in the SL NWs hence arises from the induced geometric effect, i.e., the zigzag configuration. This can actually be observed directly from the temperature profile (Fig. 5.4) for both bulk materials and nanowire SLs, where no temperature jump is observable around the twinning boundaries. The reason may be found from the fact that each atomic layer is actually identical and the stacking sequence of ABCABC and ABCACB does not alter any bond lengths or bond angles. Consequently, the force between the neighboring layers will not change and the atomic motion can be effectively transferred through the twinning boundaries.

When the diameter remains invariant, the increase in SL period leads the thermal conductivity to decrease first, reaching a minimum value, and then progressively to an increase. The minimum thermal conductivity observed here seems similar to that observed in the heterostructure SLs (Hyldgaard and Mahan 1997; Simkin and Mahan 2000; Koh et al. 2009; Lee and Venkatasubramanian 2008). However, the mechanism taking place in the twinning SL phononic metamaterial NWs completely differs from the one observed in heterostructure SL. In this latter situation, the minimum thermal conductivity is attributed to the interplay between the phonon coherence and the interface scattering. For the twinning SL NWs, the twinning boundary has no impact on heat transfer and thermal conductivity change is fully ascribed to the twinning induced zigzag geometric effect as we discussed. This can be further confirmed from the diameter dependent SL periods corresponding to the minimum thermal conductivities as displayed in Fig. 5.5(b). This figure clearly shows that the period length of minimal thermal conductivity varies with the diameter according to the relationship  $L_p = 0.95D$ . In Fig. 5.3(c), we also defined the shift length  $L_s$ , representing the total length shift in the kink direction within one period.  $L_p$  and  $L_s$  are linked with a simple relation, i.e.,  $L_s = L_p/2 \times \sin(\theta/2)$  with  $\theta = 109.4^\circ$ . As a result, the  $L_s$  value corresponding to the minimum thermal conductivity is a function of the diameter and can be simply expressed as  $L_s = D/3$ , which is also shown in Fig. 5.5(b). It has been experimentally demonstrated that the twinning boundary has almost no effect on the electrical conductivity in both bulk (Lu et al. 2004) and nanowire (Zhong et al. 2009) cases. As a result, the thermoelectric figure of merit of Si can be notably enhanced with the twinning SL phononic metamaterial NWs thanks to the significant thermal conductivity decrease without deterioration of electron transport properties.

### 5.3.2 Phonon Polarization Analysis

To explain the large thermal conductivity decrease as well as the minimal thermal conductivities, we performed the normal mode polarization calculations. For a given mode  $\lambda$ , the  $\alpha$  (x, y, or z) cartesian component of a unit polarization vector  $e_{i\alpha,\lambda}$ , of an atom  $i$  is defined as (Schelling and Phillpot 2001)

$$e_{i\alpha,\lambda} = \frac{\varepsilon_{i\alpha,\lambda}}{\sum_{\alpha} \varepsilon_{i\alpha,\lambda}^* \varepsilon_{i\alpha,\lambda}} \quad (5.1)$$

The normal mode eigenvectors components  $\varepsilon_{i\alpha,\lambda}$  and their corresponding eigenfrequencies  $\omega_{\lambda}$  are obtained by solving the lattice dynamical equation.

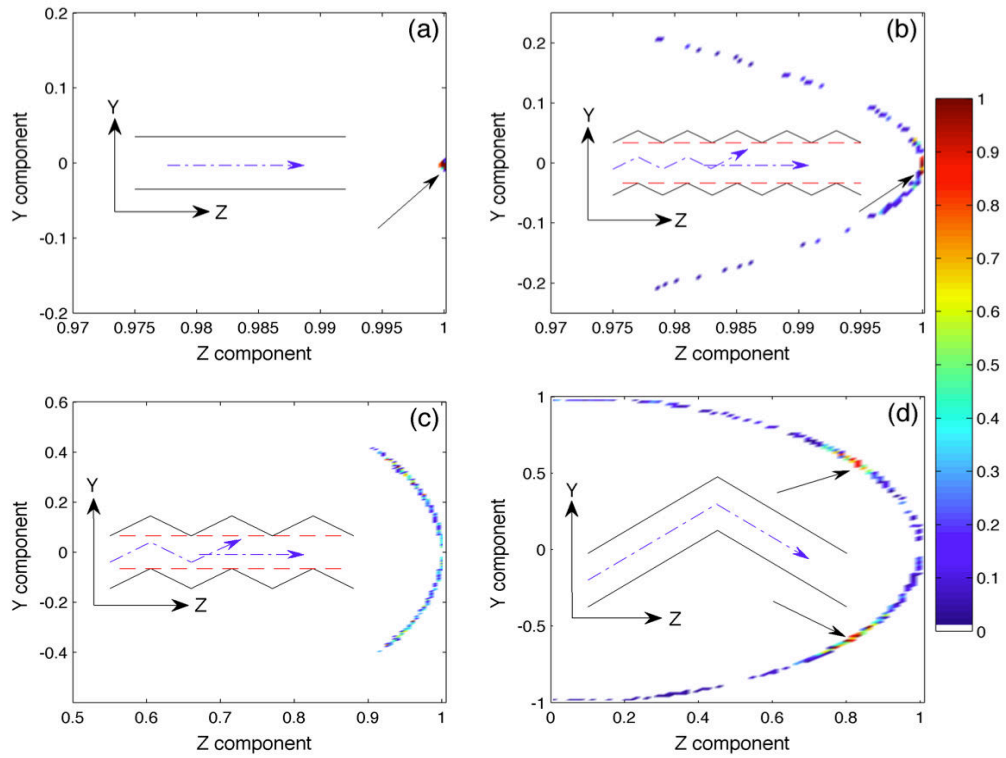


**Figure 5.6:** *Y-Z components of the LA mode vectors around the frequency  $4.0 \text{ cm}^{-1}$  for (a) the straight, (b)  $L_p = 1.25 \text{ nm}$ , (c)  $L_p = 1.9 \text{ nm}$ , and (d)  $L_p = 10.6 \text{ nm}$  phononic metamaterial NWs with  $2 \text{ nm}$  in diameter. The color represents the number of modes and the maximum value has been normalized to 1. The corresponding structures are indicated in each panel.*

Fig. 5.6 depicts the longitudinal acoustic (LA) mode polarization vectors of each atom projected on the Y-Z plane for the straight and the twinning SL

phononic metamaterials with different periods. The polarization vectors are calculated for the NWs 2 nm in diameter and around the  $4.0 \text{ cm}^{-1}$  frequency. The corresponding structures are also shown in each panel. For the straight NW, the normal modes possess well defined polarization vectors, as indicated by the dashed arrow in Fig. 5.6(a), where all the atoms show a unit polarization vector component near 1 in the z direction and almost zero in the x and y directions. This indicates that all the atoms vibrate along the z direction. This is of course favorable for phonon transport. When the NW grows with twinning of small periods, the LA modes for some of the atoms start to have a small y component but still predominate in the z direction as indicated by the arrow in Fig. 5.6(b). Those atoms with small y component are typically the atoms around the kinks.

When the SL period increases to the length corresponding to the minimum thermal conductivity (Fig. 5.6(c)), the polarization vectors significantly broaden in the y direction and no clear preferential orientation appears. The polarization vectors homogeneously distributed on the arc ranging from -0.4 to 0.4 in the y direction and from 0.91 to 1 in the z direction. This means the atomic vibrations are not coherent, hence, the phonon transport is hindered and results the decrease of the thermal conductivity compared to shorter period cases. With further elongation of the period, the atomic polarization vectors continue to broaden in the y direction with a small fraction of interchanges between LA modes and TA modes indicated by the y component near to the unity. This outcome agrees with the findings of Jiang et al (Jiang et al. 2013). However, two preferred orientations of the polarization vectors can be clearly observed in Fig. 5.6(d), which for sure will increase the thermal conductivity compared to the homogeneously distributed cases. The two preferred orientations have their y and z components (y,z) around  $(\pm 0.52, 0.81)$ . It can be easily calculated that these two preferred directions are along the two legs of kink, respectively. It follows that most of the atoms vibrate along the two legs. It can be shown that the atoms having the two preferred directions are located in the middle of the legs. Those latter also contribute to 60% - 70% of the atom polarization vectors for the NWs with  $L_p = 10.6 \text{ nm}$ . This percentage increases with the increase of period length, which agrees well with the increase of thermal conductivities when period length is increased beyond the minimum thermal conductivity period.

Alternatively, the minimum thermal conductivities can be explained with a more intuitive geometric analysis. As shown in the structures of Fig. 5.6, phonons can propagate straightforwardly along the wire direction in the pristine NWs, leading to a thermal conductivity labelled as  $\kappa_s$ , which should be in proportional to the cross section area of the straight part. While for the twinning SL NWs with long periods, phonons have to go along the legs as shown by the dash dot arrow in Fig. 5.6(d) in order to propagate from one side to

the other side. This thermal conductivity is labelled as  $\kappa_b$ .  $\kappa_b$  should be in proportional to the period length and should saturate to  $\kappa_s$  when  $L_p$  is long enough. When the shift length  $L_s$  (defined in Fig. 5.3) is larger than the diameter,  $\kappa_s = 0$  and the thermal conductivity of the wire is only composed by the heat flux involved in  $\kappa_b$ . However, in the cases where  $L_s$  is smaller than the diameter, phonons can propagate in both ways as illustrated schematically by the arrows in Fig. 5.6(b) and (c), i.e.,  $\kappa = \kappa_s + \kappa_b$ . Starting from  $L_s = D$ , with the decrease of period,  $\kappa_b$  decreases and  $\kappa_s$  increases from zero since the cross section of the straight part (noted by the red lines) enlarges progressively from zero. So there is a competition between  $\kappa_b$  and  $\kappa_s$  with the variation of the period, which finally results the minimal thermal conductivity. This also interprets the diameter dependence of the minimum thermal conductivity as a function of period length. Therefore the geometrical-period-dependent thermal conductivity of twinning SLs enables the control of heat transport and thermoelectric conversion efficiency by changing only the geometric properties of such phononic metamaterials.

### 5.3.3 Phonon Dispersion and Transmission

To know more about the vibrational properties of the twinning SL phononic metamaterial NW, we investigated the dispersion relation and compared it with that of pristine NWs (Fig. 5.7). The dispersion of both pristine and twinned NWs contain 4 acoustic branches, namely one longitudinal, two transverse and one torsion polarization branches. All the other branches are optical modes. As the twinning SL NWs contains much more atoms in a period, its dispersion curve has much more branches. However, most of the branches are flat bands, giving smaller group velocities compared to the pristine structure. This is more clearly shown in the zoom-in plot in Fig. 5.7(c) and (d). Due to the band folding effect, the acoustic phonon cut off frequency is much smaller than that of pristine NW. More interestingly, the acoustic phonon frequency goes up to the optical phonon range, no band gap between acoustic and optical phonon branches is observed. While for the twinning SL phononic NW with  $L_p = 3.1$  nm, a small gap between the optical and acoustic branches appears, giving a phononic band gap effect. The small group velocity of the twinning SL phononic metamaterial NWs hinders heat transfer, which can be identified more intuitively from the transmission function in Fig. 5.8 obtained from the Green's function calculations.

As clearly shown in Fig. 5.8, the transmission function of the twinning SL NW with  $L_p = 3.1$  nm is much smaller than the value of the pristine NW although much more branches are contained in the twinning SL NWs, indicating a decrease of group velocity to a large extent. Especially for the phonons below 7 THz, the transmission is decreased by a factor of 3. Since the phonons in this

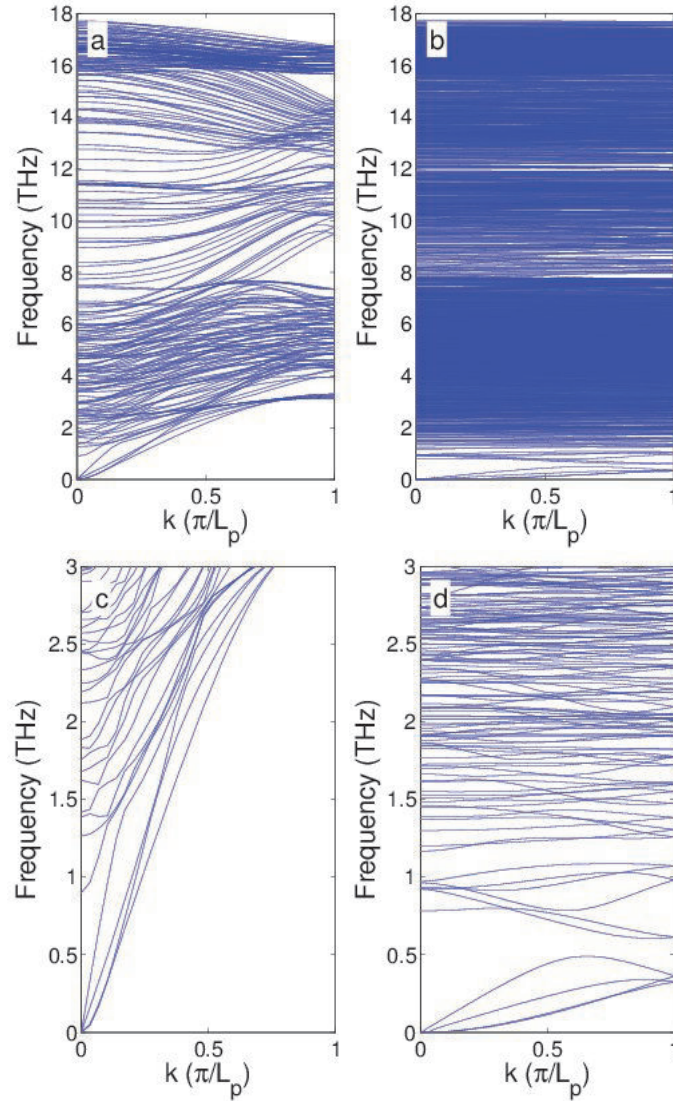


**Figure 5.7:** Phonon dispersion relation of the pristine NW with  $D = 2$  nm (a) and the twinning SL phononic metamaterial NW with  $L_p = 3.1$  nm,  $D = 2$  nm; (c) and (d) are corresponding zoomed in figures of (a) and (b), respectively.

frequency range carry most of the heat, the thermal transport in the twinning SL NWs is much hindered. The large group velocity suppression originates from the disappearance of a favored polarization direction and it is the immediate cause of thermal conductivity reduction. The transmission function also clearly shows the band gap between the acoustic and optical modes of the twinning SL NWs.

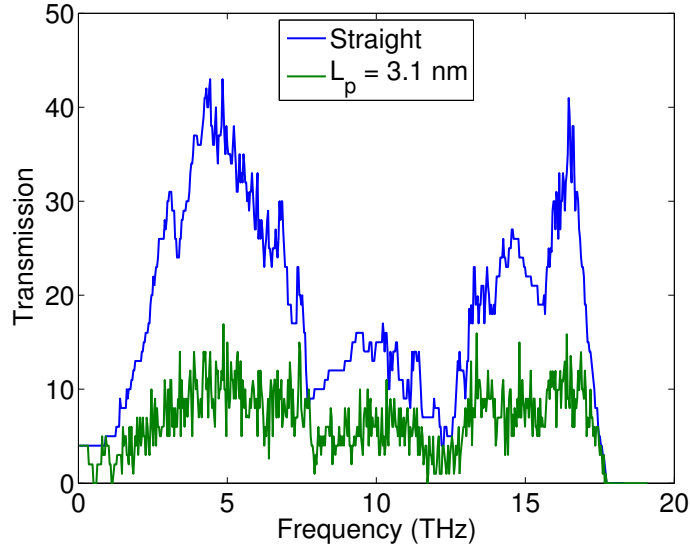


**Figure 5.8:** Phonon transmission functions calculated with the phonon Green's function vary with the frequency.

### 5.3.4 Temperature Dependent Thermal Conductivity

Fig. 5.9 illustrates the temperature dependent thermal conductivity of the pristine and twinning SL NWs with 4 nm and 34.5 nm in diameter and length, respectively. Due to the anharmonic effect, the thermal conductivity of the pristine NWs decreases quickly with the increase of temperature. While for the twinning SL NWs, the thermal conductivities only decrease slightly when the temperature increases from 300 K to 800 K, showing a weak dependence on temperature. This trend appears because the phonon mean free path in the twinning SL NWs is much smaller than in the pristine NWs and lead to weak temperature dependences for thermal conductivities in twinning SL NWs.

The phonon lifetime is commonly given by the Matheissen's rule, expressing the total inverse lifetime as the sum of the inverse lifetimes corresponding to each scattering mechanism. For the structures discussed here, only anharmonic and boundary scattering take place. Consequently, the total lifetime  $\tau$  can be casted as

$$1/\tau = 1/\tau_b + 1/\tau_a \quad (5.2)$$

where  $\tau_b$  and  $\tau_a$  are lifetimes of the boundary scattering and of the anharmonic scattering, respectively. The anharmonic scattering lifetime averaged over frequency can be approximated as (Asen-Palmer et al. 1997; Mingo 2003)

$$\tau_a^{-1} = BT e^{-C/T} \quad (5.3)$$

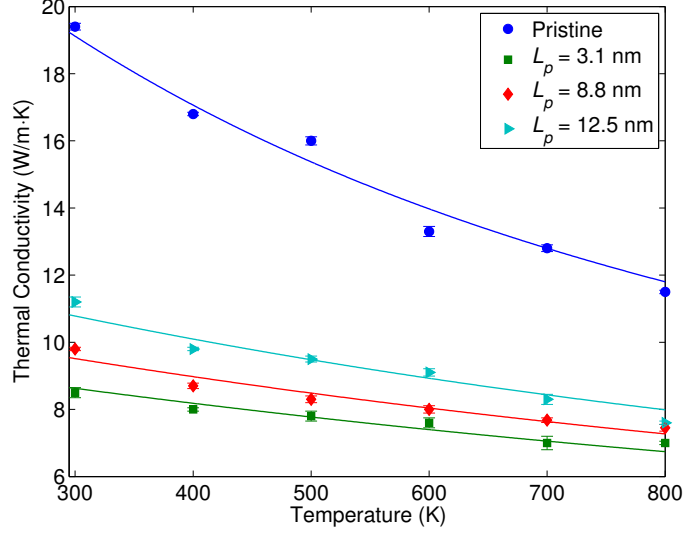


**Figure 5.9:** Temperature dependent thermal conductivity of the pristine and twinning SL phononic metamaterial NWs with different periods and a diameter of 4 nm. The corresponding solid lines are fitted with Eq. 5.5

with  $T$  being the absolute temperature,  $C = 137.3$  K and  $B$  are constants. Using the averaged specific heat capacity  $C_v$ , the group velocity  $v_g$  and the relaxation time,  $\kappa$  can be expressed as  $\kappa = C_v v_g^2 \tau$  for an one-dimensional wire. From this latter expression, it can be easily shown that

$$\kappa = C_v v_g^2 / (1/\tau_b + BT e^{-137.3/T}) \quad (5.4)$$

Let  $a = \frac{1}{C_v v_g^2 \tau_b}$  and  $b = \frac{B}{C_v v_g^2}$ . Considering  $a$  and  $b$  as fitting parameters, the following equation can be used to fit the temperature dependent thermal conductivities of different structures:

$$\kappa = \frac{1}{a + b T e^{-137.3/T}} \quad (5.5)$$

In Fig. 5.9, the corresponding solid lines are fitted with Eq. 5.5 with the fitting parameters  $a$  and  $b$  are summarized in table 5.2. The temperature dependent thermal conductivity  $\kappa$  for all structures can be well fitted with those parameters.

The parameter  $a$  related to the lifetime of the boundary scattering takes the values of 0.04, 0.08, 0.092, and 0.103 for the pristine and the twinning SLs corresponding to the periods 12.5 nm, 8.8 nm, and 3.1 nm, respectively. These values indicate a continuous decrease of the relaxation time due to boundary scattering for these structures. The parameter  $b$  takes the same value of  $6.7 \times 10^{-5}$  for all structures. This is because  $b$  characterizes the anharmonic effect,

**Table 5.2:** Summarize of the fitting parameters of  $a$  and  $b$  used in Eq. 5.5.

	$a$	$b$	$\tau_b/\tau_a$
Pristine	0.04		0.32
$L_p = 12.5$ nm	0.08	$6.7 \times 10^{-5}$	0.16
$L_p = 8.8$ nm	0.09		0.14
$L_p = 3.1$ nm	0.10		0.12

which only depends on the material properties. From the expression of  $a$  and  $b$ , one can derive the ratio between the boundary and the anharmonic relaxation time  $\tau_b/\tau_a$  as

$$\frac{\tau_b}{\tau_a} = \frac{b}{a} T e^{-C/T} \quad (5.6)$$

The ratios predicted by Eq. 5.6 at 300 K have also been summarized in table 5.2. The values are typically between 0.1 and 0.5, indicating that the boundary and the anharmonic mean free path have the following relationship (noting that the mean free path of anharmonic scattering is about hundreds of nanometers):

$$\Lambda_b > \frac{\Lambda_a}{10} > 10nm > D \quad (5.7)$$

In a purely diffusive boundary scattering case, the boundary mean free path should be the same as diameter. Contrarily in the current case,  $\Lambda_b$  is much larger than the diameter of the NWs, which means that the surfaces of the NWs are rather specular. This result indicates that the thermal conductivity can be further reduced by decreasing the surface specularly.

### 5.3.5 Coating Effects on Thermal Conductivity

To further reduce the thermal conductivity by decreasing the surface specularly, we coated Si twinning SL NWs ( $D = 4$  nm) with one- or two-Ge atom thick layers, forming the core-shell twinning SL phononic NWs. Mixed parameters for Si-Ge were based on the Stillinger-Weber potential according to references (Ding and Andersen 1986; Ethier and Lewis 1992).

The effect of the Ge atom coating on the thermal conductivities for the Si twinning SL phononic metamaterial NWs with different periods is illustrated in Fig. 5.10. As a comparison, the thermal conductivities of the Si twinning SL NWs without coating are also presented in the figure. Note that the diameters of the pure Si SL NWs and the Si-core in the core-shell structures are the same. As it can be seen from the figure, Ge coating still has a large impact on

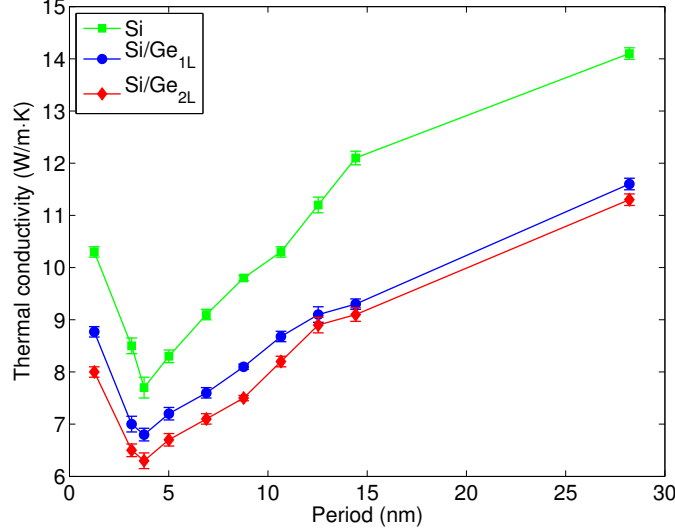


**Figure 5.10:** Thermal conductivity variation with the twinning SL period for the Si and the Si/Ge core/shell structures with one- and two-atom thick Ge atom layers.  $D = 4$  nm for the pure Si NWs and the Si core in the core/shell NWs.

the thermal conductivities of Si twinning SL NWs, especially for small periods. This is expected in terms of Ge coating can reduce the surface specularity and further shortens the phonon mean free path. With the Ge coating, the period corresponding to the minimum thermal conductivity does not change and the maximum reduction can reach almost 20% for only 2 atom layers of Ge coating. The thermal conductivity of the core-shell twinning SLs decreases with the increase of coating thickness at short periods while it almost does not change with coating thickness at large periods.

To summarize, the thermal conductivity of Si twinning SL phononic metamaterial NWs has been investigated with different periods, diameters as well as temperatures by using NEMD simulations. It is demonstrated that the thermal conductivity can be reduced by 65% at room temperature compared to the straight NW case. Pure geometry-induced induced minimal thermal conductivity of the phononic metamaterial is observed with the variation of the SL period. The corresponding periods are diameter dependent and almost equal to the diameter of the NW. A mode analysis shows that the minimal thermal conductivity is due to the loss of preferential orientation of the polarization vectors induced by the kink. The group velocity suppression produced by the loss of a single polarization direction is the key point of thermal conductivity reduction. The considered mechanism of geometry-induced reduction of thermal conductivity in twinning superlattice phononic metamaterials can be complemented by other known mechanisms to further reduce thermal conductivity in phononic metamaterials.

## 5.4 Conclusions

In this chapter, the recent progresses in the thermoelectric performance of Si based materials have been briefly reviewed. And we also introduced the experimental observations of the periodically distributed twinning boundaries along a NW, which forms a twinning SL NW. This type of SL has a novel zigzag geometry and it also offers the freedom in changing the diameter and period length, giving the flexibilities for phononic metamaterial design. Based on the experimental observations, we constructed NWs containing periodically distributed twinning boundary, i.e., twinning SL NWs, and calculated the thermal conductivities of those NWs using NEMD simulations. The comparison between the thermal conductivities of the pristine and twinning SL NWs shows that a large reduction up to 65% in thermal conductivity can be achieved at room temperature and the reduction is sensitive to temperature due to the anharmonic effect. When the period of the twinning SL NWs changes, a minimal thermal conductivity can be observed and the corresponding periods are diameter dependent and almost equal to the diameter of the NW. A mode analysis shows that the minimal thermal conductivity is purely due to the zigzag geometry. When the period is short, the phonon modes have a single polarization direction and they start to broaden when the period increases. When the period increases to a specific value, the favored phonon polarization direction totally disappears and becomes homogeneously distributed on an arc. By further increasing the period, two new favored polarization directions in the leg directions were observed. The appearance of the two new favored polarization directions promotes heat transfer compared to the one without any favored direction. Phonon dispersion reveals that the zigzag structure of twinning SL NWs results in a small group velocity, which is the immediate cause of thermal conductivity suppression. The phonon group velocity decrease is also revealed in phonon transmission spectra, where the transmission of the twinning SL NWs is much smaller than that of the pristine one. Moreover, a small phononic band gap between the acoustic and optical branches was observed in the twinning SL NWs. We also found that the considered mechanism of geometry-induced reduction of thermal conductivity in twinning superlattice can be complemented by other known mechanisms to further reduce thermal conductivity in phononic metamaterials. The current studies reveal that the twinning SL nanowire is a promising candidate for efficient thermoelectric conversion benefited from the large suppression in thermal transport without deterioration of electron transport properties.



## Chapter 6

# Void Defects in Nanowires: Transition from Heat Conduction to Radiation in Nanoscale Gaps

In this chapter, we introduce a special plane defect, i.e., vacuum, into a SiO<sub>2</sub> nanowire and arrange it periodically and perpendicular to the wire. This proposed structure allows us to study heat transfer between two clusters separated with a vacuum gap. Since heat transfer between two objects in direct contact is predominated by conduction while it is predominated by near field radiation when the two objects are separated with a vacuum gap, it is possible to study the fundamental transition between heat conduction and near field radiation when we alter the gap distance from zero (corresponding to contact) to several nanometers. By using the non-equilibrium Green's function method, we quantitatively investigate heat transfer between two silica clusters. In the gap range between 4 Å and three times the cluster size, the thermal conductance decreases as predicted by the surface charge-charge interaction. Above five times the cluster size, the volume dipole-dipole interaction predominates. Finally, when the distance becomes smaller than 4 Å, a quantum interaction where the electrons of both clusters are shared takes place. This quantum interaction leads to the dramatic increase of the thermal coupling between neighbor clusters due to strong interactions. This study finally provides a description of the transition between radiation and heat conduction in gaps smaller than a few nanometers.

### 6.1 Introduction

With the recent developments of nanotechnology, electronic devices continue to scale down in dimension and scale up in power density ([Cheng et al. 2011](#)). As

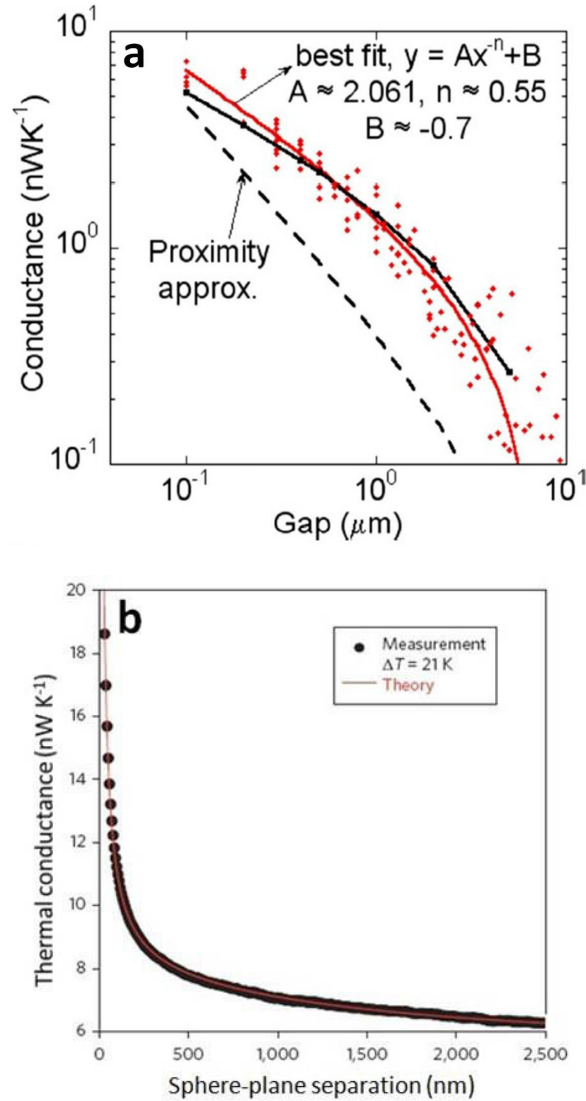


**Figure 6.1:** Near field heat transfer measurements. (a) experimental data (diamond points) from 13 heat transfer-distance measurements by Narayanaswamy. The dashed line is predicted by proximity approximation, which is far from the experimental data. This comparison indicates the break down of proximity approximation in describing near field radiation. (b) experimental measurement (solid circles) of thermal conductance between a sphere with diameter  $40 \mu\text{m}$  and a plate by Rousseau. The red line is the prediction with proximity approximation. the comparison clearly shows the perfect agreement between experimental data and theory predictions. Figure from Narayanaswamy et al *Phys. Rev. B* 2008, 78: 115303 and Rousseau et al *Nat. Photonics* 2009, 3: 514.

a result, near field radiation starts to play a notable role in the thermal design at nanoscales. Recently, it has been demonstrated both theoretically (Polder

and Van Hove 1971; Volokitin and Persson 2007; Joulain et al. 2005; Chapuis et al. 2008; Chapuis et al. 2008) and experimentally (Narayanaswamy et al. 2008; Shen et al. 2009; Emmanuel et al. 2009) that heat transfer through near field radiation between two parallel plates or between a sphere and a plane can be several orders of magnitude larger than the black body limit over a limited range of frequency. This clearly corroborates the fact that when the gap between two objects is smaller than the characteristic photon wavelength, a different physical behavior emerges in which near field radiation and acoustic phonon tunneling significantly contribute to heat transfer (Kosevich 1991; Prunnila and Meltaus 2010).

The first measurement of the radiative heat flux between two dielectric materials separated by a nanoscale gap distance has recently been performed by Narayanaswamy, Shen and Chen (Narayanaswamy et al. 2008; Shen et al. 2009) using a sensitive technique based on bimaterial cantilevers. Their experimental data show the breakdown of the Planck blackbody radiation law in the near field and also show that the proximity-force approximation is not valid for near-field radiation heat transfer in the range of gaps involved in their experiment. Shortly after, Rousseau et al. (Emmanuel et al. 2009) also measured the heat transfer in the near-field regime. Interestingly, and in contrast with Narayanaswamy's conclusions, these later results confirmed the proximity approximation. The main results of the measurements from these two groups are depicted in Fig. 6.1. The difficulty in performing such experiments makes it probable that heat transfer at the nanoscale will continue to be debated, as commented by Kittel (Achim 2009). Near-field radiation under the dipole/multipole approximation has been extensively investigated on a theoretical basis. Nonetheless, mechanisms taking place for separation distances shorter than 10 nm remain unclear. This range of separation distances may not be directly accessible by experiments due to the difficulty in fabricating well-defined planes and spheres at those scales. At the same time, as modern nanostructures might be smaller than 10 nm and are separated in some cases by only a few fractions of a nanometer, this range of lengths is of great interest to those who design nanoscale devices (Achim 2009; Ni et al. 2012). From a fundamental point of view, this domain is also involving the less understood transition from a classical charge-charge interaction, logically described as a radiation in the near-field, to a chemical bond interaction, yielding pure heat conduction.

By means of molecular dynamics simulations, Domingues et al (Domingues et al. 2005) found a interesting transition regime characterized by a thermal conductance larger than the contact conductance as shown in Fig. 6.2. But the largest value exceeded the upper physical limit. And the heat transfer behavior in long distance range can be well described with dipole-dipole approximations. Using ultra-high vacuum inelastic scanning tunneling microscopy, a previously

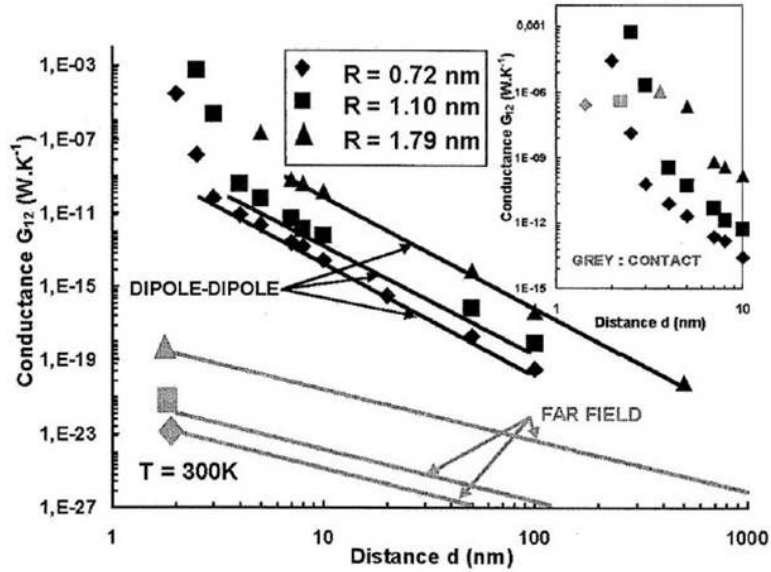


**Figure 6.2:** Thermal conductance between two silica clusters varies with the separation distance by means of molecular dynamics simulation. An interesting transition from heat conduction to radiation is observed. Figure from Domingues et al *Phys. Rev. Lett.* 2005, 94: 085901.

unknown mechanism of thermal transport—a field-induced phonon tunneling—has been reported by Altfeder et al (Altfeder et al. 2010). The thermal energy transmitted through atomically narrow vacuum gap exceeds, by ten orders of magnitude, the one of blackbody thermal radiation. In fact, before these experimental findings, Kosevich (Kosevich 1991) and Prunnila et al (Prunnila and Meltaus 2010) have modeled how acoustic phonons can directly tunnel through vacuum by introducing coupling mechanisms, and both of them have shown that acoustic phonons can travel through the vacuum gap with unitary transmission and thus can lead to significant thermal conductance and heat flux.

In this work, we estimate the heat transfer through a chain composed by identical non-contacting silica clusters by means of the phonon non-equilibrium Green's functions. We show that there are two critical vacuum gaps of about 4 Å and three to five times the cluster size. The first critical gap, of 4 Å, corresponds to a transition between the classical and the quantum regimes with strong interaction. Above this critical gap, the conductance decreases first according to a  $d^{-3}$  power law,  $d$  being the distance between the center of masses, and then gradually follows a  $d^{-6}$  power law, when the gap is larger than five times the cluster size. These power laws can be explained by classical surface charge-charge and volume dipole-dipole interactions, respectively. Below 4 Å, the conductance shows a much stronger dependence on gap thickness. The first critical gap is confirmed by *ab-initio* calculations showing that the electronic

wave functions indeed merge when the gap becomes shorter than 4 Å.

## 6.2 Structure and Simulation methods

We consider a system of identical silica clusters separated by a distance  $d$  between the cluster centers and a gap  $l$  (Fig. 6.3, top). It can also be regarded as inserting vacuum gaps perpendicular to a nanowire periodically. Clusters are coupled through the van Beest, Kramer, and van Santen (BKS) potential (van Beest et al. 1990), composed of Coulomb and Buckingham potentials. The mathematical form of the BKS potential reads as

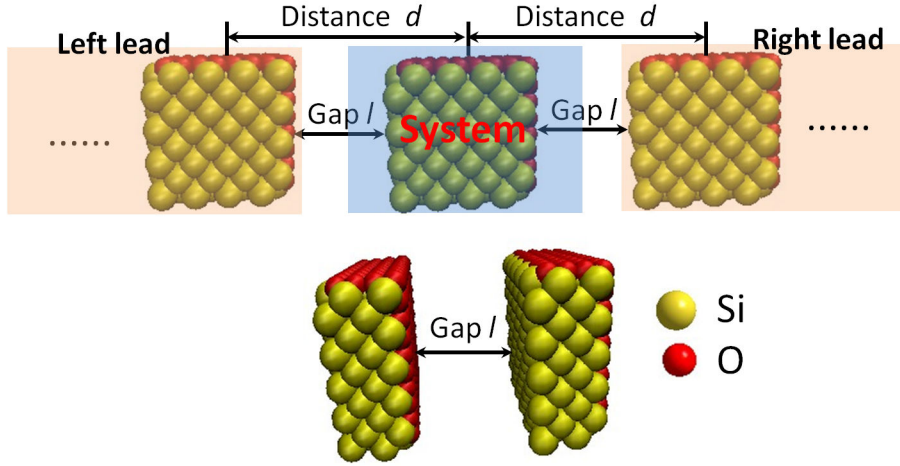


**Figure 6.3:** Schematics of the silica cluster systems considered in the Green's function calculations (top) and the ab-initio computations (bottom). For Green's function calculation, the clusters are  $N \times N \times N$  unit cells cubes with  $\text{SiO}_2$  lattice constant of 4.52 Å. In ab-initio calculations, two parallel Silica planes separated with different gap distances are used and electron densities inside the gaps are calculated with this model.

$$U = Ae^{-r/\rho} - \frac{C}{r^6} + \frac{q_i q_j}{4\pi\epsilon_0 r} \quad (6.1)$$

where  $\epsilon_0$  is the permittivity of vacuum,  $q_1$  and  $q_2$  are the charge of atom  $i$  and  $j$ , respectively.  $r$  represents the distance between atoms and  $A$ ,  $C$ , and  $\rho$  are fitting parameters of this potential. The BKS potential provides the full physical picture of the long range electromagnetic and the short-range repulsive-attractive interactions, corresponding to the third part and the first two parts in Eq. 6.1, respectively. We consider one cluster as the reference system and the clusters on its left and right sides serve as reservoirs. The system period is illustrated in Figure 1 (top). The gap conductance  $\sigma$  between two clusters is derived from the energy transmission  $Tr$  as follows (Mingo and Yang 2003;

Wang et al. 2007; Yang et al. 2012):

$$\sigma = \int_0^{\omega_{max}} T_r(\omega) \frac{\partial}{\partial T} \left( \frac{1}{e^{\hbar\omega/k_B T} - 1} \hbar\omega \frac{d\omega}{2\pi} \right) \quad (6.2)$$

where  $\omega$  and  $\omega_{max}$  are the energy and the Debye frequencies.  $T$  refers to the mean temperature of the system,  $k_B$  and  $\hbar$  represent the Boltzmann and the reduced Planck's constants, respectively.

The transmission  $T_r$  is obtained from a non-equilibrium Green's function approach (Mingo and Yang 2003; Wang et al. 2007; Yang et al. 2012) as  $T_r(\omega) = \text{Trace} [\Gamma_L G_s \Gamma_R G_s^+]$ . The advanced and retarded Green functions  $G_s^+$  and  $G_s$  can be deduced from:

$$G_s = \left[ (\omega + i\Delta)^2 I - K_{ss} - \Sigma_L - \Sigma_R \right]^{-1} \quad (6.3)$$

where  $\Delta$  is an infinitesimal imaginary part that maintains the causality of the Green's function and  $\Sigma_L = K_{ab} g_L K_{ab}^+$ ,  $\Sigma_R = K_{ab}^+ g_R K_{ab}$  are the self-energies of the left and right leads, the "+" exponent indicating the Hermitian conjugation. Finally,  $g_L$  and  $g_R$  refer to the Green's functions of the left and the right leads,  $K_{ss}$  and  $K_{ab}$  being the force constant matrices derived from the BKS potential, for one cluster and between neighboring clusters, respectively. The expression of the transmission also includes  $\Gamma_L = i(\Sigma_L - \Sigma_L^+)$  and  $\Gamma_R = i(\Gamma_R - \Gamma_R^+)$ . The details of Green's function calculations is introduced in chapter 2.

## 6.3 Physical Analysis of the Thermal Conductance between Two Clusters

### 6.3.1 Thermal Conductance

The thermal conductance between clusters obtained from Eq. 6.2 is reported in Fig. 6.4. The conductance decreases very quickly with distance in the short gap range. The power law in this range is estimated to be about  $d^{-12}$  and the absolute value of the power slightly increases with the increase of the particle size. The thermal conductance per unit cross-section indeed increases with cross section as the number of interacting pairs per atom increases. This latter number becomes larger at short distances and leads to a slight growth of the absolute exchanged power. This growth should however saturate to a maximum value as the number of interacting pairs per atom also saturates, but this limit remains beyond the maximum size under consideration here.

In the intermediate distance range, the conductance decrease with distance turns to be smoother and follows the power law  $d^{-3}$ , which is expected in the

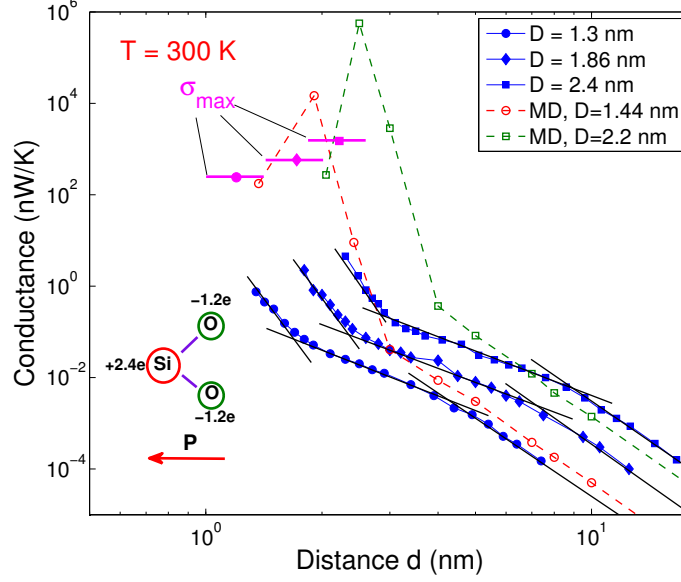


**Figure 6.4:** Thermal conductance between two neighboring clusters at 300 K for different cluster sizes versus the distance  $d$  indicated in Figure 1. In our calculations, the cluster is a cube  $N \times N \times N$  unit cells in volume. The diameter  $D$  is set in such a way that the sphere volume is equivalent to that of the simulated cube. The distance  $d$  was used as the abscissa instead of the gap distance  $l$  in order to discriminate the curves otherwise superimposed. The MD results are taken from Domingues et al *Phys. Rev. Lett.* 2005, 94: 085901, where the same BKS potential parameters as those adopted in this work were used.

framework of the non-piezoelectric interactions (Kosevich 1991). Silicon and oxygen atoms form a dipole as shown in the inset of Fig. 6.4 and each particle can be regarded as one macroscopic dipole, with bound charges of opposite sign at front and rear surfaces. When the distance between two clusters is comparable with the cluster size, the force per unit surface area between surface charges is proportional to  $\frac{S_2}{d^2}$ , where  $S_2$  is surface area of cluster 2. According to our model, the transmission of acoustic phonons through the vacuum gap can be written as (Kosevich 1991):

$$|T_{aph}|^2 = \frac{1}{1 + (\omega/\omega_0)^2} \quad (6.4)$$

where  $\omega_0$  represents the effective width of the acoustic phonon pass band through the gap;  $\omega_0$  is proportional to the modulus of the derivative of the force per unit surface area with respect to the gap width, and as a result,  $\omega_0 \propto \frac{S_2}{d^3}$ . The total thermal conductance is given by the integral of transmission (Eq. 6.4) over all frequencies times surface area of cluster 1  $S_1$  and is proportional to  $S_1\omega_0$ , and hence is characterized by the scaling  $\frac{S_1S_2}{d^3}$  (Kosevich

1991). This means that the conductance in this range of distance  $d$  is performed mainly by acoustic phonons, which is in agreement with our results obtained from Green's function (shown below). Interestingly, the slope transition in the log scale occurs at the same gap distance  $l = 4 \text{ \AA}$  whatever the cluster diameter. The distance  $d$ , gap distance  $l$ , and the diameter of cluster  $D$  have the relation  $l = d - D$ . When the gap increases further, i.e. the distance between two neighboring clusters becomes much larger than the particle size, the energy transfer between two clusters is performed by optical phonon exchange through dipole-dipole interaction (Domingues et al. 2005), following the Foerster energy transfer with a  $\frac{1}{d^6}$  decay law (Foerster 1948). The transition from the charge-charge to dipole-dipole interaction occurs smoothly when  $d$  is around three to five times the cluster size. According to the dipole-dipole approximation, the spectrum heat flux transfer from one particle to the other can be written as (Domingues et al. 2005)

$$Q_{1 \rightarrow 2} = \frac{3\alpha_1''\alpha_2''}{4\pi^3 d^6} \Theta(\omega, T) \quad (6.5)$$

where  $\alpha_1''$  and  $\alpha_2''$  are the imaginary part of the polarizability of the two particles, respectively, and  $\Theta(\omega, T) = \hbar\omega / (e^{\hbar\omega/k_B T} - 1)$  refers to the mean energy of an oscillator. In terms of power exchange, the conductance is written as

$$\sigma_{12}(T) = \frac{3}{4\pi^3} \int_0^\infty \frac{\partial \Theta(\omega, T)}{\partial T} \alpha_1''(\omega) \alpha_2''(\omega) d\omega \frac{1}{d^6} \quad (6.6)$$

So the conductance between two dipoles follows the power law of  $d^{-6}$ , which is very close to our finding.

Furthermore, in the charge-charge interaction region, the conductance at a given gap width  $l$  follows a  $D^{3.85}$  scaling law, while in the dipole-dipole interaction range, the conductance varies with diameter according to  $D^{6.5}$  for a given distance  $d$ . These findings further confirm our proposed mechanism of surface charge-charge and volume dipole-dipole heat transfer since the total conductance is proportional to the product of clusters surface areas  $S_1 S_2$ , that is to  $\frac{D_1^2 D_2^2}{d^3}$ , for surface charge-charge interaction, while the conductance is proportional to the product of clusters volumes  $V_1 V_2$ , that is to  $\frac{D_1^3 D_2^3}{d^6}$ , for volume dipole-dipole interaction.

To validate our predictions, molecular dynamics (MD) simulation results as taken from reference (Domingues et al. 2005) are plotted in Figure 2 for comparison. A clear agreement between MD and Green's function predictions appears in the long distance range. But there is no intermediate region in MD predictions and the conductance from Green's function is several orders of magnitude smaller than the one yielded from MD in the small gap range. Also in

contrast to MD simulations, no conductance decrease is found right before the contact in our Green's function calculations. Instead, the conductance increases monotonically while the gap decreases. In fact, the maximum conductance before contact predicted by MD simulations exceeds the physical upper-limit  $\sigma_{max}$  as shown in Fig. 6.4. This limit is calculated from the maximum energy  $3Nk_b(T_1 - T_2)$  possibly transferred between two neighbor clusters of  $N$  atoms each, set to temperatures  $T_1$  and  $T_2$ . Considering the fastest transfer characterized by the highest mode frequency  $f_{max}$ , the maximum conductance is obtained as  $\sigma_{max} = 3Nk_B f_{max}$ . The MD predicted conductance just before the contact is one or two orders of magnitude larger than the maximum value while the non-equilibrium Green's function predictions give estimations below this limit.

### 6.3.2 Electron Density Analysis

To understand the origin of the change in the dependence of the conductance to the distance  $d$ , we performed *ab-initio* calculations (ABINIT code (Gonze et al. 2002)) of the electron densities for two silica planes schematically shown in the below panel of Figure 1, and separated by vacuum gaps ranging from 0 to 6 Å. As each plane consists in a  $1 \times 1 \times 2$  supercell, the two cells axis being perpendicular to the interacting surfaces. Each unit cell contains twelve atoms and the simulation box includes four cells and 48 atoms. Experimental data for the atomic positions are used and the exchange-correlation Hamiltonian is treated within the generalized gradient approximation with the Perdew-Burke-Ernzerhof functional (Perdew et al. 1996). Fritz-Haber Institute pseudopotentials (Bockstedte et al. 1997) are adopted for Si and O atoms. The cut-off energy is set to 820 eV and the k-grid size to  $4 \times 4 \times 1$ .

As revealed by Fig. 6.5, the electron density is nonzero in the middle of the gap, when the gap is smaller than 4 Å but decreases rapidly as the gap widens from 0 to 4 Å. The electron density reaches zero in the middle of the gap when  $l$  increases beyond 4 Å and the zero electron density domain extends when further increasing the gap. This indicates that the electron wave functions of both sides actually overlap in the short gap range when  $l < 4$  Å to form a bond. In this region, the atoms of both sides are connected through a single electronic wave function instead of interacting through electromagnetic forces relating two separated wave functions. Beyond 4 Å, near field radiative heat transfer can be described by Maxwell equations while the quantum Schrödinger equation has to be considered when  $l < 4$  Å. Since the bonds between atoms in silica are covalent, we may call the bond before the contact as 'pseudo-covalent'. With the formation of those latter bonds, the force between two neighbors dramatically increases beyond the force produced by electromagnetic waves. As a result, heat transfer shifts from radiative to conductive, also leading to a slope change

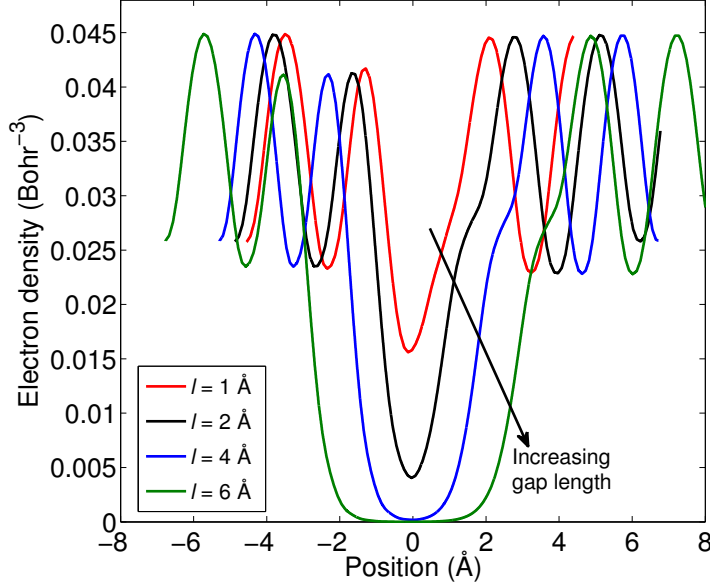


**Figure 6.5:** Ab-initio computation of the electron density generated by two parallel silica films separated by different gap widths.

of the thermal conductance in the small gap range.

### 6.3.3 Phonon Transmission Spectra

To check the relative contribution of acoustic and optical phonons to heat conduction, we now turn to our previous modeling of the transmission of acoustic phonon modes through a vacuum gap as shown in equation (3). Since  $\omega_0$  represents the effective width of the acoustic phonon pass-band through the gap and it is proportional to the derivative of the force between clusters with respect to the gap width, it decreases with the increase of the gap width. Consequently, the acoustic phonon cut-off frequency decreases when the gap widens and the frequency range of allowed transmission converges to zero.

Fig. 6.6 reports the cumulative transmission coefficient from one cluster to its neighbor as a function of frequency and distance  $l$ . The cumulative transmission function increases continuously for the smallest gap of 1 Å (black line) reflecting a continuous dependence of the transmission on frequency. The continuous decrease of the transmission as the frequency  $\omega_0$  reduces to zero reveals that the modes involved are indeed acoustical ones.

When the gap width is slightly increased from 1 Å to 4 Å, the cumulative

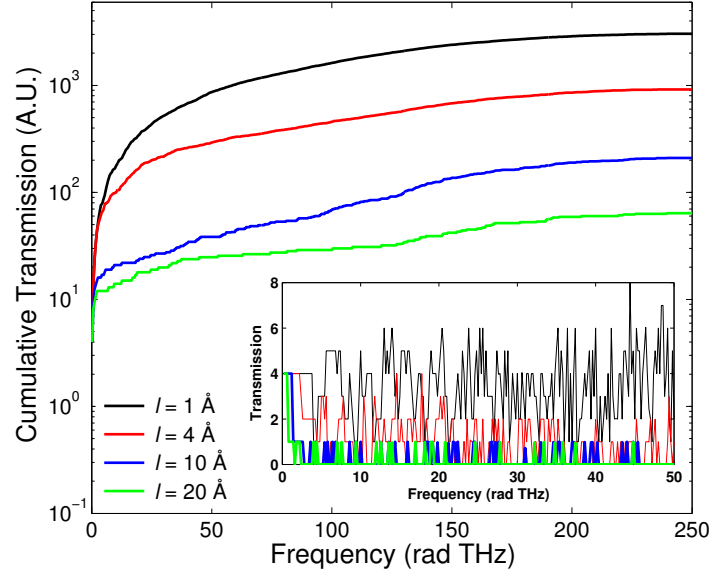


**Figure 6.6:** Angular frequency dependent cumulative phonon transmission for different gap distance  $l$  in the cluster of diameter  $D = 1.3$  nm. Inset: phonon transmission function versus angular frequency at low frequencies.

transmission function dramatically decreases and includes both a continuum at low frequencies and a set of jumps due to a discrete transmission at higher frequencies as highlighted by the inset of Figure 4. In qualitative agreement with the model of Eq. 6.4, widening the gap indeed results in a decrease of the acoustic frequency pass band, which uncovers the presence of optical contributions appearing as peaks in the transmission spectrum. A careful analysis of our data shows that the frequency range of the acoustic phonons continuum reduces to zero as the gap width reaches five times of particles size and accomplishes most of the heat transfer when the gap width is smaller than three times the particle size. The discrete set of modes also progressively disappear when the gap width is further increased and only the modes related to force constants of long range interactions remain when the gap is enlarged and those also gradually disappear as those long range interactions vanish.

The acoustic phonon behavior can also be understood with the coupling effect. Due to the acoustic sum rule, all the acoustic phonon frequency at the gamma point should be zero. Thus the acoustic modes are distributed from zero up to a maximum frequency  $\omega_{ac}^{max}$ . When the gap is very small, the coupling between neighbouring clusters is very strong and the group velocity of acoustic phonons is very large since the group velocity is proportional to the square root of coupling constant between cells, i.e.,  $v_g \propto \sqrt{K_{ab}/M}$  with  $M$  being the

mass of atoms. As a result, the maximum frequency of the acoustic phonons  $\omega_{ac}^{max}$  is large. By decreasing of the coupling strength (corresponding to a larger gap), the group velocity will decrease and results in a small frequency range of acoustic phonons (corresponding to a small  $\omega_{ac}^{max}$ ). Therefore, the acoustic modes go towards the zero frequency with the increase of the gap distance and finally disappear when the group velocity is zero. The discreteness of the optical modes is due to the same effects. If the group velocity of an optical mode vanishes or becomes very small, this optical mode disappears. Since these latter modes cannot be coupled by Coulomb interaction they do not contribute to heat transfer.

By considering the phonon-induced interactions of the gap edges, Kosevich (Kosevich 1991) and Prunnila and Meltaus (Prunnila and Meltaus 2010) have shown independently that acoustic phonons could transmit energy between separated bodies by tunneling through vacuum gap, which can led to a significant thermal conductance enhancement and which is consistent with our findings. Accordingly, Altfeder et al. (Altfeder et al. 2010) observed phonon tunneling from a sharp STM tip into a gold film at a vacuum gap distance of 3 Å. The authors claim that the tunneling effect is driven by surface electron-acoustic-phonon interaction. This result supports our argument stating that acoustic phonons are predominant in the phonon tunneling through small gaps.

In conclusion, the non-equilibrium Green's function technique has been implemented for calculating the heat transfer between two silica clusters. We found that the studied gap range can be divided into three parts with two critical gaps of 4 Å and three to five times the cluster size. The heat transfer regimes are characterized by the decay power laws of  $d^{-12}$ ,  $d^{-3}$  and  $d^{-6}$ , successively. The critical gap of 4 Å corresponds to the classical to quantum transition beyond which heat transfer between neighboring clusters follows the classical law prescribed by surface charge-charge (intermediate range) and volume dipole-dipole (long-range) interactions, while the heat flux drastically increases for the gap distance below 4 Å. Near-field radiation clearly captures the thermal interaction above  $l = 4$  Å, but the heat transfer below this distance is dominated by heat conduction as we have shown that electrons are actually forming a chemical bond in the gap. Our results thus provide a deeper insight into understanding the behavior of the transition between radiation and heat conduction in gaps smaller than a few nanometers.

## 6.4 Conclusions

A periodic plane defect of vacuum has been introduced perpendicularly to the axis of a SiO<sub>2</sub> nanowire in order to study the phonon tunnelling effect as well as the heat transfer transition from conduction to near field radiation. The

thermal conductance between two clusters at different gap distances up to 10 nm was calculated with the non-equilibrium Green's function. It was found that the studied gap range can be divided into three regions. The first region starts from the contact to the gap distance of 4 Å for all cluster sizes with a thermal conductance decay according to a power law around  $d^{-12}$ . The second region begins from the gap distance of 4 Å, i.e.,  $l = 4$  Å, and ends at a inter-cluster distance corresponding to 3-5 times the cluster size, i.e.,  $d = (3 \sim 5)D$ . In this regime, the power law of the thermal conductance variation changes to  $d^{-3}$ . The last region where a thermal conductance decay power law  $d^{-3}$  is identified ranges from  $d = (3 \sim 5)D$  up to the maximum distance in this study. With an *ab initio* calculation, we claimed that the critical gap of 4 Å corresponds to the classical to quantum transition below which electrons are actually forming a chemical bond in the gap. The heat transfer behavior beyond 4 Å was checked with previously reported models and we identified that when the gap distance is larger than 4 Å, heat transfer between neighboring clusters follows the classical law prescribed by surface charge-charge interaction (intermediate range) and volume dipole-dipole (long-range) interaction. Near-field radiation clearly captures the thermal interaction above  $l = 4$  Å, but the heat transfer below this distance is dominated by heat conduction due to the formation of chemical bonds which promote the acoustic phonon tunnelling. Our results thus provide a deeper insight into understanding the behavior of the transition between radiation and heat conduction in gaps smaller than a few nanometers.



## Chapter 7

# Conclusions and Future works

### 7.1 Conclusions

With a combination of methods including molecular dynamics, phonon Green's function, lattice dynamics, and density functional theory calculations, we have investigated the impact of various types of defects, namely screw dislocations, anti-phase boundaries, twinning boundaries, as well as vacuum gaps, on the heat transfer behaviors of nanowires. The main conclusions of this thesis are as follows:

1. The thermal transport properties have been calculated with the Non-Equilibrium Molecular Dynamics (NEMD) method for  $\langle 110 \rangle$  Si nanowires (NWs) and nanotubes (NTs) containing an axial screw dislocation (SD) in the center, as described by objective molecular dynamics coupled with the classical Tersoff potential. In accordance with the Eshelby theory, we found that the twist angle of a SD NW or NT increases with the Burger's vector while decreases with the cross-section area. We uncover a decrease in thermal conductivity in the presence of axial screw dislocations with closed and open cores. The phonon mode polarization calculation together with phonon Green's function calculation reveal that the sizeable reduction of thermal conductivity by dislocation is attributed to the enhanced phonon-phonon scattering caused by the potential anharmonicity in the highly-distorted core and, to a lesser extent, to differences in structure. As high-strain is intrinsic to dislocations, the effect should occur to various extents in other nano-materials. The dislocation effect on thermal transport can be combined with other known mechanisms, such as coating, to further hinder phonon transport.
2. According to recent experiments on anti-phase (AP) boundaries, we proposed a new type of nanowire, i.e., the anti-phase superlattice (APSL) NW. The thermal conductivity of this new type of NW 3 nm in diam-

eter is measured in a 3C SiC system with EMD simulations based on fluctuation-dissipation theory. We identified that the thermal conductivity of the period modulated APSL NWs can be suppressed to a large extent when compared to that of the pristine NW. The maximum reduction can be as high as 52% at 300 K. This minimal value corresponds only to 2.6% of the bulk SiC value at 300 K. This means that the thermal conductivity of SiC can be reduced twofold with the combination of APSL and NW effects. A lattice dynamic calculation shows that phonon group velocity is greatly decreased in APSL NWs compared to that of pristine NWs. Besides, we uncover a minimal thermal conductivity for a period of 6 nm. This minimal thermal conductivity originates from the interplay between phonon wave effect and phonon particle effect. Phonon density of states demonstrates that new vibrational states for interface atoms appear. In the Si-Si interfaces, two strong peaks emerge around 5 THz, which are identified as Si atom vibrational modes. Besides the low frequencies peaks, two gap modes around 22 THz and 30 THz due to the C atom vibrations are also observed. Because of the stiff C-C interactions, the VDOS in the C-C bonding interface regions shows a long tail above the usual cut off frequency of 35 THz. The current study shows that SiC APSL NWs may serve as a new candidate to improve the thermoelectric performance of SiC, where the high thermal conductivity is the main hurdle for increasing the figure of merit.

- Using NEMD simulations, we found that the thermal conductivity of the twinning SL NWs shows a large reduction up to 65% in comparison with that of the pristine NW at room temperature. Due to the enhanced anharmonic scatterings at high temperatures, the thermal conductivity reduction decreases with temperature. When the period of twinning SL NWs changes, a minimal thermal conductivity can be observed and the corresponding period is diameter dependent and almost equals to the diameter of the NW. Mode analysis reveals that the minimal thermal conductivity arises due to the disappearance of favored atom polarization directions. Phonon dispersion studies show that the zigzag structure of the twinning SL NW results in a small group velocity, which is the immediate cause of the thermal conductivity suppression. The phonon group velocity decrease is also revealed in the phonon transmission spectra, where the transmission of the twinning SL NWs is much smaller than that of the pristine one. Moreover, a small phononic band gap between acoustic and optical branches was observed in the twinning SL NWs. We also found that the considered mechanism of geometry-induced reduction of thermal conductivity in twinning SLs can be complemented by other known mechanisms to further reduce thermal conductivity in phononic metamaterials.

4. The thermal conductance between two clusters at sub-10 nm gaps was calculated with the non-equilibrium Green's function. We captured that the thermal conductance changes with inter-cluster distances according to three different behaviors in the studied distance range, i.e., the short range region with a gap distance below 4 Å for all cluster sizes and the thermal conductance decay according to a power law around  $d^{-12}$ ; the intermediate region from  $l = 4$  Å to  $d = (3 \sim 5)D$ , where the thermal conductance is proportional to  $d^{-3}$ ; the long range region with  $d > (3 \sim 5)D$ , where a thermal conductance decay power law  $d^{-6}$  is identified. With an *ab initio* calculation, we have shown that the critical gap of 4 Å corresponds to the classical to quantum transition below which chemical bonds are formed by shared electrons in the gap. The heat transfer behavior beyond 4 Å is checked with the previously reported models and we identify that when the gap distance is larger than 4 Å, heat transfer between neighboring clusters follows the classical law prescribed by surface charge-charge interaction (intermediate range) and volume dipole-dipole (long-range) interaction. Near-field radiation clearly captures the thermal interaction above  $l = 4$  Å, but the heat transfer below this distance is dominated by heat conduction due to the formation of chemical bonds which promote the acoustic phonon tunnelling. Our results thus provide a deeper insight into understanding the behavior of the transition between radiation and heat conduction in gaps smaller than a few nanometers.

## 7.2 Future Works

There are three extensions of the work presented here that should be pursued:

1. According to the experimental findings, in most cases, a nanowire with a screw dislocation will also be surrounded by small branched nanowires. It would be meaningful to perform simulations on thermal properties for such a real structure as a branched nanowire can produce phonon resonance effect. Combining this effect with the strain effect produced by dislocations, this dislocated-branched-nanowire should possess an extremely low thermal conductivity.
2. The studies on the twinning superlattice nanowires are focused on perfect twinning boundaries at present. While in real situations, the twin boundaries always contain dislocations (screw or edge). We have shown that a perfect twinning boundary has no impact on phonon transport. To introduce dislocations on twinning boundaries would change the boundary scatterings, providing an enhanced phonon blocking effect.
3. We focused all our studies on thermal transport properties in this thesis,

while it is also crucial to know the electron transport properties for our designed structures, especially for thermoelectric applications. Using the Green's function together with the tight-binding model, it is possible to calculate the electrical conductance, the Seebeck coefficient, and also the thermal conductance. Consequently, the thermoelectric figure of merit  $ZT = S^2\sigma T/\kappa$  can be calculated within the ballistic regime.

# References

- Achim, K. (2009). Nanophotonics: Probing near-field thermal radiation. *Nat. Photonics* 3, 492–494. (p. 97)
- Akatyeva, E. and T. Dumitrică (2012, Jul). Eshelby twist and magic helical zinc oxide nanowires and nanotubes. *Phys. Rev. Lett.* 109, 035501. (p. 47)
- Akatyeva, E., L. Kou, I. Nikiforov, T. Frauenheim, and T. Dumitrică (2012). Electrically active screw dislocations in helical zno and si nanowires and nanotubes. *ACS Nano* 6(11), 10042–10049. (p. 47, 48, 50, 52)
- Algra, P. E., M. A. Verheijen, M. T. Borgstrom, L. Feiner, G. Immink, W. J. P. van Enkevort, E. Vlieg, and E. P. A. M. Bakkers (2008). *Nature* 456, 369. (p. 79)
- Allen, M. and D. Tildesley (1989). *Computer Simulation of Liquids*. Oxford University Press. (p. 24)
- Allen, M. P. (2004). Introduction to molecular dynamics simulation. *Computational soft matter: From synthetic polymers to proteins* 23, 1–28. (p. 23)
- Allen, P. B., J. L. Feldman, J. Fabian, and F. Wooten (1999). Diffusons, locons and propagons: Character of atomic vibrations in amorphous si. *Philosophical Magazine Part B* 79(11-12), 1715–1731. (p. 40)
- Altfeder, I., A. A. Voevodin, and A. K. Roy (2010, Oct). Vacuum phonon tunneling. *Phys. Rev. Lett.* 105, 166101. (p. 98, 106)
- Asen-Palmer, M., K. Bartkowski, E. Gmelin, M. Cardona, A. P. Zhemov, A. V. Inyushkin, A. Taldenkov, V. Ozhogin, K. M. Itoh, and E. E. Haller (1997). *Phys. Rev. B* 56, 9431. (p. 90)
- Berman, R. (1976). *Thermal conduction in solids*. Clarendon Press: Oxford, U.K. (p. 46)
- Bierman, M. J., Y. K. A. Lau, A. V. Kvit, A. L. Schmitt, and S. Jin (2008). Dislocation-driven nanowire growth and eshelby twist. *Science* 320(5879), 1060–1063. (p. 45, 47)
- Bockstedte, M., A. Kley, J. Neugebauer, and M. Scheffler (1997). Density-functional theory calculations for poly-atomic systems: electronic structure, static and elastic properties and ab initio molecular dynamics. *Computer Physics Communications* 107(13), 187 – 222. (p. 103)
- Bodapati, A., P. K. Schelling, S. R. Phillpot, and P. Keblinski (2006, Dec). Vibrations and thermal transport in nanocrystalline silicon. *Phys. Rev.*

- B* 74, 245207. (p. 39, 40, 55)
- Boukai, A. I., Y. Bunimovich, J. Tahir-Kheli, J. K. Yu, W. A. Goddard, and J. R. Heath (2008). *Nature* 451, 168. (p. 78)
- Bux, S. K., R. G. Blair, P. K. Gogna, H. Lee, G. Chen, M. S. Dresselhaus, R. B. Kaner, and J. P. Fleurial (2009). *Adv. Funct. Mater.* 19, 2445. (p. 78)
- Cahill, D. G., P. V. Braun, G. Chen, D. R. Clarke, S. Fan, K. E. Goodson, P. Keblinski, W. P. King, G. D. Mahan, A. Majumdar, H. J. Maris, S. R. Phillpot, E. Pop, and L. Shi (2014). Nanoscale thermal transport. ii. 2003-2012. *Applied Physics Reviews* 1, 011305. (p. 21, 62, 68)
- Carruthers, P. (1961, Jan). Theory of thermal conductivity of solids at low temperatures. *Rev. Mod. Phys.* 33, 92–138. (p. 20)
- Casimir, H. B. G. (1938). Note on the conduction of heat in crystals. *Physica* 5, 495 – 500. (p. 16)
- Cattaneo, C. (1958). Sur une forme de l'equation de la chaleur eliminant le paradoxe d'une propagation instantanee. *C. R. Acad. Sci.* 247, 431–433. (p. 26)
- Chalopin, Y., N. Mingo, J. Diao, D. Srivastava, and S. Volz (2012). Large effects of pressure induced inelastic channels on interface thermal conductance. *Applied Physics Letters* 101(22), -. (p. 58)
- Chang, C. W., D. Okawa, H. Garcia, A. Majumdar, and A. Zettl (2008, Aug). Breakdown of fourier's law in nanotube thermal conductors. *Phys. Rev. Lett.* 101, 075903. (p. 17, 82)
- Chang, C. W., D. Okawa, A. Majumdar, and A. Zettl (2006). Solid-state thermal rectifier. *Science* 314(5802), 1121–1124. (p. 8)
- Chapuis, P.-O., M. Laroche, S. Volz, and J.-J. Greffet (2008). Radiative heat transfer between metallic nanoparticles. *Applied Physics Letters* 92(20), -. (p. 97)
- Chapuis, P.-O., S. Volz, C. Henkel, K. Joulain, and J.-J. Greffet (2008, Jan). Effects of spatial dispersion in near-field radiative heat transfer between two parallel metallic surfaces. *Phys. Rev. B* 77, 035431. (p. 97)
- Che, J., T. Cagin, W. Deng, and W. A. Goddard (2000). Thermal conductivity of diamond and related materials from molecular dynamics simulations. *The Journal of Chemical Physics* 113(16), 6888–6900. (p. 26, 27)
- Chen, J., G. Zhang, and B. Li (2010). *Nano Lett.* 10, 3978. (p. 78)
- Chen, P., N. A. Katcho, J. P. Feser, W. Li, M. Glaser, O. G. Schmidt, D. G. Cahill, N. Mingo, and A. Rastelli (2013, Sep). Role of surface-segregation-driven intermixing on the thermal transport through planar si/ge superlattices. *Phys. Rev. Lett.* 111, 115901. (p. 78)
- Cheng, C., W. Fan, J. Cao, S.-G. Ryu, J. Ji, C. P. Grigoropoulos, and J. Wu (2011). Heat transfer across the interface between nanoscale solids and gas. *ACS Nano* 5(12), 10102–10107. (p. 95)
- Cheng, G., T.-H. Chang, Q. Qin, H. Huang, and Y. Zhu (2014). Mechanical

- properties of silicon carbide nanowires: Effect of size-dependent defect density. *Nano Letters* 14(2), 754–758. (p. 62)
- Dammak, H., Y. Chalopin, M. Laroche, M. Hayoun, and J.-J. Greffet (2009, Nov). Quantum thermal bath for molecular dynamics simulation. *Phys. Rev. Lett.* 103, 190601. (p. 30)
- Dhar, A. (2001, Apr). Heat conduction in a one-dimensional gas of elastically colliding particles of unequal masses. *Phys. Rev. Lett.* 86, 3554–3557. (p. 17)
- Ding, K. and H. C. Andersen (1986, Nov). Molecular-dynamics simulation of amorphous germanium. *Phys. Rev. B* 34, 6987–6991. (p. 80, 91)
- Domingues, G., S. Volz, K. Joulain, and J.-J. Greffet (2005, Mar). Heat transfer between two nanoparticles through near field interaction. *Phys. Rev. Lett.* 94, 085901. (p. 97, 102)
- Dumitrica, T. and R. D. James (2007). Objective molecular dynamics. *Journal of the Mechanics and Physics of Solids* 55(10), 2206 – 2236. (p. 48)
- Emmanuel, R., S. Alessandro, J. Guillaume, V. Sebastian, C. Fabio, C. Joel, and G. Jean-Jacques (2009). Radiative heat transfer at the nanoscale. *Nat. Photonics* 3, 514–517. (p. 97)
- Eshelby, J. D. (1953). Screw dislocations in thin rods. *Journal of Applied Physics* 24(2), 176–179. (p. 47, 49)
- Ethier, S. and L. J. Lewis (1992, 10). Epitaxial growth of silxgex on si(100)2x1: A molecular-dynamics study. *Journal of Materials Research* 7, 2817–2827. (p. 91)
- Foerster, T. (1948). *Ann. Phys. (Paris)* 2, 55. (p. 102)
- Gonze, X., J.-M. Beuken, R. Caracas, F. Detraux, M. Fuchs, G.-M. Rignanese, L. Sindic, M. Verstraete, G. Zerah, F. Jollet, M. Torrent, A. Roy, M. Mikami, P. Ghosez, J.-Y. Raty, and D. Allan (2002). First-principles computation of material properties: the {ABINIT} software project. *Computational Materials Science* 25(3), 478 – 492. (p. 103)
- Grassberger, P., W. Nadler, and L. Yang (2002, Oct). Heat conduction and entropy production in a one-dimensional hard-particle gas. *Phys. Rev. Lett.* 89, 180601. (p. 17)
- Haile, S. M. (2014). Maintaining hope for sustainable energy. *MRS Bulletin* 39, 213. (p. 2)
- Han, T., T. Yuan, B. Li, and C.-W. Qiu (2013, 04). Homogeneous thermal cloak with constant conductivity and tunable heat localization. *Sci. Rep.* 3. (p. 10)
- Hanrath, T. and B. Korgel (2003). Supercritical fluidliquidsolid (sfls) synthesis of si and ge nanowires seeded by colloidal metal nanocrystals. *Advanced Materials* 15(5), 437–440. (p. 45)
- Harman, T. C., P. J. Taylor, M. P. Walsh, and B. E. LaForge (2002). Quantum dot superlattice thermoelectric materials and devices. *Science* 297, 2229. (p. 5)
- He, Y. and G. Galli (2012, May). Microscopic origin of the reduced thermal

- conductivity of silicon nanowires. *Phys. Rev. Lett.* *108*, 215901. (p. 53, 78)
- Hicks, L. D. and M. S. Dresselhaus (1993). Effect of quantum-well structures on the thermoelectric figure of merit. *Phys. Rev. B* *47*, 12727. (p. 5)
- Hochbaum, A. I., R. Chen, R. D. Delgado, W. Liang, E. C. Garnett, M. Najarian, A. Majumdar, and P. Yang (2008). *Nature* *451*, 163. (p. 78)
- Hoover, W. G. (1985, Mar). Canonical dynamics: Equilibrium phase-space distributions. *Phys. Rev. A* *31*, 1695–1697. (p. 48, 65, 81)
- Hsu, K. F., S. Loo, F. Guo, W. Chen, J. S. Dyck, C. Uher, T. Hogan, E. K. Polychroniadis, and M. G. Kanatzidis (2004). Cubic agpbmsbte<sub>2+m</sub>: Bulk thermoelectric materials with high figure of merit. *Science* *303*(5659), 818–821. (p. 5)
- Hu, B., L. Yang, and Y. Zhang (2006, Sep). Asymmetric heat conduction in nonlinear lattices. *Phys. Rev. Lett.* *97*, 124302. (p. 7)
- Hu, M., K. P. Giapis, J. V. Goicochea, X. Zhang, and D. Poulikakos (2011). Significant reduction of thermal conductivity in si/ge coreshell nanowires. *Nano Letters* *11*(2), 618–623. (p. 53)
- Hu, M. and D. Poulikakos (2012). *Nano Lett.* *12*, 5487. (p. 78, 82)
- Hyldgaard, P. and G. D. Mahan (1997, Nov). Phonon superlattice transport. *Phys. Rev. B* *56*, 10754–10757. (p. 21, 62, 83)
- Ikonic, Z., G. P. Srivastava, and J. C. Inkson (1995, Nov). Optical properties of twinning superlattices in diamond-type and zinc-blende-type semiconductors. *Phys. Rev. B* *52*, 14078–14085. (p. 79)
- Ikonić, Z., G. P. Srivastava, and J. C. Inkson (1993, Dec). Electronic properties of twin boundaries and twinning superlattices in diamond-type and zinc-blende-type semiconductors. *Phys. Rev. B* *48*, 17181–17193. (p. 64, 79)
- Ishai, M. B. and F. Patolsky (2009). Shape- and dimension-controlled single-crystalline silicon and sige nanotubes: Toward nanofluidic fet devices. *Journal of the American Chemical Society* *131*(10), 3679–3689. PMID: 19226180. (p. 55)
- Ivanova, L., P. Aleksandrov, and K. Demakov (2006). Thermoelectric properties of vapor-grown polycrystalline cubic sic. *Inorganic Materials* *42*(11), 1205–1209. (p. 62)
- Jacobs, B. W., M. A. Crimp, K. McElroy, and V. M. Ayres (2008). Nanopipes in gallium nitride nanowires and rods. *Nano Letters* *8*(12), 4353–4358. (p. 45)
- James, R. (2006). Objective structures. *Journal of the Mechanics and Physics of Solids* *54*(11), 2354 – 2390. (p. 48)
- Jia, Z., P. Hailin, M. A.F., B. D.M., N. W. D., and C. Yi (2008). Formation of chiral branched nanowires by the eshelby twist. *Nature Nanotechnology* *3*, 477–481. (p. 45)
- Jiang, J. W., N. Yang, B. S. Wang, and T. Rabczuk (2013). *Nano Lett.* *13*, 1670. (p. 78, 85)

- Jin, S., M. J. Bierman, and S. A. Morin (2010). A new twist on nanowire formation: Screw-dislocation-driven growth of nanowires and nanotubes. *The Journal of Physical Chemistry Letters* 1(9), 1472–1480. (p. 45, 47)
- Joulain, K., J.-P. Mulet, F. Marquier, R. Carminati, and J.-J. Greffet (2005). Surface electromagnetic waves thermally excited: Radiative heat transfer, coherence properties and casimir forces revisited in the near field. *Surface Science Reports* 57(34), 59 – 112. (p. 97)
- Kazan, M., G. Guisbiers, S. Pereira, M. R. Correia, P. Masri, A. Bruyant, S. Volz, and P. Royer (2010). Thermal conductivity of silicon bulk and nanowires: Effects of isotopic composition, phonon confinement, and surface roughness. *Journal of Applied Physics* 107(8), 083503. (p. 78)
- Keldysh, L. V. (1965). Ionization in the field of a strong electromagnetic wave. *Soviet Physics JETP* 20, 1307–1314. (p. 30)
- Kim, J., Y. Choi, D. Choi, and S. Choi (2011). Study on the thermoelectric properties of cvd sic deposited with inert gases. *Journal of Electronic Materials* 40(5), 840–844. (p. 62)
- KIM, J. G., Y. Y. CHOI, D. J. CHOI, J. I. KIM, B. S. KIM, and S. M. CHOI (2009). A study on the thermoelectric properties of chemical vapor deposited sic films with temperature and diluent gases variation. *Journal of the Ceramic Society of Japan* 117(1365), 574–577. (p. 62)
- Kitagawa, H., N. Kado, and Y. Noda (2002). *Materials Transactions* 43, 3239–3241. (p. 62)
- Klemens, P. G. (1958). Thermal conductivity and lattice vibrational modes. *Solid State Physics* 7, 1–98. (p. 46, 51)
- Kneeze, G. A. and A. V. Granato (1982, Feb). Effect of independent and coupled vibrations of dislocations on low-temperature thermal conductivity in alkali halides. *Phys. Rev. B* 25, 2851–2866. (p. 46)
- Koh, Y. K., Y. Cao, D. G. Cahill, and D. Jena (2009). Heat-transport mechanisms in superlattices. *Advanced Functional Materials* 19(4), 610–615. (p. 21, 62, 83)
- Kosevich, Y. (1991). Van der waals coupled surface waves in nonpiezoelectric crystals and thin films. *Physics Letters A* 155(45), 295 – 298. (p. 97, 98, 101, 102, 106)
- Krive, I. V. and E. R. Mucciolo (1999, Jul). Transport properties of quasi-particles with fractional exclusion statistics. *Phys. Rev. B* 60, 1429–1432. (p. 18)
- Kubo, R., M. Toda, and N. Hashitsume (1985). *Statistical Physics II*. Springer, Berlin. (p. 26, 65)
- Lee, M. L. and R. Venkatasubramanian (2008). Effect of nanodot areal density and period on thermal conductivity in sigesi nanodot superlattices. *Applied Physics Letters* 92(5), 053112. (p. 21, 62, 83)
- Leonhardt, U. (2006). Optical conformal mapping. *Science* 312(5781), 1777–1780. (p. 10)
- Lepri, S., R. Livi, and A. Politi (1997, Mar). Heat conduction in chains of

- nonlinear oscillators. *Phys. Rev. Lett.* *78*, 1896–1899. (p. 17)
- Lepri, S., Livi, R., and Politi, A. (1998). On the anomalous thermal conductivity of one-dimensional lattices. *Europhys. Lett.* *43*(3), 271–276. (p. 17)
- Li, B., J. Lan, and L. Wang (2005, Sep). Interface thermal resistance between dissimilar anharmonic lattices. *Phys. Rev. Lett.* *95*, 104302. (p. 7)
- Li, B., L. Wang, and G. Casati (2004, Oct). Thermal diode: Rectification of heat flux. *Phys. Rev. Lett.* *93*, 184301. (p. 7, 8)
- Li, D., Y. Wu, P. Kim, L. Shi, P. Yang, and A. Majumdar (2003). Thermal conductivity of individual silicon nanowires. *Applied Physics Letters* *83*(14), 2934–2936. (p. 16, 53, 78)
- Li, J., L. Porter, and S. Yip (1998). Atomistic modeling of finite-temperature properties of crystalline b-sic ii. thermal conductivity and effects of point defects. *The Journal of Chemical Physics* *255*, 139–152. (p. 26)
- Li, N., J. Ren, L. Wang, G. Zhang, P. Hänggi, and B. Li (2012, Jul). <i>colloquium</i>: Phononics: Manipulating heat flow with electronic analogs and beyond. *Rev. Mod. Phys.* *84*, 1045–1066. (p. 8)
- Li, X., K. Maute, M. L. Dunn, and R. Yang (2010, Jun). Strain effects on the thermal conductivity of nanostructures. *Phys. Rev. B* *81*, 245318. (p. 58)
- Lin, Z., L. Wang, J. Zhang, X.-Y. Guo, W. Yang, H.-K. Mao, and Y. Zhao (2010). Nanoscale twinning-induced elastic strengthening in silicon carbide nanowires. *Scripta Materialia* *63*(10), 981–984. (p. 79)
- Liu, S., X. Xu, R. Xie, G. Zhang, and B. Li (2012). Anomalous heat conduction and anomalous diffusion in low dimensional nanoscale systems. *The European Physical Journal B* *85*(10), 1–20. (p. 17)
- Lopez, F. J., E. R. Hemesath, and L. J. Lauhon (2009). *Nano Lett.* *9*, 2774. (p. 79)
- Lu, L., Y. Shen, X. Chen, L. Qian, and K. Lu (2004). Ultrahigh strength and high electrical conductivity in copper. *Science* *304*(5669), 422–426. (p. 84)
- Ma, Y., L. Lan, W. Jiang, F. Sun, and S. He (2013, 11). A transient thermal cloak experimentally realized through a rescaled diffusion equation with anisotropic thermal diffusivity. *NPG Asia Mater* *5*, e73–. (p. 9)
- Madsen, G. K. H. (2006). Automated search for new thermoelectric materials: The case of liznsb. *JACS* *128*, 12140. (p. 4)
- Maestre, D., D. Haussler, A. Cremades, W. Jager, and J. Piqueras (2011). Complex defect structure in the core of sn-doped in<sub>2</sub>o<sub>3</sub> nanorods and its relationship with a dislocation-driven growth mechanism. *The Journal of Physical Chemistry C* *115*(37), 18083–18087. (p. 45)
- Marcinkowski, M. J. and N. Brown (1962). Direct observation of antiphase boundaries in the fe<sub>3</sub>al superlattice. *Journal of Applied Physics* *33*(2), 537–552. (p. 63)
- Maria Kemper, R., T. Schupp, M. Häberlen, T. Niendorf, H.-J. Maier, A. Dempewolf, F. Bertram, J. Christen, R. Kirste, A. Hoffmann, J. Lindner, and D. Josef As (2011). Anti-phase domains in cubic gan. *Journal of*

- Applied Physics* 110(12), 123512. (p. 63)
- Martin, P., Z. Aksamija, E. Pop, and U. Ravaioli (2009, Mar). Impact of phonon-surface roughness scattering on thermal conductivity of thin si nanowires. *Phys. Rev. Lett.* 102, 125503. (p. 53)
- McGaughey, A. and M. Kaviany (2004). Thermal conductivity decomposition and analysis using molecular dynamics simulations. part i. lennard-jones argon. *International Journal of Heat and Mass Transfer* 47(8-9), 1783 – 1798. (p. 26, 27)
- Meng, F., S. A. Morin, A. Forticaux, and S. Jin (2013). Screw dislocation driven growth of nanomaterials. *Accounts of Chemical Research* 46(7), 1616–1626. (p. 45)
- Mingo, N. (2003). *Phys. Rev. B* 68, 113308. (p. 90)
- Mingo, N. (2006, Sep). Anharmonic phonon flow through molecular-sized junctions. *Phys. Rev. B* 74, 125402. (p. 35)
- Mingo, N. and L. Yang (2003, Dec). Phonon transport in nanowires coated with an amorphous material: An atomistic green’s function approach. *Phys. Rev. B* 68, 245406. (p. 30, 100)
- Morin, S. A., M. J. Bierman, J. Tong, and S. Jin (2010). Mechanism and kinetics of spontaneous nanotube growth driven by screw dislocations. *Science* 328(5977), 476–480. (p. 45, 47, 50)
- Morin, S. A. and S. Jin (2010). Screw dislocation-driven epitaxial solution growth of zno nanowires seeded by dislocations in gan substrates. *Nano Letters* 10(9), 3459–3463. (p. 45, 47)
- Morko, H., S. Strite, G. B. Gao, M. E. Lin, B. Sverdlov, and M. Burns (1994). Larged semiconductor device technologies. *Journal of Applied Physics* 76(3), 1363–1398. (p. 62)
- Narayanaswamy, A., S. Shen, and G. Chen (2008, Sep). Near-field radiative heat transfer between a sphere and a substrate. *Phys. Rev. B* 78, 115303. (p. 97)
- Ni, Y., H. Le Khanh, Y. Chalopin, J. Bai, P. Lebarney, L. Divay, and S. Volz (2012). Highly efficient thermal glue for carbon nanotubes based on azide polymers. *Appl. Phys. Lett.* 100(19), -. (p. 5, 97)
- Nikiforov, I., D.-B. Zhang, and T. Dumitric (2011). Screw dislocations in 100 silicon nanowires: An objective molecular dynamics study. *The Journal of Physical Chemistry Letters* 2(20), 2544–2548. (p. 47)
- Ninomiya, T. (1968). Dislocation vibration and phonon scattering. *Journal of the Physical Society of Japan* 25(3), 830–840. (p. 46)
- Nosé, S. (1984). *Mol. Phys.* 53, 255. (p. 48, 65, 81)
- Nukala, P., R. Agarwal, X. Qian, M. H. Jang, S. Dhara, K. Kumar, A. T. C. Johnson, J. Li, and R. Agarwal (2014). Direct observation of metalinsulator transition in single-crystalline germanium telluride nanowire memory devices prior to amorphization. *Nano Letters* 14(4), 2201–2209. (p. 63)
- Ohta, H., S. Kim, Y. Mune, T. Mizoguchi, K. Nomura, S. Ohta, T. Nomura, Y. Nakanishi, Y. Ikuhara, M. Hirano, H. Hosono, and K. Koumoto (2007).

- Giant thermoelectric seebeck coefficient of a two-dimensional electron gas in strontium titanate. *Nat Mater* 6, 129. (p. 5)
- Pendry, J. B., D. Schurig, and D. R. Smith (2006). Controlling electromagnetic fields. *Science* 312(5781), 1780–1782. (p. 10)
- Perdew, J. P., K. Burke, and M. Ernzerhof (1996, Oct). Generalized gradient approximation made simple. *Phys. Rev. Lett.* 77, 3865–3868. (p. 103)
- Pirouz, P., C. M. Chorney, and J. A. Powell (1987). Antiphase boundaries in epitaxially grown sic. *Applied Physics Letters* 50(4), 221–223. (p. 63)
- Plimpton, S. (1995). Fast parallel algorithms for short-range molecular dynamics. *Journal of Computational Physics* 117(1), 1 – 19. (p. 48, 64, 80)
- Polder, D. and M. Van Hove (1971, Nov). Theory of radiative heat transfer between closely spaced bodies. *Phys. Rev. B* 4, 3303–3314. (p. 97)
- Poon, G. J. (2001). Chapter 2 electronic and thermoelectric properties of half-heusler alloys. In T. M. Tritt (Ed.), *Recent Trends in Thermoelectric Materials Research II*, Volume 70 of *Semiconductors and Semimetals*, pp. 37 – 75. Elsevier. (p. 5)
- Prunnila, M. and J. Meltaus (2010, Sep). Acoustic phonon tunneling and heat transport due to evanescent electric fields. *Phys. Rev. Lett.* 105, 125501. (p. 97, 98, 106)
- Rajabpour, A. and S. Volz (2010). Thermal boundary resistance from mode energy relaxation times: Case study of argon-like crystals by molecular dynamics. *Journal of Applied Physics* 108(9), 094324. (p. 62)
- Rego, L. G. C. and G. Kirczenow (1999, May). Fractional exclusion statistics and the universal quantum of thermal conductance: A unifying approach. *Phys. Rev. B* 59, 13080–13086. (p. 18)
- Rowe, D. M. (1995). *CRC Handbook of thermoelectrics*. CRC, Boca Raton. (p. 2)
- Sales, B. C., D. Mandrus, and R. K. Williams (1996). Filled skutterudite antimonides: A new class of thermoelectric materials. *Science* 272(5266), 1325–1328. (p. 5)
- Samolyuk, G., S. Golubov, Y. Osetsky, and R. Stoller (2011). Molecular dynamics study of influence of vacancy types defects on thermal conductivity of sic. *Journal of Nuclear Materials* 418(13), 174 – 181. (p. 68, 75)
- Sancho, M. P. L., J. M. L. Sancho, J. M. L. Sancho, and J. Rubio (1985). Highly convergent schemes for the calculation of bulk and surface green functions. *Journal of Physics F: Metal Physics* 15(4), 851. (p. 33)
- Schelling, P. K. and S. R. Phillpot (2001). Mechanism of thermal transport in zirconia and yttria-stabilized zirconia by molecular-dynamics simulation. *Journal of the American Ceramic Society* 84(12), 2997–3007. (p. 39, 85)
- Schelling, P. K., S. R. Phillpot, and P. Keblinski (2002, Apr). Comparison of atomic-level simulation methods for computing thermal conductivity. *Phys. Rev. B* 65, 144306. (p. 25, 29, 48, 52)

- Schittny, R., M. Kadic, S. Guenneau, and M. Wegener (2013). Experiments on transformation thermodynamics: Molding the flow of heat. *Phys. Rev. Lett.* *110*, 195901. (p. 10)
- Schwab, K., E. A. Henriksen, J. M. Worlock, and M. L. Roukes (2000, 04). Measurement of the quantum of thermal conductance. *Nature* *404* (6781), 974–977. (p. 17, 18)
- Shen, S., A. Narayanaswamy, and G. Chen (2009). Surface phonon polaritons mediated energy transfer between nanoscale gaps. *Nano Letters* *9*(8), 2909–2913. PMID: 19719110. (p. 97)
- Shibahara, K., S. Nishino, and H. Matsunami (1987). Antiphase domain free growth of cubic sic on si(100). *Applied Physics Letters* *50*(26), 1888–1890. (p. 63)
- Simkin, M. V. and G. D. Mahan (2000, Jan). Minimum thermal conductivity of superlattices. *Phys. Rev. Lett.* *84*, 927–930. (p. 21, 62, 83)
- Snyder, G. J., M. Christensen, E. Nishibori, T. Caillat, and B. B. Iversen (2004). Disordered zinc in zn4sb3 with phonon-glass and electron-crystal thermoelectric properties. *Nat Mater* *3*, 458. (p. 5)
- Snyder, G. J. and E. S. Toberer (2008). Complex thermoelectric materials. *Nat Mater* *7*, 105. (p. 1, 2)
- Sofin, R. G. S., S. K. Arora, and I. V. Shvets (2011). *Phys. Rev. B* *83*, 134436. (p. 63)
- Sproull, R. L., M. Moss, and H. Weinstock (1959). Effect of dislocations on the thermal conductivity of lithium fluoride. *Journal of Applied Physics* *30*(3), 334–337. (p. 47)
- Stillinger, F. H. and T. A. Weber (1985, Apr). Computer simulation of local order in condensed phases of silicon. *Phys. Rev. B* *31*, 5262–5271. (p. 80)
- T. M. Tritt, A. (2011). *Rev. Mater. Res.* *41*, 433. (p. 78)
- Termentzidis, K., T. Barreateau, Y. Ni, S. Merabia, X. Zianni, Y. Chalopin, P. Chantrenne, and S. Volz (2013, Mar). Modulated sic nanowires: Molecular dynamics study of their thermal properties. *Phys. Rev. B* *87*, 125410. (p. 69, 70)
- Termentzidis, K. and S. Merabia (2012). *Molecular Dynamics Simulations and Thermal Transport at the Nano-Scale*. InTech. (p. 28)
- Termentzidis, K., O. Pokropyvnyy, M. Woda, S. Xiong, Y. Chumakov, P. Cortona, and S. Volz (2013). Large thermal conductivity decrease in point defective bi2te3 bulk materials and superlattices. *Journal of Applied Physics* *113*(1), -. (p. 19)
- Terraneo, M., M. Peyrard, and G. Casati (2002, Feb). Controlling the energy flow in nonlinear lattices: A model for a thermal rectifier. *Phys. Rev. Lett.* *88*, 094302. (p. 7)
- Tersoff, J. (1989, Mar). Modeling solid-state chemistry: Interatomic potentials for multicomponent systems. *Phys. Rev. B* *39*, 5566–5568. (p. 48, 64)
- Touloukian, Y. S., R. Powell, C. Y. Ho, and P. G. Klemens (1970). *Ther-*

- mophysical Properties of Matter Volume 2, Thermal Conductivity: Non-metallic Solids*. IFI/Plenum, New York-Washington. (p. 5)
- van Beest, B. W. H., G. J. Kramer, and R. A. van Santen (1990, Apr). Force fields for silicas and aluminophosphates based on ab initio calculations. *Phys. Rev. Lett.* 64, 1955–1958. (p. 99)
- Venkatasubramanian, R., E. Siivola, T. Colpitts, and B. O’Quinn (2001). Thin-film thermoelectric devices with high room-temperature figures of merit. *Nature* 413, 597. (p. 5)
- Vernotte, P. (1958). Les paradoxes de la theorie continue de l’equation de la chaleur. *C. R. Acad. Sci.* 246, 3154–3155. (p. 26)
- Volokitin, A. I. and B. N. J. Persson (2007, Oct). Near-field radiative heat transfer and noncontact friction. *Rev. Mod. Phys.* 79, 1291–1329. (p. 97)
- Volz, S. (2009). *Thermal Nanosystems and Nanomaterials*. Springer Heidelberg. (p. 33, 35)
- Volz, S. and D. Lemonnier (2000). Confined phonon and size effects on nanowire thermal conductivity. the radiative transfer approach. *Phys. Low-Dimen. Struct.* 5/6, 91. (p. 78)
- Volz, S., J. Saulnier, G. Chen, and P. Beauchamp (2000). Computation of thermal conductivity of si/ge superlattices by molecular dynamics techniques. *Microelectronics Journal* 31 (9-10), 815–819. (p. 21, 62)
- Volz, S., J.-B. Saulnier, M. Lallemand, B. Perrin, P. Depondt, and M. Mareschal (1996, Jul). Transient fourier-law deviation by molecular dynamics in solid argon. *Phys. Rev. B* 54, 340–347. (p. 26)
- Volz, S. G. and G. Chen (1999). Molecular dynamics simulation of thermal conductivity of silicon nanowires. *Applied Physics Letters* 75(14), 2056. (p. 78)
- Wang, C. Z., C. T. Chan, and K. M. Ho (1990, Dec). Tight-binding molecular-dynamics study of phonon anharmonic effects in silicon and diamond. *Phys. Rev. B* 42, 11276–11283. (p. 30)
- Wang, D., X. D, W. Q, Y. Hao, G. Jin, X. Guo, and K. N. Tu (2008). *Nanotechnology* 19, 215602. (p. 79)
- Wang, J. and H. Huang (2006). Novel deformation mechanism of twinned nanowires. *Applied Physics Letters* 88(20), 203112. (p. 79)
- Wang, J.-S., J. Wang, and N. Zeng (2006, Jul). Nonequilibrium green’s function approach to mesoscopic thermal transport. *Phys. Rev. B* 74, 033408. (p. 35)
- Wang, J.-S., N. Zeng, J. Wang, and C. K. Gan (2007, Jun). Nonequilibrium green’s function method for thermal transport in junctions. *Phys. Rev. E* 75, 061128. (p. 100)
- Wang, L. and J. Wu (2014, Jan). Frequency response of a thermal diode. *Phys. Rev. E* 89, 012119. (p. 7)
- Wang, X. H., A. Yamamoto, K. Eguchi, H. Obara, and T. Yoshida (2003). *Sci. Technol. Adv. Mater.* 4, 167–172. (p. 62)
- Wei, X.-K., A. K. Tagantsev, A. Kvasov, K. Roleder, C.-L. Jia, and N. Setter

- (2014). *Nat. Commun.* 5, 3031. (p. 63)
- Wu, H., F. Meng, L. Li, S. Jin, and G. Zheng (2012). Dislocation-driven cds and cdse nanowire growth. *ACS Nano* 6(5), 4461–4468. (p. 45)
- Xiong, Q., J. Wang, and P. C. Eklund (2006). *Nano Lett.* 6, 2736. (p. 79, 80)
- Xiong, S., J. Ma, S. Volz, and T. Dumitrica (2014). Thermally-active screw dislocations in si nanowires and nanotubes. *Small* 10(9), 1756–1760. (p. 78)
- Yamamoto, T. and K. Watanabe (2006, Jun). Nonequilibrium green’s function approach to phonon transport in defective carbon nanotubes. *Phys. Rev. Lett.* 96, 255503. (p. 17)
- Yang, K., Y. Chen, R. D’Agosta, Y. Xie, J. Zhong, and A. Rubio (2012, Jul). Enhanced thermoelectric properties in hybrid graphene/boron nitride nanoribbons. *Phys. Rev. B* 86, 045425. (p. 100)
- Yang, N., G. Zhang, and B. Li (2008). Carbon nanocone: A promising thermal rectifier. *Applied Physics Letters* 93(24), -. (p. 9)
- Yang, N., G. Zhang, and B. Li (2010). Violation of fourier’s law and anomalous heat diffusion in silicon nanowires. *Nano Today* 5(2), 85 – 90. (p. 17, 30, 82)
- Yang, W., H. Araki, C. Tang, S. Thaveethavorn, A. Kohyama, H. Suzuki, and T. Noda (2005). Single-crystal sic nanowires with a thin carbon coating for stronger and tougher ceramic composites. *Advanced Materials* 17(12), 1519–1523. (p. 62)
- Yang, Y. T., K. L. Ekinci, X. M. H. Huang, L. M. Schiavone, M. L. Roukes, C. A. Zorman, and M. Mehregany (2001). Monocrystalline silicon carbide nanoelectromechanical systems. *Applied Physics Letters* 78(2), 162–164. (p. 62)
- Yovanovich, M. M., J. R. Culham, and P. Teertstra (1997). Calculating interface resistance. *Electronics Cooling* 3, 24. (p. 6)
- Zhang, D.-B., E. Akatyeva, and T. Dumitrică (2011). Helical bn and zno nanotubes with intrinsic twisting: An objective molecular dynamics study. *Phys. Rev. B* 84, 115431. (p. 47)
- Zhang, W., N. Mingo, and T. S. Fisher (2006, 05). Simulation of interfacial phonon transport in si-ge heterostructures using an atomistic green’s function method. *Journal of Heat Transfer* 129(4), 483–491. (p. 30)
- Zhao, H. and J. B. Freund (2005). Lattice-dynamical calculation of phonon scattering at ideal si-ge interfaces. *Journal of Applied Physics* 97(2), -. (p. 38, 73)
- Zhong, S., T. Koch, M. Wang, T. Scherer, S. Walheim, H. Hahn, and T. Schimmel (2009). Nanoscale twinned copper nanowire formation by direct electrodeposition. *Small* 5(20), 2265–2270. (p. 84)
- Ziman, J. M. (1960). *Electrons and Phonons: The Theory of Transport Phenomena in Solids*. OXFORD at the Clarendon Press. (p. 13)

